

TOWARDS AN *AB INITIO* DESCRIPTION OF CORRELATED MATERIALS

BY CHUCK-HOU YEE

A dissertation submitted to the
Graduate School—New Brunswick
Rutgers, The State University of New Jersey
in partial fulfillment of the requirements
for the degree of
Doctor of Philosophy
Graduate Program in Physics and Astronomy

Written under the direction of

Kristjan Haule

and approved by

New Brunswick, New Jersey

October, 2012

ABSTRACT OF THE DISSERTATION

Towards an *Ab Initio* Description of Correlated Materials

by Chuck-Hou Yee

Dissertation Director: Kristjan Haule

Strongly-correlated materials are a rich playground for physical phenomena, exhibiting complex phase diagrams with many competing orders. *Ab initio* insights into materials combined with physical ideas provide the ability to identify the organizing principles driving the correlated electronic behavior and pursue first-principles design of new compounds. Realistic modeling of correlated materials is an active area of research, especially with the recent merger of density functional theory (DFT) with dynamical mean-field theory (DMFT).

This thesis is structured in two parts. The first describes the methods and algorithmic developments which drive advances in DFT+DMFT. In Ch. 2 and 3, we provide an overview of the two foundational theories, DMFT and DFT. In the second half of Ch. 3, we describe some of the principles guiding the combination of the two theories to form DFT+DMFT. In Ch. 4, we describe the algorithm lying at the heart of modern DFT+DMFT implementations, the hybridization expansion formulation of continuous-time quantum monte carlo (CTQMC) for the general Anderson impurity problem, as well as a fast rejection algorithm for speeding-up the local trace evaluation. The final chapter in the methods section describes an algorithm for direct sampling of the partition function, and thus the free energy and entropy, of simple Anderson impurity models within CTQMC.

The second part of the thesis is a collection of applications of our *ab initio* approach to key correlated materials. We first apply our method to plutonium binary alloys (Ch. 6), which when supplemented with slave-boson mean-field theory, allows us to understand the observed photoemission spectra. Ch. 7 describes the computation of spectra and optical conductivity for rare-earth nickelates grown as epitaxial thin films. In the final two chapters, we turn our attention to the high-temperature superconductors. In the first, we show that the charge-transfer energy is a key chemical variable which controls the superconducting transition temperatures across the cuprate families. In the second, we extend this idea towards first-principles design of cuprates by exploring a new family of copper oxysulfides.

Acknowledgements

First and foremost, I thank my adviser Kristjan Haule for his guidance. He has provided utter faith in my ability and the freedom to construct a graduate experience of my choosing. This dissertation would not have been possible without his strong support.

I also thank Gabriel Kotliar, who in many ways has been a co-adviser. His willingness to share his views on physics and provide feedback has been invaluable.

The diverse faculty at the department have created a wonderful place for physics. I especially appreciate the opportunity to collaborate with Piers Coleman, whose boundless enthusiasm for science and support for travel have enriched my graduate career. I have learned a great deal through discussions and courses with David Vanderbilt, Sang-Wook Cheong and Premi Chandra. I also would like to acknowledge Natan Andrei and Massimiliano di Ventra, who advised me during the early years of my graduate studies. Finally, Viktor Oudovenko has been an indispensable sysadmin.

It goes without saying that my time here at Rutgers and over in U.C. San Diego would have been terribly less colorful without the company of good friends: Senia, one of the sweetest I know; Sinisa, for lively debates; Adina, for her impeccable personal advice; Deepak, who freely shares his knack for physical innuendo; Chen, for the fast dinners; Ariel, for all the car rides and dances; Rebecca, with whom I have shared a large part of my life; Kshitij, for his diverse musical tastes; Mark, for just being so darn cool; Anat, for the dinner parties; Art, for being a partner in crime; Jessie, who is a complete sweetheart; and Phil, who shows up just when he's needed most. I would also like to thank Aatish, Aline, Anindya, Bryan, Cedric, Chioun, Christina, Dana, Daniel, Darakhshan, Hyowon, Ilya, Jan, John, Lucia, Lucian, Marietta, Sungpo, Tahir, Valentino, Vandana and Vic.

Finally, I thank my family, Mom, Dad, Suk-Ann and Ken-Hou, who have given me support I did not even recognize, watched grow during the course of my studies, and provided inspiration I wouldn't trade for anything else.

Dedication

To my family.

Table of Contents

Abstract	ii
Acknowledgements	iv
Dedication	vi
List of Tables	x
List of Figures	xii
1. Introduction	1
I Methods	10
2. Dynamical Mean-Field Theory	11
2.1. Primer: Ising Mean-Field Theory	12
2.2. Cavity Construction	13
2.3. Functional Approach	18
2.4. Impurity Solvers	22
3. DFT+DMFT	24
3.1. Density Functional Theory	25
3.2. Full-Potential Methods	30
3.3. The Locality Principle: Projection and Embedding	34
4. Continuous-Time Quantum Monte Carlo	41
4.1. Hybridization Expansion	42

4.2. Metropolis-Hastings Sampling	45
4.3. General Models	46
4.4. Evaluating the Impurity Trace	49
4.5. Fast Rejection via Lazy Evaluation	50
5. Reciprocal Distribution Sampling	52
5.1. Sampling the Reciprocal Distribution and Phase Space Volume	52
5.2. Spinless Fermions	53
5.3. One-Band Model	55
5.4. Arbitrary Number of Diagonal Baths	57
5.5. Thermodynamic Quantities	58
 II Applications	 63
 6. Valence Fluctuations and Quasiparticle Multiplets in Pu Chalcogenides and Pnictides	 64
6.1. Introduction	65
6.2. Numerical Method and Results	67
6.3. Slave-Boson Analysis	71
6.4. Summary	73
 7. Optical Conductivity in Lanthanum Nickelate Films	 75
7.1. Introduction	77
7.2. Optical Conductivity of LNO Films	79
7.3. Temperature-Dependence of Spectral Weight Transfer	81
7.4. Summary	85
 8. Correlating Superconducting Transition Temperatures in Hole-Doped Cuprates with the Charge-Transfer Energy	 86
8.1. Introduction	90
8.2. Extracting Chemical Parameters and Identifying Correlations	92

8.3. Calculating Transition Temperatures Using Cluster-DMFT	93
8.4. Summary	97
9. Engineering the Charge-Transfer Energy in Cuprates	99
9.1. Introduction	99
9.2. Chemical Tuning of the Charge-Transfer Energy	100
9.3. Structural and Thermodynamic Stability	104
9.4. Summary	106
10. Conclusion	108
Bibliography	109
Appendix A. Nonorthonormal Basis Sets	125
Appendix B. APW Symmetries	127
Appendix C. Slave-bosons for the Anderson Impurity Model	129
C.1. Review of Mean-field theory	131
C.2. Mean-Field Equations of the Anderson Impurity Model	133
C.3. Solution for Degenerate Orbitals	135
C.4. Solution for Atomic Multiplets	137
C.5. Effects of a Conduction Gap	139
C.6. Beyond Mean-Field: Fluctuations	141
Appendix D. Downfolding and Cluster-DMFT Implementation Notes .	147
D.1. Table of Parameters	147
D.2. Numerical Method	149
Appendix E. Iterated Perturbation Theory	154
Appendix F. Entropy via Integration	155

List of Tables

5.1. Table of polynomials g_k for Eq. 5.33.	58
9.1. Synthesis pathways for various cuprate oxysulfides.	106
D.1. Tight-binding parameters of the three-band p - d model, containing the in-plane $d_{x^2-y^2}$ and $p_{(x,y)}$ orbitals, for the hole-doped cuprates.	147

List of Figures

1.1. The Wave, an emergent phenomena in large crowds.	2
1.2. Comparison of phase diagrams of weakly- and strongly-correlated materials.	5
2.1. Legendre transforms for the free energy.	19
5.1. Decomposing the free energy for the Anderson impurity model.	61
5.2. Entropy for Anderson impurity model computed using reciprocal distribution sampling.	61
6.1. Overview of electronic properties of plutonium.	65
6.2. Plutonium pnictides and chalcogenides.	66
6.3. Electrical resistivities of PuTe and PuSb.	66
6.4. Computed spectra for PuTe and PuSb.	68
6.5. Gap formation in PuTe spectra.	69
6.6. Valence histograms for PuTe and PuSb.	70
6.7. Schematic of states giving rise to quasiparticle peaks in PuTe.	74
7.1. The structure of rhombohedrally distorted perovskite.	76
7.2. The Torrance phase diagram for rare earth nickelates.	76
7.3. Electrical resistivity of bulk polycrystalline LaNiO_3 (LNO).	77
7.4. Resistivity of LaNiO_3 thin films.	79
7.5. Optical conductivity of thick LNO films and corresponding density of states.	80
7.6. Optical conductivity of ultrathin epitaxially strained LNO.	82
7.7. Spectral function of LNO computed using DFT+DMFT.	83

7.8. Computed optical conductivity of LNO compared with experiment. . . .	84
7.9. Computed temperature dependence of the optical conductivity of LNO films.	84
7.10. The structure of the thick and ultrathin LNO films.	85
8.1. Overview of superconductivity and timeline of its discovery.	87
8.2. Cuprate structure.	88
8.3. Charge-transfer vs. Mott insulators.	89
8.4. Doping-temperature phase diagram of the cuprate superconductors. . .	89
8.5. Parameters of the three-band $p-d$ model for the cuprates.	91
8.6. Trend of charge-transfer energy with apical oxygen distance in single- layer cuprates.	92
8.7. Correlations of the cuprate $T_{c,max}$ with microscopic parameters of the three-band model Hamiltonian.	94
8.8. Calculated doping dependence magnetization and superconductivity for LSCO.	96
8.9. Sensitivity of superconducting order parameter to charge-transfer energy and oxygen-oxygen hopping.	97
9.1. Variation of charge-transfer energy in copper oxysulfides.	101
9.2. Trends in lattice parameters of copper oxysulfides.	102
9.3. Effects of pressure in oxysulfides vs. cuprates.	103
9.4. Octahedral rotations in $\text{Sc}_2\text{CuO}_2\text{S}_2$	105
C.1. Spectral density of the f electron with and without a conduction band gap.	140
D.1. ED treatment of the 3-band Hubbard model.	149
D.2. Calculated density of states and Green's function of LSCO.	152

Chapter 1

Introduction

Condensed matter physics seeks to elucidate the principles governing the quantum behavior of macroscopic numbers of interacting particles. The field traces its origins to the early twentieth century with the application of foundational work on quantum mechanics to solid state systems. The resulting theories explained the electronic and vibrational properties of simple metals and insulators. The field, characterized by close collaboration between theory and experiment, has grown to encompass a wide variety of observed phenomena in solids and in liquids, including superconductivity, magnetism, and topological order. Condensed matter physics has a record of fruitful interplay with other branches of physics and mathematics. For example, the methods of quantum field theory have become indispensable in condensed matter, while conversely, the Landau-Ginzberg theory of phase transitions and the renormalization group have grown far beyond their condensed matter origins. Experiment continues to pose new questions, from the discovery of new families of superconductors to truly two-dimensional materials in the form of graphene. The breadth of systems and phenomena encompassed, combined with the sheer quantity of open questions, guarantees that condensed matter will continue to be one of the largest and most vigorous fields of physics in the near future.

The theoretical side of condensed matter physics has been guided throughout its development by the principles of emergence and symmetry. Emergence is the idea that the behavior of 10^{23} particles may be very different from that of individual particles. The Wave (Fig. 1.1) is one realization of this principle. A more pertinent example is

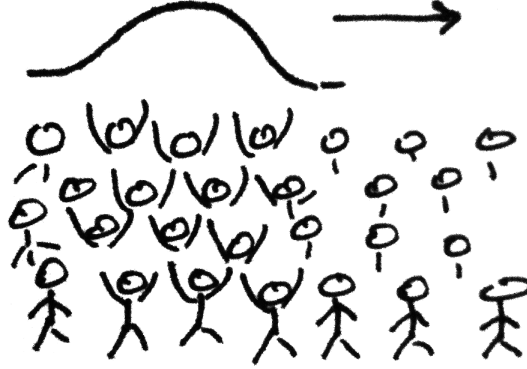


Figure 1.1: The Wave, an emergent phenomena in large crowds. The Wave is best described by a characteristic width and velocity, quantities which have little to do with the underlying individual particles. These particles in general are quite complex, yet only a few key properties (the presence of arms and a long-ranged interaction in the form of eyesight) are necessary to determine the macroscopic behavior of Waves.

that of plasmons, quantized oscillations in the density of electrons in a metal. These longitudinal modes can be visualized as sound waves propagating through the sea of electrons¹, and strongly affect the optical properties of metals, in particular, determining the characteristic color of copper and gold. Whereas the constituent electrons are fermions, characterized by spin $S = 1/2$, charge e and a fundamental mass m_e , the emergent plasmons are bosons, with integer spin, no charge and a mass dependent on the specific material under consideration. It turns out that in most metals, the constituent electrons still dominate the low-energy behavior, coexisting with the higher energy plasmons. However, in some systems, the emergent modes control even the low-energy physics. For example, the application of strong magnetic fields perpendicular to clean two-dimensional systems of electrons, like graphene [1, 2], produces the fractional quantum hall effect. Here, the low-energy excitations observed in electrical resistivity measurements are particles with fractional charge and anyonic statistics. The fact that emergent excitations are not adiabatically connected to the bare underlying particles renders their general identification and treatment particularly challenging.

In this quest to identify the low-energy excitations, we are guided by symmetry. In condensed matter, symmetry is particularly crucial for constraining crystal structures,

¹The analogy is not complete, as plasmons are gapped due to the long-ranged nature of the Coulomb interaction, and exist in the collisionless limit.

classifying states separated by phase transitions, and reducing the computational effort needed to perform simulations. For example, in approaching a new compound containing transition metals, one of the first questions to ask is the site symmetry of the transition metal ion. Straightforward application of group theory allows us to deduce the degeneracies of the d -electron energy levels directly from the crystal structure. Combined with knowledge of the valence, we have a reference frame to build our understanding of the magnetic properties of the material. If the electron spins in the material indeed overcome thermal and quantum fluctuations to order in a regular arrangement, identification of the symmetry of the order parameter is one of the key goals. This piece of information tells us about the critical behavior near the phase transition where the order appears, as well as how big of a unit cell we need for numerical simulation. Finally, symmetries of a different kind, those of the antisymmetric nature of fermionic wavefunctions with respect to the interchange of any two particles, has deep consequences on the formulation of algorithms used to simulate such systems.

This thesis focuses mainly on computational techniques for understanding and designing strongly-correlated materials. We lay out the framework of this field via two stories, the first describing the effect of electron correlations, and the second dealing with the development of electronic structure methods.

The Strong-Correlations Story: For the majority of materials, the framework of independent electrons moving in the periodic potential generated by the lattice nuclei is sufficient to account for the majority of properties. Simple metals, band insulators and some semiconductors, generally composed of materials with partially filled s or p shells, fall under this umbrella of *weakly-correlated* materials. The electron wavefunctions are itinerant, forming plane waves modulated by the crystal potential, known as Bloch states. Even when the effects of the mutual Coulomb repulsion are included, the electrons can still be treated as (nearly) independent particles because the large overlap between s and p orbitals at neighboring sites allows the kinetic energy to dominate. The electrons use this energy to screen the Coulomb interaction, rendering the effective interaction between them small. This mechanism, empirically described by Landau's Fermi liquid theory, is a cornerstone in the framework for describing weakly-correlated

materials.

However, in materials containing partially-filled d or f -shells, the effect of the Coulomb interaction between electrons cannot be ignored, and the movement of each electron is *strongly correlated* with those of its neighbors. These orbitals have small spatial extents as compared to the interatomic spacing and electrons cannot effectively screen each other when spatially confined. Therefore, electrons in these localized orbitals imbue atomic-like behavior into the material, which otherwise could be described by the Bloch states. The interplay between the itinerant, band-like character of the s and p electrons with the localized, atomic-like character of the d and f electrons poses a strong theoretical challenge, and is the hallmark of the field of *strongly correlated electrons*.

In strongly correlated materials, the internal degrees of freedom of the localized electrons—spin, charge, orbital—often order at low temperatures to form a myriad of states. Small changes in an external parameter (pressure, magnetic field, chemical doping) tunes the system through these states, forming complex phase diagrams (Fig. 1.2). This large sensitivity to external perturbations is characteristic of strongly-correlated systems, forming the foundation of their technological utility.

In theoretical approaches, the simplest model of a strongly-correlated system is the one-band Hubbard model:

$$H = - \sum_{ij\sigma} t_{ij} c_{i\sigma}^\dagger c_{j\sigma} + U \sum_i n_{i\uparrow} n_{i\downarrow}. \quad (1.1)$$

There are two noncommuting terms. The first describes the kinetic energy, capturing the itinerant band-like nature of the electrons. The second describes the potential energy in the form of a local on-site repulsion when two electrons occupy a single site. This crude model captures the fundamental tension between band and atomic physics, yet remains a challenge to solve. A key property of this model is the presence of a metal-insulator transition (MIT), which we can rationalize based on limiting cases. In the extreme atomic limit ($t = 0$) the system is a collection of isolated atoms, and thus an insulator. In the extreme band limit ($U = 0$), the electrons form Bloch states and is a metal. As we tune the ratio U/t , there must exist a metal-insulator transition.

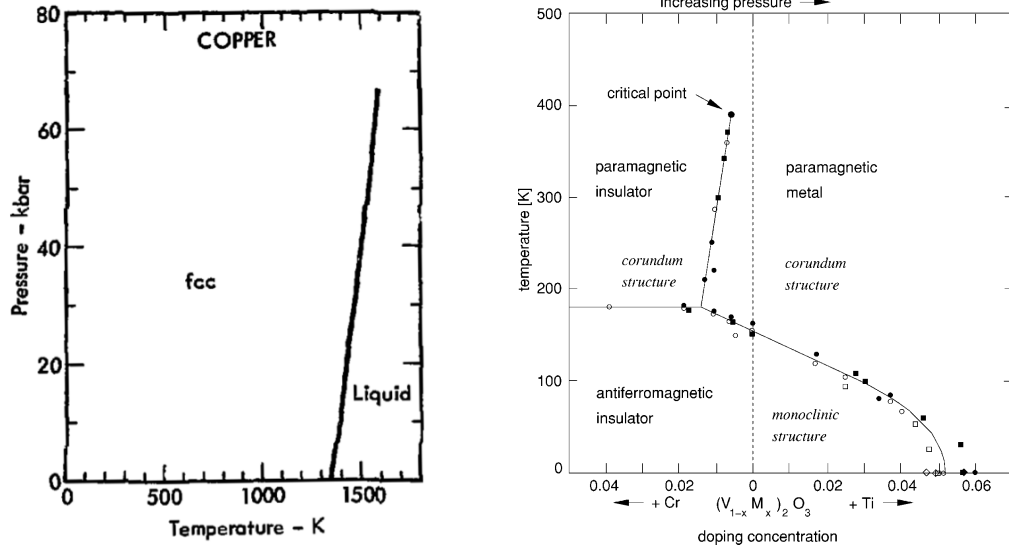


Figure 1.2: (left) The phase diagram of a typical weak-correlated metal, copper [3]. There are no phase transitions with the application of pressure. (right) In contrast, V_2O_3 , a canonical example of a strongly-correlated compound, exhibits three phases as a function of pressure and temperature [4]. Of particular interest is the metal-insulator transition between a paramagnetic metal and a paramagnetic insulator occurring above ~ 200 K as a function of pressure. Original data from Ref. [5]. Each tick on pressure scale is 4 kbar.

The exact nature of this transition (precise location in the U/t vs. T vs. doping phase diagram, fate of spin entropy, presence of superconductivity) is an active area of research [6].

Conventional perturbative treatments rely on small corrections to an appropriately chosen reference system. Due to the interplay between band and atomic physics in strongly-correlated systems, perturbative methods are inadequate, especially those based upon an expansion about the noninteracting limit. One line of theoretical attack rests on the observation that the main effect of the onsite Coulomb repulsion is to reduce the prevalence of doubly-occupied sites, leading to the observed macroscopic properties. Theoretical techniques designed to handle this suppression of the section of Hilbert space containing doubly-occupied sites include the Gutzwiller variational approach and slave bosons.

A orthogonal approach is taken by dynamical mean-field theory (DMFT). Historically, the formulation was taken in two steps. First, Metzner and Vollhardt [7] considered a novel limit to the Hubbard model, that of infinite lattice coordination. Each site is imagined to have an infinite number of neighbors, a construction equivalent

to taking the infinite-dimensional limit. In exchange for tractability, this step discards spatial fluctuations. In the second step, Georges and Kotliar [8] noticed that the infinite-dimensional Hubbard model was equivalent to a self-consistent quantum impurity model. Quantum impurity models describe set of local quantum states interacting with a bath (a continuum of non-interacting degrees of freedom). A concrete example is an iron atom embedded in a simple metal. Quantum impurity models are well-studied systems for which there already existed an entire suite of theoretical tools. The major advance of this second step is that all these theoretical tools could be brought to bear on the lattice problem. The early successes of DMFT included providing a clear description of the metal-insulator transition in the Hubbard model [9] and the associated spectral transfer observed in optical conductivity measurements of V_2O_3 [10].

The above classes of techniques are deterministic and work in the thermodynamic limit. A different class of algorithms based on repeated random sampling, called Monte Carlo methods after the Monte Carlo Casino in Monaco, simulate a large (but finite) section of a system, and use extrapolation to reach the thermodynamic limit. These have the advantage that arbitrary interactions can be included, but suffer from finite size effects due to the need for system-size extrapolation and the notorious fermion minus sign problem. Since Monte Carlo methods are based on probabilities, the negative regions in fermionic wavefunctions cause rapid loss of numerical precision. Thus, while bosonic systems containing thousands of particles can be simulated, effectively reaching the thermodynamic limit, the majority of interesting fermionic systems remain intractable to Monte Carlo methods. There are key exceptions, and Monte Carlo algorithms for quantum impurity models constitute one important case, which finds application as the impurity solver at the heart of the DMFT algorithms.

The above approaches to strongly-correlated systems have mainly focused on simplified models. The techniques for realistically modeling weakly-correlated materials were historically developed during the same period, which we describe in the next section.

The First-Principles Story: First-principles modeling of materials has grown enormously to become an industry in the past several decades. In this field, also known as *ab initio* modeling, practitioners specify only the type and positions of the atoms

forming the crystal lattice and compute macroscopic quantities without any adjustable parameters. The exponential rise of computational power, but more importantly, huge advances in algorithmic developments, have fueled the growth of this field. The anecdotal question in the field is, “Would you rather have the algorithms of today running on the machines of 1970, or vice versa?” The answer is that algorithmic developments have far surpassed the growth of computational power.²

For realistic modeling of solid state systems, density functional theory (DFT) is the method of choice, having been the workhorse of the first-principles community for several decades. The method’s ability to capture the chemistry of weakly-correlated compounds and compute total energies allows quantitative structural and electronic insights inaccessible by other methods. The historical development of DFT proceeded in two steps. The first, by Hohenberg and Kohn [11], showed that the ground state energy could be rewritten entirely in terms of (a functional of) the electronic density $n(\mathbf{r})$. This provided the theoretical basis for the subsequent construction of a computational practical DFT, a step taken by Kohn and Sham [12]. They noticed that the problem of finding a practical approximation to the ground state energy functional and solving for the electronic density could be accomplished by a mapping to an auxiliary noninteracting system of fermions.

The ultimate goal of the field of first-principles modeling is to be able to solve the inverse problem of *materials design*: a material with a given set of properties is desired, and first-principles calculations would predict which elements should be combined to form the desired compound. Contrast this with the direct problem, that of predicting materials properties given the atomic constituents. The direct problem is generically divided into two steps, (1) structural determination of the crystal lattice given the chosen elements, and (2) computation of the materials properties given the structure. Step (2) is relatively easy for weakly-correlated materials due to DFT, but remains difficult for strongly-correlated materials. Step (1) is even harder. The inverse problem is the most challenging of all.

²I have not been able to determine the source of this anecdote.

Materials design of strongly-correlated compounds is even more challenging historically due to the lack of controlled methods. In an effort to fill this gap, steps have been taken in the past decade to combine the realism of DFT with the ability DMFT to capture the effect of correlations. The resulting framework, termed DFT+DMFT, has produced realistic descriptions of compounds in regimes where the effective interaction is manifestly local, such as heavy fermions and the magnetic state of cuprates. One of the key outputs of DFT+DMFT is the one-particle electronic spectra, which can be directly compared to photoemission experiments.

The first-principles field is characterized by tight coupling between experimental observations, theoretical ideas and numerical computations. This is especially true for DFT+DMFT since comparisons with experiment can help uncover algorithmic limitations. Prior to the advent of electronic-structure methods, the workflow could be best described by a single stage:

$$\text{qualitative ideas} \longrightarrow \text{materials synthesis.} \quad (1.2)$$

The advent of first-principles methods has streamlined the guidance theorists can provide experimentalists by inserting an intermediate step where promising candidate materials can be directly identified:

$$\text{qualitative ideas} \longrightarrow \text{computational screening} \longrightarrow \text{materials synthesis.} \quad (1.3)$$

The community also constantly feeds information backwards to improve the first-principles methods. Additionally, computation can uncover new qualitative ideas.

$$\text{qualitative ideas} \longleftarrow \text{computational screening} \longleftarrow \text{materials synthesis.} \quad (1.4)$$

The ability to synthesize materials and devices on short timescales means that theoretical ideas can be quickly tested, leading to fruitful calibration of ideas and algorithms.

This thesis focuses on electronic structure methods as applied to strongly-correlated systems, and is divided into two parts. The first half describes the main methods used, beginning with a general introduction to DMFT in Chap. 2. We then describe the formulation, development and implementation of the combination of DFT and DMFT

within the linearized augmented planewave formalism in Chap. 3. We conclude the methods section by describing the hybridization-expansion continuous-time quantum monte carlo algorithm for solving impurity problems, and reciprocal distribution sampling for computation of free energies. The second half covers applications to several families of materials: heavy fermions, nickelates, and cuprates.

Chapter 2

Dynamical Mean-Field Theory

The dynamical mean-field theory (DMFT) approach to treating strongly-correlated systems replaces a lattice model by a single-site quantum impurity problem embedded in a self-consistently determined effective medium [7, 8]. It is a mean-field theory in that inter-site quantum correlations are approximated by an averaged or effective interaction. However, local on-site quantum dynamics, which describe the hopping of electrons between the site and the surrounding medium, are retained, hence the name dynamical mean-field theory. For a brief digest, see Ref. [13], while Refs. [14, 15, 16] give more detailed expositions.

The electronic behavior of correlated systems is characterized by the competition between the kinetic energy and the Coulomb interaction. DMFT is a non-perturbative technique which retains this competition while simplifying the computation, and is able to span the full range of behavior from the localized atomic limit to the itinerant band limit. One of its key early successes was a description of the Mott transition, the metal-insulator transition driven by strong electron-electron repulsion. The theory is quite flexible: DMFT can also describe ordered states, such as magnetism, charge-order and superconductivity, whenever the order parameter is essentially local. Short-ranged interactions neglected in the vanilla (single-site) DMFT formalism, known to be important in some materials like the underdoped regime of high-temperature superconductors, can be included via extensions of the self-consistency condition by mapping the lattice to a small cluster of impurities [17].

Formally, DMFT consists of treating the self-energy as a local quantity, that is,

neglecting its momentum dependence. This approximation is exact in the infinite-coordination limit of lattices. However, in many models and real materials, the inter-site correlations are small and the DMFT approximation remains extremely valid, capturing the essential correlation-driven behavior.

In all but the simplest of models, DMFT is a computational method, since the solution of the impurity problem for arbitrary densities and interactions is intractable analytically (although analytic methods give valuable insight into the behavior of the impurity). The DMFT self-consistency equation is nonlinear, and the preferred method of solution is iterative: an initial guess for the self-energy, usually taken to be zero, is used to construct the lattice Green's function $G(i\omega_n)$. This is then mapped to an effective impurity problem, whose form usually takes that of an Anderson impurity model (AIM), which produces a new self-energy used to create the next lattice Green's function. The cycle is iterated until the self-energy is converged. The solution of the AIM is the most time-consuming step. To give an idea of scale, the single-site approximation for the simplest models require minutes on modern computers (year 2012), while large clusters for more complex models require a modest several-thousand cpu-hours for reasonable results.

In the following, we introduce the idea of DMFT by analogy with the standard Ising mean-field theory. We then provide two views of the derivation of DMFT: one based on the cavity construction, and second based on effective actions.

2.1 Primer: Ising Mean-Field Theory

The mean-field approximation as applied in the context of lattice models consists of replacing the lattice with a single-site interacting with an external bath created by the degrees of freedom on all the other sites. The simplest illustration of this idea is the mean-field theory of the Ising model:

$$H = -J \sum_{\langle i,j \rangle} S_i S_j - h \sum_i S_i. \quad (2.1)$$

The mean-field approach singles out a given site, say the 0th site, and replaces its interaction with its neighboring sites with an averaged (mean) field by decoupling the

interaction term:

$$H_0 = -J \sum_{\langle i,0 \rangle} S_i S_0 - h S_0 \approx - \left(J \sum_i \langle S_i \rangle + h \right) S_0. \quad (2.2)$$

If we further make the assumption of translational invariance, and write for the magnetization of the neighboring sites $m = m_i = \langle S_i \rangle$, we see that the 0th site is governed by an effective hamiltonian,

$$H_0^{\text{eff}} = -h_{\text{eff}} S_0 \quad h_{\text{eff}} = JZm + h, \quad (2.3)$$

where Z is the number of neighboring sites. The effective field h_{eff} depends on the magnetization m which can be self-consistently computed from the local hamiltonian H_0^{eff} by constructing the partition function and taking the derivative with respect to the magnetic field. For the Ising model, we find $m = \langle S \rangle = \tanh(\beta h_{\text{eff}})$, which can be combined with the definition of the effective hamiltonian (Eq. 2.3 to arrive at the self-consistency condition for the magnetization:

$$m = \tanh(\beta JZm + \beta h). \quad (2.4)$$

The lattice problem has been replaced by a self-consistently determined single-site problem. The mapping is exact when the lattice coordination becomes large: as the number of nearest neighbors of a site becomes large, it is intuitive that they can be replaced by their average effect since fluctuations scale inversely with the (square-root) of the number of nearest-neighbors.

The straight-forward extension of this mean-field concept to a quantum system is the basis of DMFT, which we describe in the following.

2.2 Cavity Construction

The idea of the cavity construction is simple: derive an effective action for a single site by integrating out the degrees of freedom of all other lattice sites. The resultant single-site problem is in general insoluble, so specific approximations are made to retain the essential strongly-correlated physics while rendering the problem tractable.

We present the derivation for the simplest case of the one-band Hubbard model. The starting point is the partition function, written in functional form:

$$Z = \int \prod_{i\sigma} Dc_{i\sigma}^\dagger Dc_{i\sigma} e^{-S}. \quad (2.5)$$

Here, i indexes the lattice sites and σ is the fermion spin. The action contains the standard hopping and onsite repulsion terms,

$$S = \int_0^\beta d\tau \left[\sum_{ij\sigma} c_{i\sigma}^\dagger (\delta_{ij} \partial_\tau - t_{ij}) c_{j\sigma} + U \sum_i n_{i\uparrow} n_{i\downarrow} \right]. \quad (2.6)$$

Next, we partition the system into the site of interest, which we will call the 0th and use the notation $d_\sigma = c_{0\sigma}$ for its operators. The rest of the system, containing the cavity created by the absence of the 0th site, is denoted by (0). The action splits into three parts, one for each subsystem and a hybridization describing the coupling between the two:

$$S = S_0 + S_{\text{hyb}} + S_{(0)}, \quad (2.7)$$

where

$$S_0 = \int_0^\beta d\tau \left[d_\sigma^\dagger \partial_\tau d_\sigma + U n_{d\uparrow} n_{d\downarrow} \right] \quad (2.8)$$

$$S_{\text{hyb}} = - \int_0^\beta d\tau \sum_{i\sigma} \left[t_{i0} c_{i\sigma}^\dagger d_\sigma + \text{h.c.} \right] \quad (2.9)$$

$$S_{(0)} = \int_0^\beta d\tau \left[\sum_{ij\sigma} c_{i\sigma}^\dagger (\delta_{ij} \partial_\tau - t_{ij}) c_{j\sigma} + U \sum_i n_{i\uparrow} n_{i\downarrow} \right]. \quad (2.10)$$

Here, it is understood the sums over i and j exclude the 0th site. With this decomposition, we formally integrate out all of the lattice except the 0th site in the expression for the partition function:

$$Z = Z_{(0)} \int \prod_{\sigma} Dd_\sigma^\dagger Dd_\sigma e^{-S_0} \langle e^{-S_{\text{hyb}}} \rangle_{(0)}. \quad (2.11)$$

The notation $\langle \rangle_{(0)}$ means the average over the cavity action $S_{(0)}$ and $Z_{(0)}$ is the cavity partition function. We use the linked-cluster theorem to move the average into the exponential. The partition function becomes

$$Z = \int \prod_{\sigma} Dd_\sigma^\dagger Dd_\sigma e^{-S_{\text{eff}}}, \quad (2.12)$$

where the effective action is

$$S_{\text{eff}} = \beta F_{(0)} + S_0 + \sum_{n=1}^{\infty} \sum_{i_1 \dots i_n} \sum_{j_1 \dots j_n} \int_0^\beta \prod_{a=1}^n d\tau_{i_a} d\tau_{j_a} \prod_{a=1}^n t_{0i_a} t_{j_a 0} \\ \times d_\sigma^\dagger(\tau_{i_1}) \dots d_\sigma^\dagger(\tau_{i_n}) G_{i_1 \dots j_n}^{(0)}(\tau_{i_1} \dots \tau_{i_n}; \tau_{j_1} \dots \tau_{j_n}) d_\sigma(\tau_{j_n}) \dots d_\sigma(\tau_{j_1}). \quad (2.13)$$

The connected $2n$ -point cavity Green's function is denoted $G^{(0)}$. Generally we can drop the constant $\beta F_{(0)}$, where $F_{(0)} = -T \log Z_{(0)}$ is the cavity free energy. The effective single-site problem we have derived, in principle, contains complete information of all local observables, which we could extract by coupling source fields to the d_σ^\dagger operators. However, the problem is intractable because of the presence of the $2n$ -point cavity correlators.

The DMFT approximation consists of dropping all terms in the effective action beyond the first:

$$S_{\text{eff}}^{\text{DMFT}} = S_0 + \sum_{ij\sigma} \int_0^\beta d\tau \int_0^\beta d\tau' d_\sigma^\dagger(\tau) t_{0i} G_{ij}^{(0)}(\tau - \tau') t_{j0} d_\sigma(\tau') \quad (2.14)$$

When is this approximation justified? Analysis of the scaling of the Green's functions with the number of nearest neighbors $Z_{|i-j|}$ at a Manhattan distance of $|i-j|$ shows that in the infinite coordination limit (i.e. infinite dimensional limit), this approximation is exact [15].

We rewrite the action to emphasize the effective-field by grouping together all the one-particle terms:

$$S_{\text{eff}}^{\text{DMFT}}[\mathcal{G}_0] = - \sum_{\sigma} \int_0^\beta d\tau \int_0^\beta d\tau' d_\sigma^\dagger(\tau) \mathcal{G}_0^{-1}(\tau - \tau') d_\sigma(\tau') + \int_0^\beta d\tau U n_{d\uparrow} n_{d\downarrow} \quad (2.15)$$

where we have defined

$$\mathcal{G}_0^{-1}(\tau) = -\frac{\partial}{\partial \tau} - \sum_{ij} t_{0i} G_{ij}^{(0)}(\tau) t_{j0}. \quad (2.16)$$

This equation defines the effective field \mathcal{G}_0 experienced by the site, which intuitively is constructed of processes which hop off the site t_{0i} , propagate in the lattice $G_{ij}^{(0)}$, and return to the site t_{j0} . The Green's function \mathbf{G}_0 plays the analogous role of the effective hamiltonian h_{eff} in the Ising mean-field treatment.

The last step is to derive the self-consistency condition by relating the cavity Green's function $G^{(0)}$ to local quantities. The relation between the cavity and full Green's function G is

$$G_{ij}^{(0)} = G_{ij} - \frac{G_{i0}G_{0j}}{G_{00}}. \quad (2.17)$$

The idea is to subtract out the paths which pass through the 0th site from the full propagator G_{ij} . In the non-interacting case, these paths are given by $G_{i0}G_{00}^{-1}G_{0j}$ where the inserted factor G_{00}^{-1} ensures paths which leave and return to the intermediate 0th site are only counted once. In the presence of interactions, this expression is exact only in the infinite-dimensional case, as first derived by Hubbard [18].

Inserting this relation into the expression for the effective field \mathbf{G} , we must compute the sum

$$\mathcal{G}_0^{-1} = i\omega_n - \sum_{ij} t_{0i}G_{ij}t_{j0} + \left(\sum_i t_{0i}G_{i0} \right)^2 G_{00}^{-1}. \quad (2.18)$$

Since we are working in the infinite-dimensional limit, the self-energy is local, an approximation which can be justified by power counting [15]. Since the self-energy is local, that is, \mathbf{k} -independent, the Fourier transform of the full Green's function takes the form

$$G_{\mathbf{k}} = \frac{1}{\zeta - \epsilon_{\mathbf{k}}}, \quad \zeta = i\omega_n - \Sigma(i\omega_n). \quad (2.19)$$

Using this form of $G_{\mathbf{k}}$, we can derive the following two identities by Fourier transforms:

$$\sum_i t_{0i}G_{i0} = \sum_{\mathbf{k}} \epsilon_{\mathbf{k}}G_{\mathbf{k}} = \zeta G_{00} - 1 \quad (2.20)$$

$$\sum_{ij} t_{0i}G_{ij}t_{j0} = \sum_{\mathbf{k}} \epsilon_{\mathbf{k}}^2 G_{\mathbf{k}} = \zeta^2 G_{00} - \zeta. \quad (2.21)$$

Using these expressions, we get for the effective field

$$\mathcal{G}_0 = \Sigma + G_{00}^{-1} \quad (2.22)$$

Now that we have an expression for \mathcal{G}_0 , and thus the DMFT effective action, purely in terms of local quantities, we can compute any local observable, in particular, the local Green's function G_{00} , giving us the DMFT self-consistency condition

$$G_{00}(i\omega_n) = \int \mathcal{D}[d^\dagger d] d^\dagger(i\omega_n) d(i\omega_n) e^{-S_{\text{eff}}^{\text{DMFT}}[\mathcal{G}_0]}. \quad (2.23)$$

When combined with the definition of the local part of the lattice Green's function,

$$G_{00}(i\omega_n) = \sum_{\mathbf{k}} \frac{1}{i\omega_n - \epsilon_{\mathbf{k}} - \Sigma(i\omega_n)}, \quad (2.24)$$

the three equations 2.22, 2.23 and 2.24 form a closed non-linear set of expressions which can be solved for the local self-energy $\Sigma(i\omega_n)$. These equations are analogous to the self-consistent equation determining the magnetization in the Ising mean-field theory. Likewise, when given the band dispersion $\epsilon_{\mathbf{k}}$ and the onsite repulsion U , solution of the DMFT equation produces the self-energy Σ , or equivalently, the lattice Green's function $G_{\mathbf{k}}$.

In practice, the self-consistency equation is solved iteratively. An initial guess for the self-energy $\Sigma(i\omega_n)$ is chosen, usually taken to be zero for a new calculation, or the result of a previous converged run if we know it is a good starting point. Then, the algorithm proceeds by cycling through the following steps:

- Compute the local Green's function given Σ :

$$G_{00}(i\omega_n) = \sum_{\mathbf{k}} \frac{1}{i\omega_n - \epsilon_{\mathbf{k}} - \Sigma(i\omega_n)}, \quad (2.25)$$

- Compute the effective field:

$$\mathcal{G}_0^{-1} = G_{00}^{-1} + \Sigma \quad (2.26)$$

- Solve the impurity model for the local Green's function

$$G_{00}(i\omega_n) = \int \mathcal{D}[d^\dagger d] d^\dagger(i\omega_n) d(i\omega_n) e^{-S_{\text{eff}}^{\text{DMFT}}[\mathcal{G}_0]}. \quad (2.27)$$

- Extract the new self-energy:

$$\Sigma = \mathcal{G}_0^{-1} - G_{00}^{-1} \quad (2.28)$$

- Iterate these steps until the distance between the self-energy at the n -th and $(n+1)$ -th steps is less than some threshold ϵ :

$$||\Sigma_{n+1} - \Sigma_n|| < \epsilon \quad (2.29)$$

Since the effective field \mathcal{G}_0 acts as the free part of the local impurity problem, we often decompose it into its constituent onsite impurity level E_{imp} and a hybridization function $\Delta(i\omega_n)$ which accounts for the retarded quantum processes hopping electrons from the impurity into the effective medium and back:

$$\mathcal{G}_0(i\omega_n) = \frac{1}{i\omega_n - E_{\text{imp}} - \Delta(i\omega_n)}. \quad (2.30)$$

The hybridization is defined such that $\Delta(i\omega_n \rightarrow \infty) = 0$ so that the static component is captured in E_{imp} . The full impurity Green's function \mathcal{G} is the solution to the impurity problem,

$$\mathcal{G}(i\omega_n) = \int \mathcal{D}[d^\dagger d] d^\dagger(i\omega_n) d(i\omega_n) e^{-S_{\text{eff}}^{\text{DMFT}}[\mathcal{G}_0]}, \quad (2.31)$$

which must equal the local part of the lattice Green's function G_{00} ,

$$\frac{1}{i\omega_n - E_{\text{imp}} - \Delta - \Sigma} = \sum_{\mathbf{k}} \frac{1}{i\omega_n + \mu - \epsilon_{\mathbf{k}} - \Sigma}. \quad (2.32)$$

These three equations form an alternative way of writing the DMFT self-consistency condition, and we will use both in the following chapters.

2.3 Functional Approach

The effective action formalism is an elegant method for presenting a unified description of various approaches to the many-body problem. The basic idea is to choose an observable A and construct a functional $\Gamma[A]$ which (a) is extremized at the true A of the system, and (b) gives the free energy F when evaluated at its extremum (see Fig. 2.1). The construction of Γ relies on Legendre transforms and the utility of this formalism lies in the ability to write Γ as a perturbation series in the interaction strength. When the observable A is chosen to be the Green's function G , the functional Γ is called the Baym-Kadanoff functional. DMFT arises from choosing specific approximations to the full Baym-Kadanoff functional. In the following, we first derive the Baym-Kadanoff functional, then describe the DMFT approximation.

We begin with the free energy written in functional form:

$$e^{-\beta F} = \int \mathcal{D}[\psi^\dagger \psi] e^{-S}. \quad (2.33)$$

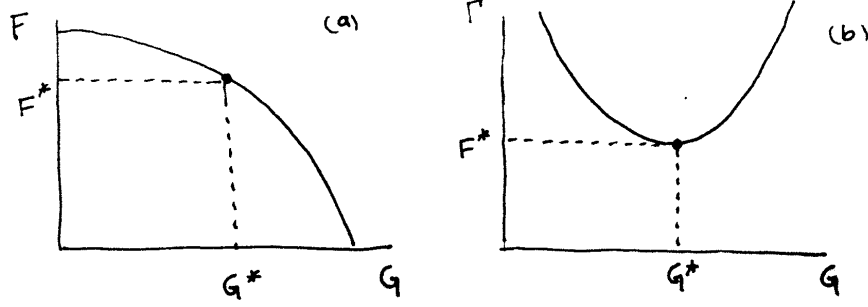


Figure 2.1: (a) The free energy $F = F[G]$, viewed as a functional of the Green's function G , is not stationary at the physical value G^* . (b) In contrast, the Baym-Kadanoff functional $\Gamma = \Gamma[G]$ is stationary at G^* (in this case minimized), and has the value of the physical free energy $\Gamma[G^*] = F^*$ at its stationary point.

The observable of interest is the operator $\psi^\dagger(\mathbf{r}\tau)\psi(\mathbf{r}'\tau')$, which produces the Green's function

$$G(\mathbf{r}'\tau'; \mathbf{r}\tau) = -\left\langle T_\tau \psi(\mathbf{r}'\tau') \psi^\dagger(\mathbf{r}\tau) \right\rangle \quad (2.34)$$

as its expectation value. We modify the action by adding a source term

$$e^{-\beta F} = \int \mathcal{D}[\psi^\dagger \psi] \exp \left(-S - \int d\mathbf{r} d\tau d\mathbf{r}' d\tau' \psi^\dagger(\mathbf{r}\tau) J(\mathbf{r}\tau, \mathbf{r}'\tau') \psi(\mathbf{r}'\tau') \right), \quad (2.35)$$

so that the functional derivative of the free energy with respect to the source field J gives us the Green's function in the presence of the source field

$$\frac{\delta F[J]}{\delta J} = G[J]. \quad (2.36)$$

The physical Green's function G^* is obtained by evaluating the above equation at $J = 0$, and the physical free energy is likewise $F^* = F[J = 0]$.

The idea of the Legendre transform is to consider the Green's function G as the independent variable rather than J , which is done by inverting this equation to obtain $J = J[G]$, which has the property that $J[G^*] = 0$. Substituting this into the free energy, we get $F = F[J[G]]$, which is shown in Fig. 2.1a. Finally, we form the Baym-Kadanoff functional via the Legendre transform

$$\Gamma[G] = F[J[G]] - \text{tr } J[G]G. \quad (2.37)$$

We prove that $\Gamma[G]$ is extremized at the physical G^* by using the chain rule:

$$\frac{\delta \Gamma[G]}{\delta G} = \frac{\delta F}{\delta J} \frac{\delta J}{\delta G} - \frac{\delta J}{\delta G} G - J = -J[G]. \quad (2.38)$$

Since $J[G^*] = 0$, we find that

$$\left. \frac{\delta \Gamma}{\delta G} \right|_{G^*} = 0, \quad (2.39)$$

so $\Gamma[G]$ is extremized at the physical Green's function, and its value

$$\Gamma[G^*] = F[J[G^*] = 0] = F^* \quad (2.40)$$

is the physical free energy.

With these preliminaries, we first construct the Baym-Kadanoff functional for a hamiltonian without interactions, which we denote $\Gamma_0[G]$. Since the action is quadratic, we can explicitly write down the free energy

$$F_0[J] = -\text{tr} \log(-G_0^{-1} + J), \quad (2.41)$$

where G_0 is the non-interacting Green's function, a fixed input parameter. Following the steps outlined above, the Green's function in the presence of the source field is

$$G[J] = \frac{\delta F_0[J]}{\delta J} = \frac{1}{G_0^{-1} - J}, \quad (2.42)$$

which we invert to obtain $J_0[G] = G_0^{-1} - G^{-1}$. We note that if we evaluate the expression for the source field J_0 of the noninteracting system using the physical Green's function G^* for the *interacting* system, we get the physical self-energy of the interacting system, since $\Sigma^* = G_0^{-1} - (G^*)^{-1}$ is the just Dyson's equation. Using the expression for $J_0[G]$, we arrive at the result for the noninteracting Baym-Kadanoff functional

$$\Gamma_0[G] = -\text{tr} \log(-G^{-1}) - \text{tr} J_0[G]G \quad (2.43)$$

$$J_0[G] = G_0^{-1} - G^{-1}. \quad (2.44)$$

It can be checked that the functional has the correct stationary properties.

In the presence of interactions, the Baym-Kadanoff is shifted from its free form by additional terms which we denote $\Phi[G]$:

$$\Gamma[G] = \Gamma_0[G] + \Phi[G]. \quad (2.45)$$

Our goal is to determine $\Phi[G]$, called the Luttinger-Ward functional. To this end, we use the fact that $\Gamma[G]$ must be stationary at the physical Green's function G^* of the

interacting system:

$$\left. \frac{\delta \Gamma[G]}{\delta G} \right|_{G^*} = G^{-1} - G \frac{\delta J_0[G]}{\delta G} - J_0[G] + \left. \frac{\delta \Phi[G]}{\delta G} \right|_{G^*} = 0 \quad (2.46)$$

The first two terms cancel, and we get an equation which the Luttinger-Ward functional must satisfy at the stationary point:

$$\left. \frac{\delta \Phi[G]}{\delta G} \right|_{G^*} = \Sigma^*. \quad (2.47)$$

This equation offers a simple diagrammatic recipe: construct $\Phi[G]$ by summing all two-particle irreducible skeleton graphs. The the functional derivative amounts to opening one (interacting) Green's function line, and the self-energy is defined as the sum of all one-particle irreducible diagrams, so $\Phi[G]$ must contain two-particle irreducible quantities. The complication of skeleton graphs arises because the derivative is with respect to G and not G_0 [19, 20].

To summarize, the Baym-Kadanoff functional for a general interacting system characterized by a noninteracting Green's function G_0 is

$$\Gamma[G] = -\text{tr} \log(-G^{-1}) - \text{tr} J_0[G]G + \Phi[G] \quad (2.48)$$

$$J_0[G] = G_0^{-1} - G^{-1}, \quad (2.49)$$

where the Luttinger-Ward functional $\Phi[G]$ captures the effect of interactions, and is the sum of all two-particle irreducible skeleton diagrams. The stationary point of the functional is the physical Green's function G^* and its value $\Gamma[G^*] = F^*$ is the free energy.

In this functional framework, the DMFT approximation is simple to state: include only local diagrams in $\Phi[G]$. Technically, this means

$$\frac{\delta \Phi_{\text{DMFT}}[G]}{\delta G_{ij}} = 0 \quad \text{for } i \neq j, \quad (2.50)$$

where i and j index lattice sites. This implies the self-energy is local, which is an equivalent statement of the DMFT approximation:

$$\Sigma_{ij}^{\text{DMFT}} = \delta_{ij} \frac{\delta \Phi_{\text{DMFT}}[G]}{\delta G_{ii}} \quad (2.51)$$

Furthermore, if we have a translationally invariant system, we construct $\Phi_{\text{DMFT}}[G]$ such that the self-energy is independent of the lattice site i . An advantage of the functional formalism is that there is no need to appeal to the infinite-dimensional limit since it is clear which diagrammatic contributions are discarded.

Practical construction of the DMFT Luttinger-Ward functional requires mapping the lattice to an impurity problem, whose Green's function we denote \mathcal{G} . The impurity problem is described by the functional

$$\Gamma_{\text{imp}}[\mathcal{G}] = -\text{tr} \log(-\mathcal{G}^{-1}) - \text{tr} J_0[\mathcal{G}] \mathcal{G} + \Phi_{\text{imp}}[\mathcal{G}] \quad (2.52)$$

$$J_0[\mathcal{G}] = \mathcal{G}_0^{-1} - \mathcal{G}^{-1} \quad (2.53)$$

If we choose \mathcal{G}_0^{-1} so that the solution of the impurity problem $\mathcal{G} = G_{ii}$ of the lattice, then the impurity self-energy equals the DMFT approximation to the lattice self-energy.

2.4 Impurity Solvers

We conclude with a brief discussion of various impurity solvers used to solve the auxiliary Anderson impurity model. The earliest solvers were based on iterated perturbation theory (IPT), a scheme based on solving the impurity problem perturbatively by expanding in the interaction U up to second-order. In the half-filled case, IPT successfully captured the Mott transition (see Appendix E for details).

However, DMFT on all but the simplest lattices and at arbitrary points in the temperature-doping phase diagram requires impurity solvers capable of handling more complex atomic interactions (including Hund's coupling) and arbitrary hybridization functions. Methods based on the Bethe ansatz, while exact, are constrained to linear bath dispersions and the Kondo regime [21]. Slave boson techniques [22, 23, 24] give valuable physical insight but again are applicable in limited regimes and display an unphysical phase transition due to boson condensation.

Computational methods based on resummation of salient classes of diagrams increased the flexibility of the impurity solver. In particular, those based on the non-crossing approximation (NCA) and one-crossing approximation (OCA) allowed access to physics of realistic models, but the approximations still lead to a slight noncausality

in the DMFT equations. Exact diagonalization (ED) and the numerical renormalization group (NRG) can be used to access extremely low temperatures.

The modern impurity solvers of choice are those based on quantum Monte Carlo (QMC). The Hirsch-Fye algorithm [25], which mapped the Anderson impurity model to a set of auxiliary Ising spin, was the first widely used QMC impurity solver. The formulation of continuous-time quantum monte carlo algorithms (CTQMC) [26, 27, 28, 29, 30] allowed DMFT to be applied to systems with realistic atomic interactions, access short-ranged spatial fluctuations via clusters, and probe lower temperatures regimes and stronger interaction strengths. The major advantage of QMC algorithms are their ability to solve the impurity problem exactly, the trade-off being that the output self-energy is given on the imaginary axis, requiring a procedure known as analytic continuation to extract real-axis quantities. Additionally, in some regimes, the fermionic sign problem forbids the application of QMC due to an exponential loss in accuracy. In Chapter 4, we describe the hybridization-expansion formulation of CTQMC used for the majority of this work.

Chapter 3

DFT+DMFT

There is enormous interest in extending the DMFT treatment of simple models to realistic correlated materials. Density functional theory (DFT) is the standard method routinely used to model weakly-correlated compounds. The idea of DFT+DMFT is to combine the strengths of each method: DFT is used to capture the physics of the weakly-correlated s and p bands, while DMFT describes the physics of the strongly-correlated d and f orbitals. The challenge is to merge the two theories in a self-consistent manner.

The combination of DFT+DMFT is currently considered the most powerful and practical method for *ab initio* modeling of correlated materials. Our implementation is able to describe heavy quasiparticles in renormalized metals, the paramagnetic Mott state, as well as magnetically- and charge-ordered states in compounds. The method produces spectral functions which can be directly compared to experimental techniques such as photoemission and optics. We have coded an implementation of DFT+DMFT using full-potential basis sets, as described in Ref. [31], to which we refer the reader interested in details. In this chapter, we describe the formal structure of DFT, followed by the author's contributions towards its implementation in full-potential basis sets. In particular, we address the challenge of applying the principle of locality for identifying correlated subspaces within a material, within which DMFT is used to provide an accurate description of correlations.

3.1 Density Functional Theory

Density functional theory is one of the foundational techniques used by physicists and chemists to realistically model quantum mechanical systems. The approach is often called first-principles or *ab initio* because no free parameters are needed beyond the specification of the nuclear locations and atomic numbers. DFT can be implemented both in real space to describe isolated molecules, and in momentum space for crystal lattices. The key output of DFT is insight into the ground state (zero temperature) properties, including the charge density, equilibrium structure, binding energies, and in the case of weakly-correlated materials, reasonable bandstructures and band gaps. The reason for DFTs enormous impact lies in its low computational effort: results for simple materials can be obtained on a modern laptop in under an hour and for complicated structures in a few days on a moderately-sized computer cluster of a hundred CPUs.

In this section on DFT, we briefly describe its theoretical foundations as first derived by Hohenberg and Kohn [11], and Kohn and Sham [12]. We start from the “standard model” of solid state physics, describing a (nonrelativistic) lattice of nuclei and their associated electrons:

$$\begin{aligned}
 H = & -\frac{\hbar^2}{2m_e} \sum_i \nabla_i^2 - \frac{\hbar^2}{2M_I} \sum_I \nabla_I^2 \\
 & + \frac{1}{2} \sum_{i \neq j} \frac{e^2}{|\mathbf{r}_i - \mathbf{r}_j|} + \sum_{i,I} \frac{e^2 Z_I}{|\mathbf{r}_i - \mathbf{R}_I|} + \frac{1}{2} \sum_{I \neq J} \frac{e^2 Z_I Z_J}{|\mathbf{R}_I - \mathbf{R}_J|},
 \end{aligned} \tag{3.1}$$

where m_e and \mathbf{r}_i are the mass and position of the i -th electron, and M_I , Z_I and \mathbf{R}_I are the mass, atomic number and position of the I -th nucleus. The first two terms describe the electronic and nuclear kinetic energies, while the last three describe the Coulomb interaction between the particles.

Since the nuclear masses are at least three orders of magnitude larger than the electron mass, we can first hold the nuclei fixed and the electrons quantum mechanically, then compute the quantum mechanical motion of the nuclei in the effective potential generated by the electrons. This two-step technique is called the Born-Oppenheimer approximation. In electronic structure calculations with DFT, we only consider the first

step, which simply means removing the nuclear kinetic energy from the hamiltonian:

$$H = -\frac{\hbar^2}{2m_e} \sum_i \nabla_i^2 + \frac{1}{2} \sum_{i \neq j} \frac{e^2}{|\mathbf{r}_i - \mathbf{r}_j|} + \sum_i V_{\text{ext}}(\mathbf{r}_i) + E_{\text{ion}} \quad (3.2)$$

where E_{ion} is the constant term arising from the inter-nuclei Coulomb repulsion and

$$V_{\text{ext}}(\mathbf{r}) = \sum_I \frac{e^2 Z_I}{|\mathbf{r} - \mathbf{R}_I|} \quad (3.3)$$

is the external potential created by the nuclei.

The brute force route would be to solve the Schrödinger equation $H|\Psi\rangle = E|\Psi\rangle$ for the many-body wavefunction $|\Psi\rangle$, an enormously difficult task. Hohenberg and Kohn [11] proposed a new point of view: instead of the wavefunction Ψ , use the charge density

$$n(\mathbf{r}) = \langle \Psi | \psi^\dagger(\mathbf{r}) \psi(\mathbf{r}) | \Psi \rangle \quad (3.4)$$

as the basic variable. The reduction in complexity is drastic: instead of working with a $3N$ -dimensional object, we can manipulate just the 3-dimensional density function. Hohenberg and Kohn proved two basic theorems which create the foundation for DFT.

In what has become known as the Hohenberg-Kohn theorem, they showed that the many-body ground state $|\Psi\rangle$ is uniquely determined by $n(\mathbf{r})$, and vice versa. The proof proceeds by contradiction. Assume that two external potentials $V_{\text{ext}}(\mathbf{r})$ and $V'_{\text{ext}}(\mathbf{r})$, when plugged into the Schrödinger equation, give the same charge density $n(\mathbf{r})$. Label the two hamiltonians constructed from the two external potentials by H and H' , the corresponding ground states $|\Psi\rangle$ and $|\Psi'\rangle$, and their energies E and E' . Let us construct an inequality between the two energies:

$$E' = \langle \Psi' | H' | \Psi' \rangle < \langle \Psi | H' | \Psi \rangle = \langle \Psi | H + V'_{\text{ext}} - V_{\text{ext}} | \Psi \rangle. \quad (3.5)$$

The inequality holds because $|\Psi\rangle$ is not the ground state of H' . Thus we have the relation

$$E' < E + \int d\mathbf{r} (V'_{\text{ext}}(\mathbf{r}) - V_{\text{ext}}(\mathbf{r})) n(\mathbf{r}) \quad (3.6)$$

between the two energies. Exchanging the primes in the above derivation, we get

$$E < E' + \int d\mathbf{r} (V_{\text{ext}}(\mathbf{r}) - V'_{\text{ext}}(\mathbf{r})) n(\mathbf{r}), \quad (3.7)$$

since we assumed that $n(\mathbf{r})$ and $n'(\mathbf{r})$ were equal. Adding these two equations, we arrive at a contradiction:

$$E + E' < E + E'. \quad (3.8)$$

Thus the charge density $n(\mathbf{r})$ uniquely determines the potential $V_{\text{ext}}(\mathbf{r})$, and thus the many-body ground state $|\Psi\rangle$. The converse is simple, since Eq. 3.4 uniquely prescribes how the density is related to the wavefunction.

Hohenberg and Kohn proved a second, variational principle. It states that there exists a universal functional $F[n]$ of the charge density such that the functional

$$E[n] = F[n] + \int d\mathbf{r} n(\mathbf{r}) V_{\text{ext}}(\mathbf{r}) + E_{\text{ion}}, \quad (3.9)$$

for fixed particle number, is minimized for the ground state density, and takes on the value of the ground state energy at the minimum. The proof proceeds by construction. Since the ground state wavefunction is a functional of the density $|\Psi\rangle = |\Psi[n]\rangle$, we define the functional

$$F[n] = -\frac{\hbar^2}{2m_e} \sum_i \langle \Psi[n] | \nabla_i^2 | \Psi[n] \rangle + \frac{1}{2} \sum_{i \neq j} \langle \Psi[n] | \frac{e^2}{|\mathbf{r}_i - \mathbf{r}_j|} | \Psi[n] \rangle. \quad (3.10)$$

This functional is clearly independent of V_{ext} , and thus is a fundamental property of the interacting electron fluid, capturing the kinetic and Coulomb potential energies. The functional $E[n]$ defined above is just the expectational value of the Hamiltonian in the state $|\Psi\rangle$, and since $|\Psi\rangle$ is uniquely determined by the density $n(\mathbf{r})$ due to the Hohenberg-Kohn theorem, $E[n]$ is minimized at the ground state density and takes on the value of the ground state energy at its minimum. The expression of the ground state energy as a functional of the charge density gives DFT its name.

If a sufficiently simple expression for $F[n]$ were known, the problem of determining the ground state energy and density in a given external potential would be easy, since it only requires the minimization of a functional of the 3-dimensional density function. We can write an explicit expression for one contribution to $F[n]$: the Hartree component of the Coulomb energy

$$F[n] = \frac{e^2}{2} \int d\mathbf{r} d\mathbf{r}' \frac{n(\mathbf{r})n(\mathbf{r}')}{|\mathbf{r} - \mathbf{r}'|} + G[n] \quad (3.11)$$

Here $G[n]$ describes the kinetic energy and the portion of the potential energy not captured by the Hartree term. Finding a good expression for $G[n]$ is a challenge.

The current, practical implementations of DFT owe their existence to Kohn and Sham [12], who proposed the following expression:

$$G[n] = T_s[n] + E_{xc}[n], \quad (3.12)$$

where $T_s[n]$ is the kinetic energy of an auxiliary system of noninteracting electrons with density $n(\mathbf{r})$ and $E_{xc}[n]$ is the exchange and correlation energies of an interacting system with density $n(\mathbf{r})$. Furthermore, they proposed to approximate $E_{xc}[n]$ by the expression

$$E_{xc}[n] = \int d\mathbf{r} n(\mathbf{r}) \epsilon_{xc}(n(\mathbf{r})), \quad (3.13)$$

where $\epsilon_{xc}(n)$ is the exchange and correlation energy per electron. The key physical assumption is that the exchange and correlation energies can be well-approximated to be local, depending on the charge density at only one point in space.¹ Usually, the function $\epsilon_{xc}(n)$ is computed once for a uniform electron gas for a range of densities n using many-body techniques, e.g. quantum monte carlo [32], then applied in each DFT calculation. Kohn and Sham's form for $E_{xc}[n]$ is called the local density approximation (LDA), a term which has become synonymous with DFT in colloquial usage. LDA produces unphysical results in strongly-correlated systems, and we discuss a more appropriate approximation in Section 3.3.

To understand more explicitly how the auxiliary noninteracting electrons are introduced to represent the kinetic energy, consider the hamiltonian for N noninteracting particles,

$$H = \sum_i^N \left[-\frac{\hbar^2}{2m_e} \nabla_i^2 + V_{KS}(\mathbf{r}_i) \right], \quad (3.14)$$

where the Kohn-Sham potential $V_{KS}(\mathbf{r})$ will be specified later. To find the ground state density, we solve for the N lowest single-particle eigenstates $|\phi_i\rangle$ and eigenenergies ϵ_i via the Kohn-Sham Schrödinger equation,

$$\left[-\frac{\hbar^2}{2m_e} \nabla^2 + V_{KS}(\mathbf{r}) \right] |\phi_i\rangle = \epsilon_i |\phi_i\rangle, \quad (3.15)$$

¹For example, a non-local density approximation would be $E_{xc}[n] = \int d\mathbf{r} d\mathbf{r}' n(\mathbf{r}) K(\mathbf{r}, \mathbf{r}') n(\mathbf{r}')$, for some function $K(\mathbf{r}, \mathbf{r}')$.

and form the sum of these N lowest eigenstates

$$n(\mathbf{r}) = \sum_{i=1}^N |\phi_i(\mathbf{r})|^2. \quad (3.16)$$

The assumption that the many-body ground state density could be represented by the sum of noninteracting eigenstates lacks rigorous proof, but works well in practice. Now that the system is represented both as a set of Kohn-Sham states $|\phi_i\rangle$ and as a density $n(\mathbf{r})$, we can evaluate the kinetic energy term in the functional $G[n]$ via the standard expression

$$T_s[n] = -\frac{\hbar^2}{2m_e} \sum_{i=1}^N \int d\mathbf{r} \phi_i^*(\mathbf{r}) \nabla^2 \phi_i(\mathbf{r}), \quad (3.17)$$

which is much simpler than attempting to find an expression in terms of the density, even though it is guaranteed to exist.²

How is V_{KS} chosen so that the solution of the Kohn-Sham Schrödinger equation gives the ground state density and energy derived from the functional approach of Hohenberg and Kohn? To derive the result, we use the stationary property of $E[n]$. Since the density is represented in terms of the Kohn-Sham states, we use the chain rule and vary the functional against (the conjugate) $\phi_i^*(\mathbf{r})$:

$$0 = \frac{\delta}{\delta \phi_i^*} \left(E[n] - \sum_{j=1}^N \epsilon_j (\phi_j^* \phi_j - 1) \right), \quad (3.18)$$

where we fix normalization of the states ϕ_i via a Lagrange multipliers ϵ_i . Doing the algebra, we obtain precisely the Kohn-Sham equation 3.14 with the Kohn-Sham potential given by

$$V_{\text{KS}}(\mathbf{r}) = V_{\text{ext}}(\mathbf{r}) + \int d\mathbf{r}' \frac{e^2}{|\mathbf{r} - \mathbf{r}'|} n(\mathbf{r}') + V_{\text{xc}}(\mathbf{r}), \quad (3.19)$$

where the LDA exchange-correlation potential is

$$V_{\text{xc}}(\mathbf{r}) = \frac{d(n(\mathbf{r})\epsilon_{\text{xc}}(n(\mathbf{r})))}{dn(\mathbf{r})} \quad (3.20)$$

The reformulation in terms of an auxiliary Schrödinger equation and the local density approximation are the two key contributions of the Kohn-Sham paper which transformed DFT into practical computational tool. Computationally, the minimization of

²See, for example, the Thomas-Fermi approximation.

the functional $E[n]$ has been replaced by the simpler and standard task of solving an eigenvalue problem. Since the Kohn-Sham potential V_{KS} depends on the density, the equation is nonlinear and the solution is found iteratively. A trial density $n_0(\mathbf{r})$ is chosen and used to construct the potential V_{KS} . The eigenvalue equation is solved for the eigenstates $|\phi_i\rangle$, from which a new density $n_1(\mathbf{r})$ is constructed. The process is iterated until the charge difference falls below a chosen threshold. From the converged results, the ground state energy is computed via

$$E = \sum_i \epsilon_i - \frac{e^2}{2} \int d\mathbf{r} d\mathbf{r}' \frac{n(\mathbf{r})n(\mathbf{r}')}{|\mathbf{r} - \mathbf{r}'|} + E_{\text{xc}}[n] - \int d\mathbf{r} n(\mathbf{r})V_{\text{xc}}(\mathbf{r}), \quad (3.21)$$

which is derived by multiplying the Kohn-Sham equation 3.14 from the left by $\langle\phi_i|$ and summing over i .

It is important to note that the Kohn-Sham eigenvalues ϵ_i and eigenstates $|\phi_i\rangle$, in principle, are not physical. They were introduced only as a practical method for representing the kinetic energy and to allow for simple approximations to E_{xc} . This point demonstrated even more clearly by the fact that the energy is not simply the sum of the eigenvalues ϵ_i , but must be evaluated via Eq. 3.21. However, for weakly-correlated system, the Kohn-Sham energies are a good representation of the actual electronic bandstructure which compares well with experiment.

3.2 Full-Potential Methods

We seek to find a DFT implementation of high accuracy as a starting point to build our DFT+DMFT implementation. When the DFT formalism is applied to crystals, the lattice potentials, charge density and Kohn-Sham states must be represented on some discrete mesh in some chosen basis so that the computer can diagonalize the matrix constructed. The goal is to choose a basis which captures as much structure with as few mesh points possible. One popular basis is planewaves. The Kohn-Sham equations are mathematically simple to formulate in this basis, but they are not very efficient for describing the rapid spatial variation of potentials, densities and wavefunctions near the atomic nuclei, requiring a huge number of basis states. Pseudopotential methods have alleviated this problem [33, 34], but the challenge of generating good pseudopotentials,

especially for the f -shell elements crucial for strongly-correlated physics, renders this technique less than ideal for DFT+DMFT.

Let us enumerate the various choices of bases in a crystal characterized by discrete translational symmetry. Two obvious bases are Bloch states $|n\mathbf{k}\rangle$, and planewaves, which we write as $|\mathbf{k}\mathbf{K}\rangle$ where \mathbf{k} runs over the first Brillouin zone and the discrete \mathbf{K} runs over multiples of the reciprocal lattice vectors. The dual to the planewave basis is the real space basis $|\mathbf{R}\mathbf{r}\rangle$, where \mathbf{r} runs over the first unit cell and \mathbf{R} is discrete and runs over multiples of the real-space lattice vectors. In the augmented planewave family of methods, which we will introduce shortly, we define spherical volumes of space called muffin-tins around each atom in the unit cell, which we will index by τ . If we wish to faithfully represent only the Hilbert space contained within the MTs, we can replace \mathbf{r} with the set of indices $(\tau\kappa lm)$ which we will call the DMFT basis. Conceptually, we imagine a new basis within the τ -th MT, defined in terms of the spherical harmonics (lm) and some complete set of radial functions indexed by κ :

$$\langle \mathbf{r} | \mathbf{R} \tau \kappa l m \rangle = u_l^{\tau\kappa}(r_\tau) Y_{lm}(\hat{\mathbf{r}}_\tau) \quad (3.22)$$

Here $\mathbf{r}_\tau = \mathbf{r} - \vec{\tau}$ is the position vector inside the τ -th MT sphere. Thus, we have the following list of equivalent basis sets spanning the Hilbert space within the MTs:

$$|n\mathbf{k}\sigma\rangle \leftrightarrow |\mathbf{k}\mathbf{K}\sigma\rangle \leftrightarrow |\mathbf{R}\mathbf{r}\sigma\rangle \leftrightarrow |\mathbf{R}\tau\kappa lm\sigma\rangle, \quad (3.23)$$

where we have reintroduced spin. For notational convenience, we define an aggregate orbital index $L \equiv (lm\sigma)$ and a single crystal-wide index $\alpha \equiv (\mathbf{R}\tau)$ for all MTs, so the DMFT basis is written $|\alpha\kappa L\rangle$.

The DMFT basis is not orthonormal. This fact originates from the radial functions $u_l^{\tau\kappa}$ are often neither orthogonal nor normalized in the κ subspace. In Appendix A, we describe in more detail the standard issues and establish the notation we use to represent nonorthonormal bases. For example, unity in the DMFT basis is

$$1 = \sum_{\alpha\kappa L} |\alpha\kappa L\rangle \langle \alpha\bar{\kappa} L|, \quad (3.24)$$

where the bar denotes the dual basis.

For our DFT+DMFT implementation, we chose to build off of a DFT code written in the augmented planewave (APW) basis (for an invaluable introduction and technical details, see Ref. [35]). This method is one of the most accurate types of DFT, as no approximations are made to the lattice potential near the atomic nuclei, hence the term “full-potential”. The APW methods are capable of accurately describing the rapid variations of wavefunctions near the nuclei as well as relativistic effects (spin-orbit physics) which dominate the behavior of the late d -shell and f -shell elements. In the APW formalism, the space within the crystal is partitioned into muffin-tins (MTs) centered about the atomic nuclei, and the interstitials comprised of the space between the muffin-tins. The size of the muffin-tins are specified by an input parameter, the muffin-tin radius R_{MT} , chosen so that the MTs of different atoms do not overlap.

The idea of the APW basis is to match the basis set to the spatial structure of the wavefunction. In the interstitials, where the lattice potential varies slowly, plane waves are a good choice. Near the atomic nuclei, the strong effect of the nuclear Coulomb potential causes the wavefunctions to behave like the solutions of the atomic Schrödinger equation, so we “augment” the plane waves and use spherical harmonics and radial solutions to the Schrödinger equation as a basis within the MTs. Matching the plane waves to the atomic-like basis at the MT boundary is accomplished by the formula for expanding plane waves in terms of spherical harmonics

$$e^{i\mathbf{k}\mathbf{r}} = 4\pi \sum_L i^l j_l(kr) Y_L^*(\hat{\mathbf{k}}) Y_L(\hat{\mathbf{r}}), \quad (3.25)$$

where j_l are the spherical Bessel functions. With this motivation in mind, the APW basis states are written

$$\chi_{\mathbf{k}+\mathbf{K}}(\mathbf{r}) = \begin{cases} e^{i(\mathbf{k}+\mathbf{K})\cdot\mathbf{r}} & \mathbf{r} \notin S_\tau \\ \sum_{\kappa L} A_{\mathbf{k}+\mathbf{K}}^{\tau\kappa L} u_l^{\tau\kappa}(r_\tau) Y_L(\hat{\mathbf{r}}_\tau) & \mathbf{r} \in S_\tau \end{cases} \quad (3.26)$$

where S_τ denotes the volume of space contained in the muffin-tin around the τ -th atom, and $\mathbf{r}_\tau = \mathbf{r} - \vec{\tau}$ is the coordinate vector with its origin at the τ -th atom. Here, Y_L are the spherical harmonics and $u_l^{\tau\kappa}$ are radial functions, which are generally chosen to be the regular solutions to the atomic Schrödinger equation at a chosen energies $E_l^{\tau\kappa}$

within the MT. The coefficients $A_{\mathbf{k}+\mathbf{K}}^{\tau\kappa L}$ are fixed by the requirement that the interstitial planewaves smoothly match the atomic-like basis via Eq. 3.25:

$$A_{\mathbf{k}+\mathbf{K}}^{\tau\kappa L} = \frac{4\pi}{u_l^{\tau\kappa}(R_{\text{MT}}^\tau)} j_l(|\mathbf{k} + \mathbf{K}| R_{\text{MT}}^\tau) Y_L^*(\widehat{\mathbf{k} + \mathbf{K}}) \quad (3.27)$$

We note that the APW basis transforms like planewaves under crystal symmetries.

When we diagonalize the Kohn-Sham equation, the resulting Kohn-Sham eigenstates $\psi_{n\mathbf{k}}(\mathbf{r})$ are superpositions of the basis functions

$$\psi_{n\mathbf{k}}(\mathbf{r}) = \sum_{\mathbf{K}} C_{n\mathbf{k}}^{\mathbf{K}} \chi_{\mathbf{k}+\mathbf{K}}(\mathbf{r}) = \begin{cases} u_{n\mathbf{k}}(\mathbf{r}) e^{i\mathbf{k}\cdot\mathbf{r}} & \mathbf{r} \notin S_\tau \\ \sum_{\kappa L} \mathcal{A}_{n\mathbf{k}}^{\tau\kappa L} u_l^{\tau\kappa}(r_\tau) Y_L(\hat{\mathbf{r}}_\tau) & \mathbf{r} \in S_\tau \end{cases} \quad (3.28)$$

Here, we have defined

$$u_{n\mathbf{k}}(\mathbf{r}) = \sum_{\mathbf{K}} C_{n\mathbf{k}}^{\mathbf{K}} e^{i\mathbf{K}\cdot\mathbf{r}} \quad (3.29)$$

$$\mathcal{A}_{n\mathbf{k}}^{\tau\kappa L} = \sum_{\mathbf{K}} A_{\mathbf{k}+\mathbf{K}}^{\tau\kappa L} C_{n\mathbf{k}}^{\mathbf{K}} \quad (3.30)$$

With these definitions, we can write explicitly several key physical quantities. The Kohn-Sham Green's function is

$$\hat{G}(\omega) = \sum_{n\mathbf{k}\sigma} |n\mathbf{k}\sigma\rangle \frac{1}{\omega + \mu - \epsilon_{n\mathbf{k}\sigma}} \langle n\mathbf{k}\sigma|. \quad (3.31)$$

The density of states is

$$\rho(\omega) = -\frac{1}{\pi} \text{Im tr } \hat{G}(\omega) = \sum_{n\mathbf{k}\sigma} \delta(\omega + \mu - \epsilon_{n\mathbf{k}\sigma}). \quad (3.32)$$

Projections onto a subspace, for example the projection onto a given orbital L in the α -th MT sphere, can be written

$$P_{\alpha L} = \sum_{\kappa} |\alpha\kappa L\rangle \langle \alpha\bar{\kappa} L|. \quad (3.33)$$

Then, the (partial) Green's function in this subspace is simply $\hat{G}_{\alpha L}(\omega) = P_{\alpha L} \hat{G}(\omega) P_{\alpha L}$ and the partial density of states is

$$\rho_{\alpha L}(\omega) = -\frac{1}{\pi} \text{Im tr } P_{\alpha L} \hat{G}(\omega) P_{\alpha L} \quad (3.34)$$

$$= \sum_{\kappa} \sum_{n\mathbf{k}\sigma} \langle \alpha\bar{\kappa} L | n\mathbf{k}\sigma \rangle \delta(\omega + \mu - \epsilon_{n\mathbf{k}\sigma}) \langle n\mathbf{k}\sigma | \alpha\kappa L \rangle. \quad (3.35)$$

The matrix elements appearing in the density of states often recur so we introduce the following notation for them:

$$A_{n\mathbf{k}\sigma}^{\alpha\bar{\kappa}L} = \langle \alpha\bar{\kappa}L | n\mathbf{k}\sigma \rangle \quad \text{or equivalently} \quad |n\mathbf{k}\sigma\rangle = \sum_{\alpha\bar{\kappa}L} A_{n\mathbf{k}\sigma}^{\alpha\bar{\kappa}L} |\alpha\bar{\kappa}L\rangle. \quad (3.36)$$

For example, with this notation, the partial density of states becomes

$$\rho_{\alpha L}(\omega) = \sum_{\kappa} \sum_{n\mathbf{k}\sigma} A_{n\mathbf{k}\sigma}^{\alpha\bar{\kappa}L} A_{n\mathbf{k}\sigma}^{*\alpha\bar{\kappa}'L} \delta(\omega + \mu - \epsilon_{n\mathbf{k}\sigma}) \quad (3.37)$$

$$= \sum_{\kappa\kappa'} \sum_{n\mathbf{k}\sigma} A_{n\mathbf{k}\sigma}^{\alpha\bar{\kappa}L} A_{n\mathbf{k}\sigma}^{*\alpha\bar{\kappa}'L} \langle u_l^{\alpha\kappa'} | u_l^{\alpha\kappa} \rangle \delta(\omega + \mu - \epsilon_{n\mathbf{k}\sigma}). \quad (3.38)$$

Generally, if we want to write the matrix elements exclusively in either the original or the dual basis, we will get factors of the overlap $S \sim \langle u_l^{\alpha\kappa'} | u_l^{\alpha\kappa} \rangle$.

3.3 The Locality Principle: Projection and Embedding

The main conceptual challenge to combining DFT with DMFT lies in the delineation of the correlated subspace, a hurdle which does not exist in the application of DMFT to model hamiltonians. We seek to use DMFT to model the effect of strong-correlations within the localized d and f orbitals. However, in a real material, the d and f orbitals are embedded in a medium composed of the weakly-correlated s and p shells, and electrons freely hop between the two subspaces due to orbital overlaps. In fact, formally it makes no sense to speak of s - p - d - f orbitals because these concepts are only well-defined in systems with continuous rotational symmetry, like an isolated atom. How should we partition the Hilbert space into a weakly-correlated subspace and a strongly-correlated subspace, to which we apply DMFT?

The principle which underlies the local density approximation and DFT+DMFT is locality. In weakly-correlated materials, Coulomb interaction is strongly screened and the behavior of electrons at two different points in space are essentially uncorrelated. LDA exploits this fact and approximates the dependence of the exchange and correlation energies on the charge density as completely local in space. In strongly-correlated materials, the behavior of electrons in the weakly-correlated s and p bands are still well-described by LDA. However, embedded in this weakly-correlated medium are regions

of electronic density where the electrons cannot be treated as independent particles. A simple concrete example is the d -shells in the oxide V_2O_3 : disturbing the density at one spatial point of a d -orbital strongly perturbs the electrons in the rest of the d -orbital. We envision this d -orbital as the fundamental *correlated local object* in the material V_2O_3 . The local correlated objects need not correspond to the atomic orbital: in materials where atoms dimerize, for example VO_2 , the fundamental object is a pair of atoms. In molecules, the molecular orbitals constitute the correlated objects. In summary, the spatially pointwise locality of LDA is replaced by locality of discrete correlated subspaces.

Implementations of LDA+DMFT must provide tools for identifying these local correlated objects. Once identified, DMFT is used to treat the interactions in the subspace spanned by these local objects, and it does so exactly since QMC methods sum up all local diagrams. The remaining weakly-correlated subspace is treated with DFT. In applications of DMFT to crystalline solids, current implementations identify atomic-like orbitals of the d or f elements as the local correlated objects, but we stress the concept of locality is general.

In addition to locality, an implementation of DFT+DMFT must specify the form of the interactions within the local correlated subspace. In a correlated material, the Coulomb interaction within the identified local orbitals, while strong, are screened by the weakly-correlated s and p bands. Choosing atomic-like orbitals allows us to use intuition from atomic physics to specify a reasonable form of the Coulomb interaction via renormalized Slater integrals. In practice, we renormalize F^2 , F^4 and F^6 by about 30%, and F^0 is strongly screened, and can be computed, for example, via constrained LDA [36]. The concepts and algorithms for computing the interaction strength within correlated subspaces remain under active development [37, 38].

DMFT solves a local impurity problem, defined through the self-consistency condition

$$\hat{G}_{\text{imp}}(\omega) = \sum_{LL'} |L\rangle \left(\frac{1}{\omega - E_{\text{imp}} - \Delta - \Sigma} \right)_{LL'} \langle L'| = \hat{P} \hat{G}(\omega). \quad (3.39)$$

The states $|L\rangle$ span the space of the local correlated object which has been mapped

to an impurity problem. The operator \hat{P} implements the *projection* of the correlated electron subspace G_{imp} out from the full lattice Green's function G :

$$G_{\text{imp}} = \hat{P}G. \quad (3.40)$$

The reverse operation \hat{E} of inserting the local time-dependent self-energy Σ_{imp} , the result of the DMFT solution of the local impurity problem, back into the lattice to give the lattice self-energy Σ is called *embedding*:

$$\Sigma = \hat{E}\Sigma_{\text{imp}}. \quad (3.41)$$

The various DFT+DMFT implementations differ not only in the choice of local states, but also in the choice of the projection-embedding step.

Projection and embedding connect the atomic physics with the solid state physics. DFT+DMFT effectively creates a translation table between atomic physics and the lattice. For example, if the impurity solution exhibits a Kondo peak, this implies the presence of heavy quasiparticles in the lattice. If original DFT solution was metallic, but the solution of the DFT+DMFT impurity problem is gapped, then we have a Mott insulator. Finally, if the impurity acquires a magnetic moment, this implies long-ranged magnetic order in the lattice. The solution of the impurity problem is strongly dependent on its valence, which is controlled by the quantity of charge defined as correlated in the projection step. Thus, one stringent check of the physical reasonableness of a projection-embedding scheme is to examine the valence of the solution, which can be compared against experiment (for example, X-ray absorption spectroscopy). The chosen projector must map to the correct Anderson impurity model!

Various choices of orbitals spanning the correlated subspace have been proposed in the literature, including tight-binding LMTO's [39, 40], non-orthogonal LMTO's [41], Nth-order Muffin-Tin orbitals [42], numerically-orthogonalized LMTO's [43], and maximally-localized Wannier orbitals [44, 45]. Maximally-localized Wannier orbitals are appealing because of their elegant mathematical properties [46]. However, our experience has been that the extracted valence is often too large, especially for materials which are not extremely localized. Localized basis sets are a better starting point, but

their non-orthogonality pose a challenge. Straightforward orthogonalization mixes the angular character of the orbitals, leading to incorrect electron counts in each angular momentum shell. For example, within modern DFT implementations, cerium metal has approximately one $4f$ electron. Naïve orthogonalization results in a considerably higher $4f$ electron count, causing the lattice to be mapped to an unphysical impurity problem.

Even more challenging is the formulation of the correlated orbitals in APW basis sets. Multiple basis functions, indexed by κ , are used in a single angular momentum channel to provide enough variational freedom to accurately describe the bands. To implement DMFT in such basis sets, the group of orbitals representing the correlated electrons in the solid must be contracted to form a single set of atomic-like orbitals. How should we collapse the κ space onto a single orbital?

Below we enumerate three proposals for the projection \hat{P} and embedding \hat{E} operations. The first two are used in the current literature, and the last is our own. We have implemented all three in our code.

$$\hat{G}_{\text{imp}}^{\alpha}(\omega) = \sum_{\kappa} P_{\alpha\kappa}^0 \hat{G}(\omega) P_{\alpha\kappa}^0 \quad \hat{\Sigma}(\omega) = \sum_{\alpha\kappa} P_{\alpha\kappa}^0 \hat{\Sigma}_{\text{imp}}^{\alpha}(\omega) P_{\alpha\kappa}^0 \quad (3.42)$$

$$\hat{G}_{\text{imp}}^{\alpha}(\omega) = P_{\alpha}^1 \hat{G}(\omega) P_{\alpha}^1 \quad \hat{\Sigma}(\omega) = \sum_{\alpha} P_{\alpha}^1 \hat{\Sigma}_{\text{imp}}^{\alpha}(\omega) P_{\alpha}^1 \quad (3.43)$$

$$\hat{G}_{\text{imp}}^{\alpha}(\omega) = P_{\alpha}^2 \hat{G}(\omega) P_{\alpha}^{2\dagger} \quad \hat{\Sigma}(\omega) = \sum_{\alpha} P_{\alpha}^{2\dagger} \hat{\Sigma}_{\text{imp}}^{\alpha}(\omega) P_{\alpha}^2 \quad (3.44)$$

where the projection operators (not to be confused with the symbol \hat{P} for the general concept of projection) are

$$P_{\alpha\kappa}^0 = \sum_L |\alpha\kappa L\rangle \langle \alpha\bar{\kappa} L| \quad (3.45)$$

$$P_{\alpha}^1 = \sum_L |\alpha 0 L\rangle \langle \alpha \bar{0} L| \quad (3.46)$$

$$P_{\alpha}^2 = \sum_L \sum_{n\mathbf{k}\sigma} |\alpha 0 L\rangle A_{n\mathbf{k}\sigma}^{\alpha\bar{0}L} f_{n\mathbf{k}\sigma}^{\alpha L} \langle n\mathbf{k}\sigma| \quad (3.47)$$

and the coefficients for our projection scheme are

$$f_{n\mathbf{k}\sigma}^{\alpha L} = \sqrt{\frac{\sum_{\kappa} A_{n\mathbf{k}\sigma}^{\alpha\bar{\kappa}L} A_{n\mathbf{k}\sigma}^{*\alpha\kappa L}}{A_{n\mathbf{k}\sigma}^{\alpha\bar{0}L} A_{n\mathbf{k}\sigma}^{*\alpha 0 L}}}. \quad (3.48)$$

Without loss of generality, we have chosen to project to the zeroth unit cell $\mathbf{R} = \mathbf{0}$ in the above.

The operators P implement the projection and embedding. The first two, $P_{\alpha\kappa}^0$ and P_{α}^1 are true projection operators in the sense of linear algebra, since $P^2 = P$. The third, P_{α}^2 , is not as it has the renormalizing factor $f_{n\mathbf{k}\sigma}^{\alpha L}$ which, as we shall see below, corrects for missing spectral weight. When applied to the lattice Green's function $\hat{G}(\omega)$, the projection operators produce the correlated impurity Green's function at the α -th muffin-tin:

$$\hat{G}_{\text{imp}}^{\alpha}(\omega) = P_{\alpha}\hat{G}(\omega)P_{\alpha}. \quad (3.49)$$

The impurity Green's function lives in the space spanned by the local orbitals $|L\rangle$, which we generalize to index spherical harmonics $|lm\rangle$, cubic harmonics, or relativistic harmonics $|jm_j\rangle$, depending on the system symmetry. We choose this basis to minimize the off-diagonal elements of the correlated Green's function in order to reduce the minus-sign problem in Monte Carlo impurity solvers. The dual operation of embedding is accomplished by inserting the impurity self-energy into every muffin-tin:

$$\hat{\Sigma}(\omega) = \sum_{\alpha} P_{\alpha}\hat{\Sigma}_{\text{imp}}^{\alpha}(\omega)P_{\alpha}. \quad (3.50)$$

The lattice self-energy $\hat{\Sigma}(\omega)$ is nonzero inside every muffin-tin in the crystal. In the common case of single site DMFT for translationally invariant systems, the impurity self-energy is independent of the atom, $\hat{\Sigma}_{\text{imp}}^{\alpha} = \hat{\Sigma}_{\text{imp}}$ so we are inserting the same self-energy into each muffin-tin.

All three of the proposed schemes implement atomic-like orbitals, since they project to the local basis, but we believe our proposal is the most advantageous. We judge their quality by asking if they (i) capture all the spectral weight in the given angular momentum channels, (ii) lead to causal DMFT equations, and (iii) preserve angular momentum character.

The first scheme $P_{\alpha\kappa}^0$ integrates all the spectral weight in each angular momentum channel (the sum of κ), thereby projecting purely onto the angular momentum eigenfunctions $|L\rangle$. By construction, this scheme clearly preserves angular momentum character. Additionally, $P_{\alpha\kappa}^0$ captures all the spectral weight: application of Eq. 3.34

to $\hat{G}_{\text{imp}}^\alpha$ will give the same partial density of states as DFT (Eq. 3.37). This projection scheme is attractive for the further reason that summation over κ implies no information is retained about the radial dependence of the self-energy, a fact which meshes with the intuition that the impurity solver within the DMFT should only know about angular character. However, this scheme leads to noncausal DMFT equation, which manifests itself in the imaginary part of the hybridization Δ becoming positive. This can be clearly seen in the case of a diverging self-energy $\Sigma_{\text{imp}}(i\omega_n \sim 0) \rightarrow -i\infty$, as is the case in the Mott insulating state. In this case, the DMFT self-consistency equation simplifies to

$$\frac{1}{\hat{\Sigma}_{\text{imp}}^\alpha + \Delta^\alpha} = \sum_{\kappa} \frac{1}{\hat{\Sigma}_{\text{imp}}^\alpha}. \quad (3.51)$$

Solving for the hybridization gives

$$\Delta^\alpha = \left(\sum_{\kappa} \frac{1}{\hat{\Sigma}_{\text{imp}}^\alpha} \right)^{-1} - \hat{\Sigma}_{\text{imp}}^\alpha = \left(\frac{1}{N_\kappa} - 1 \right) \hat{\Sigma}_{\text{imp}}^\alpha. \quad (3.52)$$

Since the number of local orbitals $N_\kappa > 1$, the coefficient $(N_\kappa^{-1} - 1)$ is negative, so the hybridization becomes noncausal.

We note that the first projection $P_{\alpha\kappa}^0$ is implemented in the QTL package [47] of Wien2K[48]. The LDA+U implementation within Wien2K [49] also uses $P_{\alpha\kappa}^0$, but this does not generate a causality problem since it is only in DFT+DMFT that we must compute the hybridization function. Additionally, simple impurity solvers such as Hubbard-I [50] do not incorporate a true hybridization so they also avoid issues with causality.

The second scheme P_α^1 projects only to $\kappa = 0$ radial state, in addition to the atomic angular momentum channels. Since this scheme truly is a projection operation (no sum over κ), causality is automatically satisfied. However, spectral weight from the $\kappa \geq 1$ orbitals are not captured, as the computation of the partial density of states shows:

$$\rho_{\alpha L}(\omega) = \sum_{n\mathbf{k}\sigma} A_{n\mathbf{k}\sigma}^{\alpha\bar{0}L} A_{n\mathbf{k}\sigma}^{*\alpha 0L} \delta(\omega + \mu - \epsilon_{n\mathbf{k}\sigma}). \quad (3.53)$$

Comparing this with Eq. 3.37 for the DFT partial density of states, we see P_α^1 misses the sum over κ . This scheme does not capture a portion of the electron density which

should be considered correlated, causing the DMFT impurity problem to have the wrong valence.

The strategy we use in the construction of our scheme P_α^2 is to begin with P_α^1 , which is causal, but renormalize the projector elements in such a way that the partial density of states is preserved. This is accomplished by the coefficients $f_{n\mathbf{k}\sigma}^{\alpha L}$. We can check that P_α^2 captures spectral weight by computing the partial density of states:

$$\rho_{\alpha L}(\omega) = -\frac{1}{\pi} \text{Im tr } P_{\alpha L} \hat{G}_{\text{imp}}^\alpha(\omega) P_{\alpha L} = -\frac{1}{\pi} \text{Im tr } P_{\alpha L} \left(P_\alpha^2 \hat{G}_{\text{imp}}^\alpha(\omega) P_\alpha^{2\dagger} \right) P_{\alpha L} \quad (3.54)$$

$$= \sum_L \sum_{n\mathbf{k}\sigma} A_{n\mathbf{k}\sigma}^{\alpha\bar{0}L} f_{n\mathbf{k}\sigma}^{\alpha L} \delta(\omega + \mu - \epsilon_{n\mathbf{k}\sigma}) f_{n\mathbf{k}\sigma}^{\alpha L} A_{n\mathbf{k}\sigma}^{*\alpha 0L} \quad (3.55)$$

The renormalization factors $f_{n\mathbf{k}\sigma}^{\alpha L}$ were chosen so that they would exactly replace the matrix elements

$$(f_{n\mathbf{k}\sigma}^{\alpha L})^2 \cdot A_{n\mathbf{k}\sigma}^{\alpha\bar{0}L} A_{n\mathbf{k}\sigma}^{*\alpha 0L} = \sum_{\kappa} A_{n\mathbf{k}\sigma}^{\alpha\bar{\kappa}L} A_{n\mathbf{k}\sigma}^{*\alpha \kappa L}, \quad (3.56)$$

restoring the sum over κ and reproducing the exact DFT partial density of states. By renormalizing the projector in the Bloch basis $|n\mathbf{k}\sigma\rangle$, we slightly give up purity of angular momentum character in return for capturing all the correlated electron density. We have based our code which implements the projection P_α^2 on the QTL package of P. Novak [47].

All of the above projection schemes lead to a slightly nonorthonormal local basis because (i) we never use complete Bloch states up to infinite energy in practical computation when computing overlaps and inserting resolutions of unity, and (ii) the APW basis is overcomplete. To remedy this loss of spectral weight, we orthonormalize the projector. For example, in the case of P_α^2 , we compute the overlap

$$\mathcal{O}_{LL'}^\alpha = \sum_{n\mathbf{k}\sigma \in \mathcal{L}} \langle \alpha\bar{0}L | P_\alpha^2 | n\mathbf{k}\sigma \rangle \langle n\mathbf{k}\sigma | P_\alpha^{2\dagger} | \alpha 0L' \rangle, \quad (3.57)$$

where \mathcal{L} denotes the Hilbert space of bands, generally specified by an energy window about the Fermi level, that we keep in our DFT+DMFT implementation. Then we symmetrically orthogonalize the projection scheme by replacing projector with

$$(P_\alpha^2)_{n\mathbf{k}\sigma}^L \rightarrow (\tilde{P}_\alpha^2)_{n\mathbf{k}\sigma}^L = \sum_{L'} \left(\frac{1}{\sqrt{\mathcal{O}^\alpha}} \right)_{LL'} \langle \alpha\bar{0}L' | P_\alpha^2 | n\mathbf{k}\sigma \rangle \quad (3.58)$$

which we use to extract the correlated subspace of the full lattice Green's function $G(\omega)$.

Chapter 4

Continuous-Time Quantum Monte Carlo

The Anderson Impurity Model (AIM) is one of the canonical models in condensed matter physics, describing a localized level embedded in a sea of conduction electrons. The motivation for the model arose for the need to describe the magnetic behavior of impurities embedded in metals [51]. It is the simplest example of a strongly-correlated model, with interactions localized onto a single site. The model has stimulated the development of a wealth of physical ideas, only to be paralleled by the number of techniques developed to tackle its solution over its half-century of existence. These include the first perturbative calculations of the Kondo model [52], scaling [53, 54], the numerical renormalization group [55], applications of the Bethe ansatz [21], slave bosons in the context of heavy fermion materials [22] and the Hirsch-Fye quantum Monte Carlo algorithm [25].

The solution of an AIM lies at the heart of every DMFT implementation, and in this chapter, we describe one particularly powerful method for its solution: continuous-time quantum Monte Carlo (CTQMC) [30]. This exact method relies on expanding the partition function of the AIM about the local atomic limit in powers of the hybridization. The expansion is sampled via Monte Carlo importance sampling in the form of the Metropolis-Hastings algorithm. The advantage of this method is its generality and reduced computational time, especially in the strongly-interacting regime relevant for Mott physics.

We begin by deriving the hybridization expansion, followed by the Monte Carlo updates needed to sample the partition function, and conclude with brief comments on

optimizations which allow fast rejections, avoiding the need to perform the expensive atomic-trace computation.

4.1 Hybridization Expansion

The hybridization formalism for performing Monte Carlo simulations of the AIM was first presented in Ref. [27] and extended in Ref. [28] and Ref. [29]. This method is state-of-the-art, replacing the earlier Hirsch-Fye impurity solver, allowing over an order of magnitude lower temperatures in realistic atomic interaction regimes. The term continuous-time arises because there is no discretization of the time domain in CTQMC, as compared previous Monte Carlo schemes like the Hirsch-Fye algorithm, which divided the imaginary time interval $[0, \beta]$ into a fixed number N_τ of time-slices.

We first develop the formalism with spinless fermions to illustrate its essential features before generalizing to spin-ful and multi-orbital systems. The hamiltonian contains three terms,

$$H = H_{\text{imp}} + H_{\text{bath}} + H_{\text{hyb}}, \quad (4.1)$$

describing the impurity, the bath of conduction electrons, and hopping processes hybridizing the two flavors of electrons:

$$H_{\text{imp}} = \epsilon_d d^\dagger d \quad (4.2)$$

$$H_{\text{bath}} = \sum_k \epsilon_k c_k^\dagger c_k \quad (4.3)$$

$$H_{\text{hyb}} = \sum_k V_k c_k^\dagger d + \text{h.c.} \quad (4.4)$$

Throughout the following, we take the bath as the reference system, and ask how the system is modified by the addition of the impurity and hybridization. The quantity we formally manipulate is the partition function, in the path integral representation:

$$Z = \int \mathcal{D}[c^\dagger c d^\dagger d] e^{-S_{\text{imp}} - S_{\text{bath}} - S_{\text{hyb}}} \quad (4.5)$$

Our first goal is to express the partition function solely in terms of the impurity degrees of freedom, which are finite in number and thus amenable to computer simulation.

Since the conduction electrons are non-interacting, we can integrate them out, and the partition function factors into two terms:

$$Z = Z_{\text{bath}} \cdot Z_{\text{imp}} \quad (4.6)$$

$$Z_{\text{bath}} = \prod_{nk\sigma} \beta(-i\omega_n + \epsilon_k) \quad (4.7)$$

$$Z_{\text{imp}} = \int \mathcal{D}[d^\dagger d] e^{-S_{\text{eff}}[d^\dagger, d]} \quad (4.8)$$

The effective action describes the original impurity physics plus an additional term capturing retarded processes where impurity electrons hop into the bath and then return to the impurity:

$$S_{\text{eff}}[d^\dagger, d] = S_{\text{imp}} + \sum_{\sigma} \int_0^{\beta} d\tau \int_0^{\beta} d\tau' d^\dagger(\tau) \Delta(\tau - \tau') d(\tau') \quad (4.9)$$

In the second term, which we denote ΔS , the hybridization function

$$\Delta(i\omega_n) = \sum_k \frac{|V_k|^2}{i\omega_n - \epsilon_k} \quad (4.10)$$

quantifies the strength of hopping at various energies. We have reduced the problem to a finite-sized impurity hamiltonian with the effects of the hopping V_k and conduction bath captured by a single hybridization function $\Delta(i\omega_n)$. We can choose any hybridization of our liking; a flat band, semicircle and lorentzian are three popular choices.

The quantity of interest is Z_{imp} , which captures the perturbation of the impurity on the noninteracting conduction bath. To express the Grassman integration over d and d^\dagger in a manner amenable to computation, we Taylor series expand in the hybridization term:

$$Z_{\text{imp}} = \sum_{k=0}^{\infty} \frac{1}{k!} \int \mathcal{D}[d^\dagger d] e^{-S_{\text{imp}}} (-\Delta S)^k \quad (4.11)$$

$$= Z_0 \sum_{k=0}^{\infty} \frac{1}{k!} \int_0^{\beta} d\tau_1 \cdots d\tau_k \int_0^{\beta} d\tau'_1 \cdots d\tau'_k Z(\tau_1 \cdots \tau_k; \tau'_1 \cdots \tau'_k), \quad (4.12)$$

where the integrand is

$$\begin{aligned} & Z(\tau_1 \cdots \tau_k; \tau'_1 \cdots \tau'_k) \\ &= \left\langle T_{\tau} d(\tau'_1) d^\dagger(\tau_1) \cdots d(\tau'_k) d^\dagger(\tau_k) \right\rangle_0 \cdot \Delta(\tau_1 - \tau'_1) \cdots \Delta(\tau_k - \tau'_k). \end{aligned} \quad (4.13)$$

The minus sign in $-\Delta S$ has been absorbed by reordering $-d^\dagger \Delta d = dd^\dagger \Delta$. We have expressed the Grassman integral over the impurity degrees of freedom using the standard expression for time-ordered correlation functions

$$\int \mathcal{D}[d^\dagger d] e^{-S_{\text{imp}}} \mathcal{O}(\tau_1 \cdots \tau_k) \equiv Z_0 \langle T_\tau \mathcal{O}(\tau_1 \cdots \tau_k) \rangle_0, \quad (4.14)$$

where the normalization

$$Z_0 = \int \mathcal{D}[d^\dagger d] e^{-S_{\text{imp}}} \quad (4.15)$$

is the impurity partition function.

As formulated, the integrands in the hybridization expansion can be both negative and positive, and thus the series cannot be efficiently sampled via Monte Carlo. The solution is to group together all the diagrams at a given expansion order k in the form of a determinant. We show this grouping explicitly for the second-order term:

$$\frac{1}{2!} \int_0^\beta d\tau_1 d\tau_2 \int_0^\beta d\tau'_1 d\tau'_2 \left\langle T_\tau d(\tau'_1) d^\dagger(\tau_1) d(\tau'_2) d^\dagger(\tau_2) \right\rangle_0 \cdot \Delta(\tau_1 - \tau'_1) \Delta(\tau_2 - \tau'_2) \quad (4.16)$$

Considering just the un-primed τ_i integrals, there are two wedges in the integral phase space defined by $W = \{(\tau_1, \tau_2) : \tau_1 < \tau_2\}$ and vice versa. The idea is to convert the un-primed integrals from over both wedges into an integral over just one wedge:

$$\int_0^\beta d\tau_1 d\tau_2 f(\tau_1, \tau_2) = \int_0^\beta d\tau_1 \int_{\tau_1}^\beta d\tau_2 f(\tau_1, \tau_2) + \int_{\tau_2}^\beta d\tau_1 \int_0^\beta d\tau_2 f(\tau_1, \tau_2) \quad (4.17)$$

$$= \int_0^\beta d\tau_1 \int_{\tau_1}^\beta d\tau_2 [f(\tau_1, \tau_2) + f(\tau_2, \tau_1)] \quad (4.18)$$

The price we pay the integrand becomes a sum of two terms. When we swap the two times in the time-ordered impurity trace, we can reorder the operators and get sign corresponding to the parity of the permutation, in this case a single minus sign:

$$\left\langle T_\tau d(\tau'_1) d^\dagger(\tau_2) d(\tau'_2) d^\dagger(\tau_1) \right\rangle_0 = - \left\langle T_\tau d(\tau'_1) d^\dagger(\tau_1) d(\tau'_2) d^\dagger(\tau_2) \right\rangle_0 \quad (4.19)$$

The impurity trace factors out of the two terms in the integrand. The minus sign combined with the swap in arguments in the hybridization functions $\Delta(\tau_i - \tau_j)$ gives

the determinant:

$$\frac{1}{2!} \int_0^\beta d\tau_1 \int_{\tau_1}^\beta d\tau_2 \int_0^\beta d\tau'_1 \int_0^\beta d\tau'_2 \left\langle T_\tau d(\tau'_1) d^\dagger(\tau_1) d(\tau'_2) d^\dagger(\tau_2) \right\rangle_0 \\ \times \det \begin{pmatrix} \Delta(\tau_1 - \tau'_1) & \Delta(\tau_1 - \tau'_2) \\ \Delta(\tau_2 - \tau'_1) & \Delta(\tau_2 - \tau'_2) \end{pmatrix} \quad (4.20)$$

Finally, we can absorb the $1/2!$ prefactor by again replacing the integral over the primed imaginary times τ'_i by an integral over a single wedge. This time, the integrand is invariant under permutations of the times τ'_1 and τ'_2 because both the impurity trace and the determinant are antisymmetric objects—the impurity trace acquires a minus sign when two operators are swapped while the determinant acquires a minus sign when two columns are swapped. Thus, our final formula at second-order is

$$\int_W d\tau_1 d\tau_2 \int_W d\tau'_1 d\tau'_2 \left\langle T_\tau d(\tau'_1) d^\dagger(\tau_1) d(\tau'_2) d^\dagger(\tau_2) \right\rangle_0 \cdot \det M^{-1}(\{\tau_i\}, \{\tau_j\}) \quad (4.21)$$

where we have defined the hybridization matrix $(M^{-1})_{ij} = \Delta(\tau_i - \tau'_j)$. We write M^{-1} because it will prove simpler to manipulate its inverse in the following.

Generalizing this argument to an arbitrary perturbation order k , we arrive at the hybridization expansion of the partition function amenable for Monte Carlo sampling:

$$Z_{\text{imp}} = Z_0 \sum_{k=0}^{\infty} \int_W d\tau_1 \cdots d\tau_k \int_W d\tau'_1 \cdots d\tau'_k Z(\tau_1 \cdots \tau_k; \tau'_1 \cdots \tau'_k), \quad (4.22)$$

where the integration region is a wedge $W = \{(\tau_1, \dots, \tau_k) : \tau_1 < \dots < \tau_k\}$ and the integrand is

$$Z(\tau_1 \cdots \tau_k; \tau'_1 \cdots \tau'_k) = \left\langle T_\tau d(\tau'_1) d^\dagger(\tau_1) \cdots d(\tau'_k) d^\dagger(\tau_k) \right\rangle_0 \cdot \det M^{-1}(\{\tau_i\}, \{\tau_j\}) \quad (4.23)$$

with the hybridization matrix $(M^{-1})_{ij} = \Delta(\tau_i - \tau'_j)$.

4.2 Metropolis-Hastings Sampling

We use Markov-chain Monte Carlo to sample the hybridization expansion Eq. 4.22 (see, for example, Ref. [56] for an introduction). We use the Metropolis-Hastings algorithm to sample a distribution over the configuration space $\{i\}$ with probabilities P_i . The transition probabilities $T(i \rightarrow j)$ for stepping from configuration i to j is written

$$T(i \rightarrow j) = w(i \rightarrow j) A(i \rightarrow j) \quad (4.24)$$

where $w(i \rightarrow j)$ is the probability of proposing the move from i to j , and acceptance probability is

$$A(i \rightarrow j) = \min \left(1, \frac{P_j w(j \rightarrow i)}{P_i w(i \rightarrow j)} \right). \quad (4.25)$$

In the hybridization expansion, we are sampling over a semi-discrete space, consisting of the countably-infinite collection of $2k$ -dimensional integral phase spaces. A Monte Carlo configuration consists of the $2k$ times $\mathcal{D}_k = (\tau_1, \dots, \tau_k; \tau'_1 \dots \tau'_k)$ for the creation and annihilation operators.

The moves we use to step through the semi-discrete phase space $\mathcal{D} = \bigoplus_{k=0}^{\infty} \mathcal{D}_k$ consist of adding or removing two operators, one creation and one annihilation. When we add two operators, the proposal probability density is

$$w(\mathcal{D}_k \rightarrow \mathcal{D}_{k+1}) = \frac{1}{\beta^2}, \quad (4.26)$$

because we have an equal probability of inserting the creation operator at any point in the interval $[0, \beta]$, and likewise for the annihilation operator. When we remove two operators, we choose one of the $(k+1)$ creation operators for removal, and likewise for the annihilation operators, so we get

$$w(\mathcal{D}_{k+1} \rightarrow \mathcal{D}_k) = \frac{1}{(k+1)^2}. \quad (4.27)$$

The probability density for a given configuration is given by the integrands of the hybridization expansion Eq. 4.23, which we denote $Z(\mathcal{D}_k)$ in short. Thus the Metropolis-hastings acceptance probability for adding a pair of operators is

$$A(\mathcal{D}_k \rightarrow \mathcal{D}_{k+1}) = \min \left(1, \frac{\beta^2}{(k+1)^2} \frac{Z(\mathcal{D}_{k+1})}{Z(\mathcal{D}_k)} \right) \quad (4.28)$$

while the equivalent expression for removing a pair of operators is

$$A(\mathcal{D}_k \rightarrow \mathcal{D}_{k-1}) = \min \left(1, \frac{k^2}{\beta^2} \frac{Z(\mathcal{D}_{k-1})}{Z(\mathcal{D}_k)} \right) \quad (4.29)$$

4.3 General Models

The generalization of this formalism to models with arbitrary impurity Hilbert spaces and hybridization functions is straightforward. In the following derivation, we can

consider the impurity to be a general local object, which can be a multi-orbital atom or a cluster of atoms. The effective action for an impurity model where there are $\alpha = 1 \cdots N_b$ flavors of local electrons d_α^\dagger , with the bath electrons are already integrated out, is

$$S_{\text{eff}} = S_{\text{imp}} + \sum_{\alpha\alpha'} \int_0^\beta d\tau \int_0^\beta d\tau' d_\alpha^\dagger(\tau) \Delta_{\alpha\alpha'}(\tau - \tau') d_{\alpha'}(\tau'). \quad (4.30)$$

Performing the same steps as above, arrive at the hybridization expansion

$$Z_{\text{imp}} = Z_0 \sum_{k=0}^{\infty} \sum_{\alpha_1 \cdots \alpha_k} \sum_{\alpha'_1 \cdots \alpha'_k} \int_W d\tau_1 \cdots d\tau_k \int_W d\tau'_1 \cdots d\tau'_k Z(\mathcal{D}_k), \quad (4.31)$$

where the integrand is

$$Z(\mathcal{D}_k) = \left\langle T_\tau d_{\alpha'_1}(\tau'_1) d_{\alpha_1}^\dagger(\tau_1) \cdots d_{\alpha'_k}(\tau'_k) d_{\alpha_k}^\dagger(\tau_k) \right\rangle_0 \cdot \det M^{-1}(\mathcal{D}_k) \quad (4.32)$$

and the hybridization matrix is $(M^{-1})_{ij} = \Delta_{\alpha_i, \alpha'_j}(\tau_i - \tau'_j)$. The proposal probability for adding a pair of operators is modified. For each operator, in addition to choosing a time in the interval $[0, \beta]$, we choose one of the N_b baths, so we have

$$w(\mathcal{D}_k \rightarrow \mathcal{D}_{k+1}) = \frac{1}{(N_b \beta)^2}. \quad (4.33)$$

The proposal probability for removal is unmodified so the acceptance probabilities for Monte Carlo sampling just acquire extra factors of N_b^2 :

$$A(\mathcal{D}_k \rightarrow \mathcal{D}_{k+1}) = \min \left(1, \left(\frac{N_b \beta}{k+1} \right)^2 \frac{Z(\mathcal{D}_{k+1})}{Z(\mathcal{D}_k)} \right) \quad (4.34)$$

$$A(\mathcal{D}_k \rightarrow \mathcal{D}_{k-1}) = \min \left(1, \left(\frac{k}{N_b \beta} \right)^2 \frac{Z(\mathcal{D}_{k-1})}{Z(\mathcal{D}_k)} \right) \quad (4.35)$$

There is one additional simplification which occurs in the case when the hybridization matrix is block diagonal, where each block has dimension N_b^a and there are N_b blocks in total. In this block diagonal case, the hybridization terms in the impurity effective action separate

$$S_{\text{eff}} = S_{\text{imp}} + \sum_{a=1}^{N_b} S_{\text{hyb}}^a \quad (4.36)$$

$$S_{\text{hyb}}^a = \sum_{\alpha\alpha'} \int_0^\beta d\tau_a \int_0^\beta d\tau'_a d_{\alpha\alpha'}^\dagger(\tau_a) \Delta_{\alpha\alpha'}^a(\tau_a - \tau'_a) d_{\alpha\alpha'}(\tau'_a), \quad (4.37)$$

which means in the hybridization expansion, we generate a separate series in each hybridization term S_{hyb}^a , obtaining

$$Z_{\text{imp}} = Z_0 \sum_{k_1 \dots k_{N_b}}^{\infty} \prod_{a=1}^{N_b} \sum_{\alpha_{a1} \dots \alpha_{ak_a}} \sum_{\alpha'_{a1} \dots \alpha'_{ak_a}} \int_W d\tau_{a1} \dots d\tau_{ak_a} \int_W d\tau'_{a1} \dots d\tau'_{ak_a} Z(\mathcal{D}_{k_1}^1 \dots \mathcal{D}_{k_{N_b}}^{N_b}), \quad (4.38)$$

with the integrands

$$Z(\mathcal{D}_{k_1}^1 \dots \mathcal{D}_{k_{N_b}}^{N_b}) = \left\langle T_{\tau} \prod_{a=1}^{N_b} d_{a\alpha'_{a1}}(\tau'_{a1}) d_{a\alpha_{a1}}^{\dagger}(\tau_{a1}) \dots d_{a\alpha'_{ak_a}}(\tau'_{ak_a}) d_{a\alpha_{ak_a}}^{\dagger}(\tau_{ak_a}) \right\rangle_0 \\ \times \prod_{a=1}^{N_b} \det M^{-1}(\mathcal{D}_{k_a}^a) \quad (4.39)$$

and the hybridization matrices $(M^{-1}(\mathcal{D}_{k_a}^a))_{ij} = \Delta_{\alpha_{ai}, \alpha'_{aj}}^a(\tau_{ai} - \tau'_{aj})$. The hybridization determinant has factored into a product of individual determinants, one for each block. When adding two operators, we first choose one of the N_b blocks, then one of the N_b^a operators within the block. For the second operator, we can only choose one of the N_b^a operators within the same block since the integrand vanishes otherwise. Thus, the proposal probability density for adding a pair of operators is

$$w(\mathcal{D}_{k_a}^a \rightarrow \mathcal{D}_{k_a+1}^a) = \frac{1}{N_b} \frac{1}{(N_b^a \beta)^2}. \quad (4.40)$$

When we remove two operators, we again choose a one of the N_b blocks in which to operate, a removal probability of

$$w(\mathcal{D}_{k_a+1}^a \rightarrow \mathcal{D}_{k_a}^a) = \frac{1}{N_b} \frac{1}{(k_a + 1)^2}. \quad (4.41)$$

Assembling the factors, we arrive at the acceptance probabilities for the general model

$$A(\mathcal{D}_{k_a}^a \rightarrow \mathcal{D}_{k_a+1}^a) = \min \left(1, \left(\frac{N_b^a \beta}{k_a + 1} \right)^2 \frac{Z(\dots \mathcal{D}_{k_a+1}^a \dots)}{Z(\dots \mathcal{D}_{k_a}^a \dots)} \right) \quad (4.42)$$

$$A(\mathcal{D}_{k_a}^a \rightarrow \mathcal{D}_{k_a-1}^a) = \min \left(1, \left(\frac{k_a}{N_b^a \beta} \right)^2 \frac{Z(\dots \mathcal{D}_{k_a-1}^a \dots)}{Z(\dots \mathcal{D}_{k_a}^a \dots)} \right) \quad (4.43)$$

The most computationally expensive part of the Monte Carlo sampling is the computation of the impurity traces $\langle \dots \rangle_0$ in the acceptance probabilities, so it is imperative we find efficient ways to evaluate this trace. We note that the hybridization determinant ratios are not the bottleneck in general models, and can be computed cheaply via Sherman-Morrison formulas.

4.4 Evaluating the Impurity Trace

The impurity trace consists of a time-ordered correlation function. We compute the trace by first explicitly time-ordering the operators creation and annihilation operators, which we will denote F^i :

$$\langle T_\tau F_1(\tau_1) \cdots F_k(\tau_k) \rangle_0 = \text{sgn } \mathcal{P} \cdot \langle F_{\mathcal{P}(1)}(\tau_{\mathcal{P}(1)}) \cdots F_{\mathcal{P}(k)}(\tau_{\mathcal{P}(k)}) \rangle_0. \quad (4.44)$$

Here, \mathcal{P} denotes the permutation necessary for placing the operators in the time-ordered sequence. Since the impurity has a finite number of degrees of freedom, we express the operators in a complete basis of impurity states and take the trace. For example, if we use the impurity eigenstates $|n\rangle$ and eigenenergies E_n as the complete basis, we evaluate

$$\langle F_k(\tau_k) \cdots F_1(\tau_1) \rangle_0 = \sum_{n_1 \cdots n_k} \left[e^{-E_{n_k}(\beta - \tau_k)} F_{n_k, n_{k-1}}^k e^{-E_{n_{k-1}}(\tau_k - \tau_{k-1})} \cdots e^{-E_{n_1}(\tau_2 - \tau_1)} F_{n_1, n_k}^1 e^{-E_{n_k} \tau_1} \right] \quad (4.45)$$

where the matrix elements are denoted $F_{mn}^i \equiv \langle m | F^i | n \rangle$. In the atomic eigenstate basis, the creation and annihilation operators are nontrivial matrices, while the time-evolution operators are simple. Alternatively, we could have chosen the direct product basis of the single-particle operators F^i , in which the creation and annihilation operators are simple while the time-evolution operators are dense matrices. This approach to evaluating the impurity trace has been pursued via applications of the Krylov method [57, 58].

In our implementation, we use the atomic eigenbasis and take advantage of the symmetries in our system to construct “superstates”. If we have a set of operators (for example N , S and S_z) which commute with the Hamiltonian H , then we can decompose the atomic Hilbert space into block diagonal form, where each block is a group of states with definite quantum numbers in the commuting operators. The impurity operators F^i has nonzero matrix elements only between two of these blocks. Thus, it is convenient to group together the states within each block and call them a superstate $|a, m\rangle$, where a labels the superstate and m labels the individual states grouped to form the superstate. The action of an operator $F^i |a, m\rangle = |b, n\rangle$ takes us uniquely between two superstates a and b . Storing a single index array $F^i(a) = b$ for each operator allows us to figure

out which superstates are visited under a given sequence of operators in the impurity trace. The representation of the operators F^i has been reduced to small matrix blocks $(F_{ab}^i)_{mn} = \langle a, m | F^i | b, n \rangle$.

As implemented in our code, the evaluation of the impurity trace proceeds as follows: for each superstate $|a\rangle$, we use to index array $F^i(a)$ to step through the sequence of $2k$ operators describing the current Monte Carlo configuration, and find those “strings” of superstates $a_0 - a_1 - \dots - a_{2k}$ which survive the time evolution from 0 to β . For those strings which survive, we compute the trace of the matrix product of the impurity operators along with the time-evolution operators, and sum them together to obtain the total impurity trace.

4.5 Fast Rejection via Lazy Evaluation

The vast majority of proposed moves are rejected. For example, in 5-orbital systems with realistic atomic interactions, the regime relevant for $3d$ elements, less than 5% of moves are accepted at temperatures near 100 K. Often, the acceptance rate is below 1%. These statistics suggest computational gains could be made if we quickly filter out moves with low acceptance probabilities. As described in Ref. [28], a scheme based on storing a string of matrix products from the left and right on the time interval $[0, \beta]$ already allows for efficient filtering of proposed moves. In this section, we present an additional fast rejection scheme based on bracketing the randomly chosen acceptance threshold.

The idea is to transpose the order of the acceptance probability computation with the coin-flipping in the Monte Carlo sampling. In the conventional sampling procedure, we compute the acceptance probability $A = A(i \rightarrow j)$ for a given proposed move, and actually accept the move if $A > P$, where P is a randomly chosen number in the interval $[0, 1]$. In our fast rejection scheme, we first flip the coin to obtain P , then we lazily evaluate rough bounds $A_{\min} < A < A_{\max}$ for the acceptance probability. If $A_{\max} < P$, we reject the move. If $A_{\min} \geq P$, we accept the move. If we cannot decide, we refine the bounds on A with the minimal of effort, and perform the comparison again. This

cycle is repeated until we can make a decision on whether to accept the move.

We compute our bounds by evaluating as few superstate matrix product strings as possible. Given a matrix product representing one string of surviving superstates

$$T_a = \text{tr } U_{2k} F_{2k} U_{2k-1} F_{2k-1} \cdots U_1 F_1 U_0 \quad (4.46)$$

where U_i are the time-evolution operators, we use the fact that $\|F_i\| < f_i$ are bounded to construct an approximation for the partial trace

$$\tilde{T}_a = \text{tr } U_{2k} f_{2k} U_{2k-1} f_{2k-1} \cdots U_1 f_1 U_0 \quad (4.47)$$

which is easy to compute since it only involves summing the sequence of exponents $E_i(\tau_i - \tau_{i-1})$ arising from the time-evolution operators. This approximation bounds the exact partial trace as $|T_a| < \tilde{T}_a$. The full impurity trace T is then bounded by

$$|T| = \left| \sum_a T_a \right| < \sum_a |T_a|, \quad (4.48)$$

which allows us to compute rough upper A_{\max} and lower A_{\min} bounds on our acceptance probability A . Often, this approximation is sufficient to reject the move.

If we cannot reject or accept the move outright, we proceed to compute the exact partial trace T_a for the superstate string with the largest approximation \tilde{T}_a . This allows us to refine our bounds on the total trace

$$|T - T_a| < \sum_{b \neq a} |T_b|, \quad (4.49)$$

and tighten our upper and lower bounds on the acceptance probability A . We iterate until we are able to definitively accept or reject the proposed move. This algorithm provides up to a five-fold factor of speed-up with respect to the original code utilizing the left-right matrix products.

Chapter 5

Reciprocal Distribution Sampling

Algorithms for direct evaluation of the partition function are useful since they allow access to the free energy, and thus, thermodynamic quantities. In this chapter, we describe an algorithm for evaluation of the reciprocal of the partition function in the context of CTQMC for $SU(N)$ Anderson impurity models. The result allows for the computation of the entropy via $S = \beta(E - F)$, and for generalizations to the lattice via DMFT in the future.

5.1 Sampling the Reciprocal Distribution and Phase Space Volume

We want to sample the impurity partition function within the hybridization expansion continuous-time quantum Monte Carlo solver. The general approach we will take is to sample the reciprocal distribution, a concept which is applicable in any Monte Carlo scheme where we have access to the phase space volume. For example, if $f(x)$ is our distribution function, the sampling of normal observables $A(x)$ is equivalent to evaluating

$$\langle A \rangle = \frac{\int dx f(x) A(x)}{\int dx f(x)}. \quad (5.1)$$

If we take our observable to be the reciprocal distribution $A = 1/f$, then we sample

$$\left\langle \frac{1}{f} \right\rangle = \frac{\int dx}{\int dx f(x)} \equiv \frac{V}{Z}. \quad (5.2)$$

Often, there are regions where f vanishes, so in fact the phase space volume is

$$V = \int dx \theta(f(x) \neq 0), \quad (5.3)$$

that is, we restrict the integral regions of finite f since the importance sampling ignores regions of zero probability. Reciprocal distribution sampling gives us direct access to the unnormalized distribution, provided we know the phase space volume V . In most simulations of physical systems, the unnormalized distribution is the partition function, a quantity of key interest.

As an example, consider sampling the reciprocal Boltzman distribution at a fixed energy E :

$$\left\langle e^{E(X)/T} \delta(E(X) - E) \right\rangle = \int dX \frac{e^{-E(X)/T}}{Z} e^{E(X)/T} \delta(E(X) - E) \quad (5.4)$$

$$= \frac{1}{Z} \int dX \delta(E(X) - E) \quad (5.5)$$

$$\equiv \frac{g(E)}{Z}. \quad (5.6)$$

Since we sample at fixed energy, the phase space volume V is the familiar density of states. For CTQMC, we sample at fixed perturbation order k , so V will be the number of diagrams at that perturbation order.

5.2 Spinless Fermions

The expansion of the partition function in CTQMC for spinless fermions is

$$Z = Z_0 \sum_{k=0}^{\infty} \int_0^{\beta} d\tau_1 \int_{\tau_1}^{\beta} d\tau_2 \cdots \int_{\tau_{k-1}}^{\beta} d\tau_k \int_0^{\beta} d\tau'_1 \int_{\tau'_1}^{\beta} d\tau'_2 \cdots \int_{\tau'_{k-1}}^{\beta} d\tau'_k \times Z(\tau_1 \cdots \tau_k; \tau'_1 \cdots \tau'_k), \quad (5.7)$$

where we write Z_0 for the atomic partition function and the integrand is

$$Z(\tau_1 \cdots \tau_k; \tau'_1 \cdots \tau'_k) = \left\langle T_{\tau} \psi(\tau'_1) \psi^{\dagger}(\tau_1) \cdots \psi(\tau'_k) \psi^{\dagger}(\tau_k) \right\rangle_0 \det M^{-1} \equiv Z(\mathcal{D}_k), \quad (5.8)$$

and the $k \times k$ matrix $(M^{-1})_{ij} = \Delta(\tau_i - \tau'_j)$.

We sample the reciprocal distribution at fixed perturbation order k ,

$$\left\langle \frac{\delta_{k,k'}}{Z(\mathcal{D}_{k'})} \right\rangle = \frac{Z_0}{Z} \int_W d\tau_1 \cdots d\tau_k \int_W d\tau'_1 \cdots d\tau'_k \theta(Z(\mathcal{D}_k) \neq 0) \equiv \frac{Z_0}{Z} V_k, \quad (5.9)$$

where the integration region W is shorthand for the wedge $0 < \tau_1 < \cdots < \tau_k < \beta$. This gives us the inverse partition function, up to factors of the atomic partition function Z_0 (which is easily computed) and the diagram density V_k .

Let us compute V_k . For $k = 0$, the volume is just unity. For $k \geq 1$, we have

$$V_k = \int_W d\tau_1 \cdots d\tau_k \int_W d\tau'_1 \cdots d\tau'_k \theta(Z(\mathcal{D}_k) \neq 0). \quad (5.10)$$

The distribution $Z(\mathcal{D}_k)$ is composed of two parts, an atomic trace and a hybridization determinant. The determinant never vanishes if $\Delta(\tau)$ is always nonzero, a reasonable assumption for physical systems. However, if we assume the atomic action conserves particle number (no terms like ψ^\dagger or ψ in isolation), the trace can vanish due to Fermi statistics. There are only two arrangements of the $2k$ creation and annihilation operators which survive: $\psi\psi^\dagger\psi\psi^\dagger\cdots$ and $\psi^\dagger\psi\psi^\dagger\psi\cdots$. The volume of a particular arrangement of the $2k$ operators is $\beta^{2k}/(2k)!$ so we arrive at

$$V_k = \begin{cases} 1 & k = 0, \\ 2 \cdot \frac{\beta^{2k}}{(2k)!} & k \geq 1. \end{cases} \quad (5.11)$$

In practice, we sample $1/V_k Z_0 Z(\mathcal{D}_k)$ for each perturbation order k so that we obtain exactly $1/Z$ at each order. This quantity can be easily computed from the acceptance probabilities. Recall the probability to add two operators is

$$p(\mathcal{D}_k \rightarrow \mathcal{D}_{k+1}) = \frac{\beta^2}{(k+1)^2} \frac{Z(\mathcal{D}_{k+1})}{Z(\mathcal{D}_k)}. \quad (5.12)$$

Rearranging, we get the new $V_{k+1} Z_0 Z(\mathcal{D}_{k+1})$ in terms of $V_k Z_0 Z(\mathcal{D}_k)$ as follows:

$$V_{k+1} Z_0 Z(\mathcal{D}_{k+1}) = V_k Z_0 Z(\mathcal{D}_k) \cdot p(\mathcal{D}_k \rightarrow \mathcal{D}_{k+1}) \cdot \frac{V_{k+1}}{V_k} \frac{(k+1)^2}{\beta^2}. \quad (5.13)$$

The ratio of volumes is

$$\frac{V_{k+1}}{V_k} = \begin{cases} \beta^2 & k = 0, \\ \frac{\beta^2}{(2k+2)(2k+1)} & k \geq 1, \end{cases} \quad (5.14)$$

which allows us to update our observable when adding two operators as follows:

$$V_{k+1} Z_0 Z(\mathcal{D}_{k+1}) = V_k Z_0 Z(\mathcal{D}_k) \cdot p(\mathcal{D}_k \rightarrow \mathcal{D}_{k+1}) \cdot \begin{cases} 1 & k = 0, \\ \frac{(k+1)^2}{(2k+2)(2k+1)} & k \geq 1. \end{cases} \quad (5.15)$$

A similar calculation for the removal of two operators gives

$$V_{k-1} Z_0 Z(\mathcal{D}_{k-1}) = V_k Z_0 Z(\mathcal{D}_k) \cdot p(\mathcal{D}_k \rightarrow \mathcal{D}_{k-1}) \cdot \begin{cases} 1 & k = 1, \\ \frac{(2k)(2k-1)}{k^2} & k \geq 2. \end{cases} \quad (5.16)$$

Thus, as we importance sample, we simply store the list of observables $1/V_k V_0 Z(\mathcal{D}_k)$. The CTQMC histogram is strongly peaked around a particular perturbation order $\langle k \rangle$, so we use only the sampled values near $\langle k \rangle$ to calculate $1/Z$ to better precision.

5.3 One-Band Model

Including spin leads to some minor complications but the idea is the same. For this derivation, we assume the hybridization conserves spin, that is

$$S = S_0 + \sum_{\sigma} \int_0^{\beta} d\tau \int_0^{\beta} d\tau' \psi_{\sigma}^{\dagger}(\tau) \Delta_{\sigma}(\tau - \tau') \psi_{\sigma}(\tau') \equiv \sum_{\sigma} S_{\text{hyb}}^{\sigma}. \quad (5.17)$$

The expansion of the partition function now contains two sums,

$$Z = Z_0 \sum_{k_{\uparrow} k_{\downarrow}} \frac{1}{k_{\uparrow}!} \frac{1}{k_{\downarrow}!} \left\langle T_{\tau} (-S_{\text{hyb}}^{\uparrow})^{k_{\uparrow}} (-S_{\text{hyb}}^{\downarrow})^{k_{\downarrow}} \right\rangle_0 \quad (5.18)$$

$$= Z_0 \sum_{k_{\uparrow} k_{\downarrow}} \int_W \prod_i^{k_{\uparrow}} d\tau_{\uparrow i} \int_W \prod_i^{k_{\uparrow}} d\tau'_{\uparrow i} \int_W \prod_i^{k_{\downarrow}} d\tau_{\downarrow i} \int_W \prod_i^{k_{\downarrow}} d\tau'_{\downarrow i} \quad (5.19)$$

$$\times Z(\tau_{\uparrow 1} \cdots \tau_{\uparrow k}; \tau'_{\uparrow 1} \cdots \tau'_{\uparrow k}; \tau_{\downarrow 1} \cdots \tau_{\downarrow k}; \tau'_{\downarrow 1} \cdots \tau'_{\downarrow k}). \quad (5.20)$$

Ultimately we want to sample the reciprocal distribution at a given total perturbation order $k = k_{\uparrow} + k_{\downarrow}$, but as an intermediate step, we sample at fixed k_{\uparrow} and k_{\downarrow} :

$$\begin{aligned} \left\langle \frac{\delta_{k_{\uparrow}, k'_{\uparrow}} \delta_{k_{\downarrow}, k'_{\downarrow}}}{Z(\mathcal{D}_{k'_{\uparrow} k'_{\downarrow}})} \right\rangle &= \frac{Z_0}{Z} \int_W \prod_i^{k_{\uparrow}} d\tau_{\uparrow i} \int_W \prod_i^{k_{\uparrow}} d\tau'_{\uparrow i} \int_W \prod_i^{k_{\downarrow}} d\tau_{\downarrow i} \int_W \prod_i^{k_{\downarrow}} d\tau'_{\downarrow i} \theta(Z(\mathcal{D}_{k_{\uparrow} k_{\downarrow}}) \neq 0) \\ &\equiv \frac{Z_0}{Z} V_{k_{\uparrow} k_{\downarrow}}. \end{aligned}$$

It turns out the joint volume factors as $V_{k_{\uparrow} k_{\downarrow}} = V_{k_{\uparrow}} V_{k_{\downarrow}}$. To derive this, first note that the hybridization determinant again never vanishes, so Fermi statistics controls when the distribution vanishes. The volume of a particular arrangement of all $2(k_{\uparrow} + k_{\downarrow})$ operators is

$$\text{single wedge volume} = \frac{\beta^{2k_{\uparrow} + 2k_{\downarrow}}}{(2k_{\uparrow} + 2k_{\downarrow})!}. \quad (5.21)$$

The number of ways we can interleave the $2k_{\uparrow}$ up-spin operators with the $2k_{\downarrow}$ down-spin operators is $\binom{2k_{\uparrow} + 2k_{\downarrow}}{2k_{\uparrow}}$. Let us assume the atomic interactions conserve spin and particle number. Amongst the up-spins, we must arrange the $\psi_{\uparrow}^{\dagger}$ and ψ_{\uparrow} in alternating order to

have a non-vanishing trace. There are two ways to do this. The situation is identical with the down-spin operators. The phase space is

$$V_{k_\uparrow k_\downarrow} = 2^2 \cdot \frac{(2k_\uparrow + 2k_\downarrow)!}{(2k_\uparrow)!(2k_\downarrow)!} \cdot \frac{\beta^{2k_\uparrow + 2k_\downarrow}}{(2k_\uparrow + 2k_\downarrow)!} = \prod_\sigma \frac{2\beta^{2k_\sigma}}{(2k_\sigma)!} = \prod_\sigma V_{k_\sigma}. \quad (5.22)$$

Actually, this derivation only holds if both $k_\uparrow > 0$ and $k_\downarrow > 0$. Taking into account the special cases, we again find that $V_{k_\uparrow k_\downarrow} = V_{k_\uparrow} V_{k_\downarrow}$, with V_k defined as in Eq. 5.11.

Now we compute the volume when we sample all diagrams contributing to a fixed total perturbation order:

$$\left\langle \frac{\delta_{k_\uparrow + k_\downarrow = k}}{Z(\mathcal{D}_{k_\uparrow k_\downarrow})} \right\rangle = \frac{Z_0}{Z} \sum_{k_\uparrow k_\downarrow} V_{k_\uparrow k_\downarrow} \delta_{k_\uparrow + k_\downarrow = k} = \frac{Z_0}{Z} \sum_{k_\uparrow=0}^k V_{k_\uparrow} V_{k-k_\uparrow} \equiv \frac{Z_0}{Z} V_k. \quad (5.23)$$

Evaluating the summation gives us the 2-bath volume:

$$V_k = \begin{cases} 1 & k = 0, \\ 2(2^{2k} - 2) \frac{\beta^{2k}}{(2k)!} & k \geq 1. \end{cases} \quad (5.24)$$

Again we sample the distribution multiplied by the volume $V_k Z_0 Z(\mathcal{D}_{k_\uparrow k_\downarrow})$, where the constraint $k_\uparrow + k_\downarrow = k$ is understood. For the addition of two up-spin operators, the update formula is

$$\begin{aligned} V_{k+1} Z_0 Z(\mathcal{D}_{k_\uparrow+1, k_\downarrow}) &= V_k Z_0 Z(\mathcal{D}_{k_\uparrow k_\downarrow}) \\ &\times p(\mathcal{D}_{k_\uparrow k_\downarrow} \rightarrow \mathcal{D}_{k_\uparrow+1, k_\downarrow}) \cdot \begin{cases} 2 & k = 0, \\ \frac{2^{2k+2} - 2}{2^{2k} - 2} \frac{(k_\uparrow + 1)^2}{(2k + 2)(2k + 1)} & k \geq 1. \end{cases} \end{aligned} \quad (5.25)$$

Swapping $k_\uparrow \leftrightarrow k_\downarrow$ gives the formula for the addition of two down-spin operators. A similar calculation for the removal of two operators gives

$$\begin{aligned} V_{k-1} Z_0 Z(\mathcal{D}_{k_\uparrow-1, k_\downarrow}) &= V_k Z_0 Z(\mathcal{D}_{k_\uparrow k_\downarrow}) \\ &\times p(\mathcal{D}_{k_\uparrow k_\downarrow} \rightarrow \mathcal{D}_{k_\uparrow-1, k_\downarrow}) \cdot \begin{cases} \frac{1}{2} & k = 1, \\ \frac{2^{2k-2} - 2}{2^{2k} - 2} \frac{(2k)(2k-1)}{k_\uparrow^2} & k \geq 2. \end{cases} \end{aligned} \quad (5.26)$$

5.4 Arbitrary Number of Diagonal Baths

For N baths, where we assume each bath is one-dimensional and there are no inter-bath hoppings, we find that the phase space volume is the product

$$V_k = \sum_{k_1 \dots k_N} V_{k_1} \dots V_{k_N} \delta_{k_1 + \dots + k_N = k}. \quad (5.27)$$

There are many terms in this sum, due to the special case for $k = 0$ in the formula for V_{k_α} . Writing the single bath volume as

$$V_k^{(1)} = \frac{2\beta^{2k}}{(2k)!} - \delta_{k=0} \equiv \bar{V}_k - \delta_{k=0}, \quad (5.28)$$

and inserting this into the general volume expression gives

$$V_k = \sum_{k_1 \dots k_N} \bar{V}_{k_1} \dots \bar{V}_{k_N} \left[1 - \sum_{\alpha} \frac{\delta_{k_\alpha=0}}{\bar{V}_{k_\alpha}} + \sum_{\{\alpha_1 \alpha_2\}} \frac{\delta_{k_{\alpha_1}=0}}{\bar{V}_{k_{\alpha_1}}} \frac{\delta_{k_{\alpha_2}=0}}{\bar{V}_{k_{\alpha_2}}} + \dots \right. \\ \left. \pm \sum_{\{\alpha_1 \dots \alpha_N\}} \frac{\delta_{k_{\alpha_1}=0}}{\bar{V}_{k_{\alpha_1}}} \dots \frac{\delta_{k_{\alpha_N}=0}}{\bar{V}_{k_{\alpha_N}}} \right] \delta_{k_1 + \dots + k_N = k}, \quad (5.29)$$

where, for example, by $\sum_{\{\alpha_1 \alpha_2\}}$ we mean the sum over all unordered pairs (α_1, α_2) where $\alpha_1 \neq \alpha_2$. Since $\bar{V}_{k=0} = 2$, we simplify to obtain

$$V_k = \frac{\beta^{2k}}{(2k)!} \sum_{\alpha=0}^N (-)^\alpha \binom{N}{\alpha} \cdot 2^{N-\alpha} \sum_{k_1 \dots k_{N-\alpha}} \frac{(2k)!}{(2k_1)! \dots (2k_{N-\alpha})!} \cdot \delta_{k_{\alpha_1} + \dots + k_{\alpha_{N-\alpha}} = k} \quad (5.30)$$

$$= \frac{\beta^{2k}}{(2k)!} \sum_{\alpha=0}^N (-)^\alpha \binom{N}{\alpha} \sum_{\eta=0}^{N-\alpha} \binom{N-\alpha}{\eta} (N-\alpha-2\eta)^{2k}. \quad (5.31)$$

For the special case $k = 0$, the volume $V_k = 1$.

For the addition of two operators in bath α , we need the ratio

$$\frac{V_{k+1}}{V_k} \frac{(k_\alpha + 1)^2}{\beta^2} = \frac{N^2(k_\alpha + 1)^2}{(2k+2)(2k+1)} \left(\frac{g_{N,k+1}}{g_{N,k} N^2} \right). \quad (5.32)$$

Similarly, for the removal of two operators in bath α , we need the ratio

$$\frac{V_{k-1}}{V_k} \frac{\beta^2}{k_\alpha^2} = \frac{(2k)(2k-1)}{N^2 k_\alpha^2} \left(\frac{g_{N,k-1} N^2}{g_{N,k}} \right). \quad (5.33)$$

The expressions in parenthesis are close to unity, except at small perturbation order k .

We tabulate for small N the expressions for g_k in Table. 5.1.

N	$g_{N,k}$
1	1
2	$2^{2k} - 2$
3	$3^{2k} - 3 \cdot 2^{2k} + 6$
4	$4^{2k} - 4 \cdot 3^{2k} + 10 \cdot 2^{2k} - 16$
5	$5^{2k} - 5 \cdot 4^{2k} + 15 \cdot 3^{2k} - 30 \cdot 2^{2k} + 45$
6	$6^{2k} - 6 \cdot 5^{2k} + 21 \cdot 4^{2k} - 50 \cdot 3^{2k} + 90 \cdot 2^{2k} - 126$

Table 5.1: Table of polynomials g_k for Eq. 5.33.

5.5 Thermodynamic Quantities

Sampling the partition function Z allows us to compute the free energy $F = -T \log Z$. If additionally we had access to the energy E , we could compute the entropy $S = \beta(E - F) = \beta E + \log Z$. Usually, computation of the entropy requires an integration over temperature, as described in Appendix F, while this approach is single-point in temperature. We describe the details of these thermodynamic quantities in the following section.

In the Anderson impurity model, since the conduction bath is noninteracting, we can factor the partition function into the form

$$Z = Z_{\text{bath}} \cdot Z_{\text{imp}} \quad (5.34)$$

$$Z_{\text{bath}} = \prod_{nk\sigma} \beta(-i\omega_n + \epsilon_k) \equiv \prod_{nk\sigma} \beta(-g_k^{-1}(i\omega_n)) \quad (5.35)$$

$$Z_{\text{imp}} = \int \mathcal{D}[\psi^\dagger \psi] e^{-S_{\text{eff}}} \quad (5.36)$$

where S_{eff} is defined as in Eq. 5.17. With this convention, the free energy decomposes into two terms $F = F_{\text{imp}} + F_{\text{bath}}$. In CTQMC, we only compute the impurity contribution since we drop Z_{bath} from our formulas.

For formal manipulation, it is useful to work in terms of the effective-action formalism. The Baym-Kadanoff functional for the free energy at the saddle point is

$$F = \text{tr} \log G - \text{tr} \Sigma G + \Phi[G]. \quad (5.37)$$

Here, the Green's function is

$$G = \begin{pmatrix} i\omega_n - E_{\text{imp}} - \Sigma & V \\ V & (i\omega_n - \epsilon_k)\delta_{kk'} \end{pmatrix}^{-1} = \begin{pmatrix} G_{dd} & G_{dk'} \\ G_{kd} & G_{kk'} \end{pmatrix} \quad (5.38)$$

and the trace $\text{tr} \equiv \beta^{-1} \sum_{nk\sigma}$ has units of energy. The Luttinger-Ward functional, which collects all the skeleton diagrams, is denoted $\Phi[G]$. The various propagators are defined as follows:

$$G_{dd} = \frac{1}{i\omega_n - E_{\text{imp}} - \Delta - \Sigma} \quad (5.39)$$

$$G_{kd} = G_{dk} = g_k V G_{dd} \quad (5.40)$$

$$G_{kk'} = g_k \delta_{kk'} + g_k V G_{dd} V g_{k'} \quad (5.41)$$

and the quantities relating to the bare conduction bath are

$$g_k = \frac{1}{i\omega_n - \epsilon_k} \quad \Delta = V^2 \sum_k g_k \quad (5.42)$$

Using these equations, we can separate the formal expression of the free energy into the impurity and bath contributions. Applying the formula for determinants of block matrices to the first term $\text{tr} \log G$,

$$\det \begin{pmatrix} A & B \\ C & D \end{pmatrix} = \det(A) \cdot \det(D - C A^{-1} B), \quad (5.43)$$

we can separate the bath contribution in the first term to obtain

$$F_{\text{bath}} = \text{tr} \log g \quad (5.44)$$

$$F_{\text{imp}} = \text{tr} \log G_{dd} - \text{tr} \Sigma G_{dd} + \Phi[G_{dd}] \quad (5.45)$$

The interaction terms only depend on the impurity Green's function.

In this same framework, the energy is

$$E = \text{tr} H_0 G + \frac{1}{2} \text{tr} \Sigma G, \quad (5.46)$$

where H_0 denotes the single-particle part of the hamiltonian, namely

$$H_0 = \begin{pmatrix} E_{\text{imp}} & V \\ V & \epsilon_k \end{pmatrix}. \quad (5.47)$$

The second term in the energy is $\text{tr} \Sigma G_{dd}$, while the first can be decomposed into the

impurity and bath contributions:

$$\text{tr } H_0 G = \text{tr} \begin{pmatrix} E_{\text{imp}} G_{dd} + V \sum_k G_{kd} & \cdots \\ \cdots & V G_{dk'} + \epsilon_k G_{kk'} \end{pmatrix} \quad (5.48)$$

$$= 2 \text{tr } \Delta G_{dd} + \text{tr} \sum_k \epsilon_k G_{kk}. \quad (5.49)$$

We can separate the bath contribution out of the second term:

$$\text{tr} \sum_k \epsilon_k G_{kk} = \text{tr} \sum_k \epsilon_k g_k + \text{tr} G_{dd} V^2 \sum_k \epsilon_k g_k^2 \quad (5.50)$$

$$= \text{tr} \epsilon g - \text{tr} \Delta G_{dd} + \text{tr} G_{dd} i\omega_n V^2 \sum_k g_k^2 \quad (5.51)$$

We want to perform the momentum summation in the second term to rewrite it in terms of the hybridization Δ . In order to do so, we eliminate the double pole by using

$$g_k^2(i\omega_n) = -\frac{\partial}{\partial(i\omega_n)} g_k(i\omega_n) \quad (5.52)$$

to finally obtain

$$E_{\text{bath}} = \text{tr} \epsilon g \quad (5.53)$$

$$E_{\text{imp}} = \text{tr} \Delta G_{dd} - \text{tr} \frac{\partial \Delta(i\omega_n)}{\partial \log(i\omega_n)} G_{dd} + \frac{1}{2} \text{tr} \Sigma G_{dd}. \quad (5.54)$$

In this equation, E_{imp} is the thermodynamic energy contribution of the impurity, and not the impurity level denoted by the same symbol in Eq. 5.47. The first kinetic term $E_{\text{kin}} = \text{tr} \Delta G_{dd}$ and the last potential term $\text{tr} \Sigma G_{dd}/2$ are easy to compute with high precision via the CTQMC sampling [28]. The logarithmic kinetic correction due to frequency dependence of the hybridization function is evaluated by subtracting out the analytic tails at large $i\omega_n$.

We show in Fig. 5.1 the various energetic contributions for the single-orbital Anderson impurity model at half-filling in the Bethe lattice. The Bethe lattice has a semi-circular density of states, giving the hybridization function

$$\Delta(z) = \frac{1}{2}(z - \sqrt{z^2 - D^2}), \quad (5.55)$$

where D is the half-bandwidth, and from which we can evaluate the logarithmic term analytically. We find that all three terms are of the same order of magnitude at low

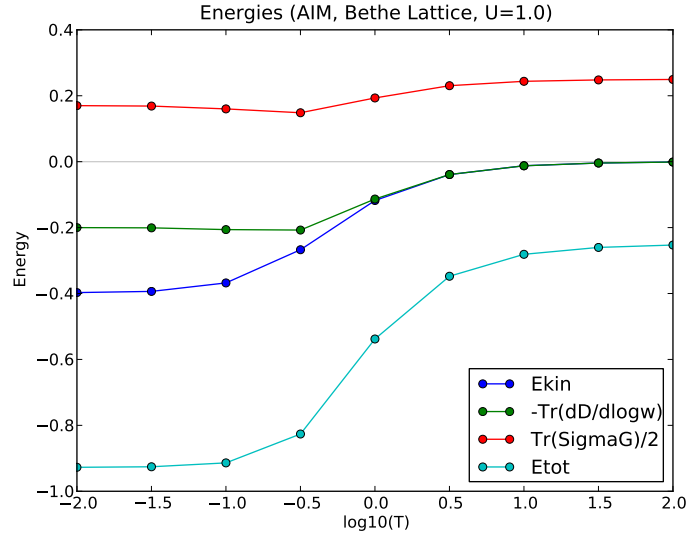


Figure 5.1: Contributions of each of the three terms in Eq. 5.54 to the total energy for the one-orbital Anderson impurity model at half-filling on the Bethe lattice. Energies in units of the half-bandwidth D .

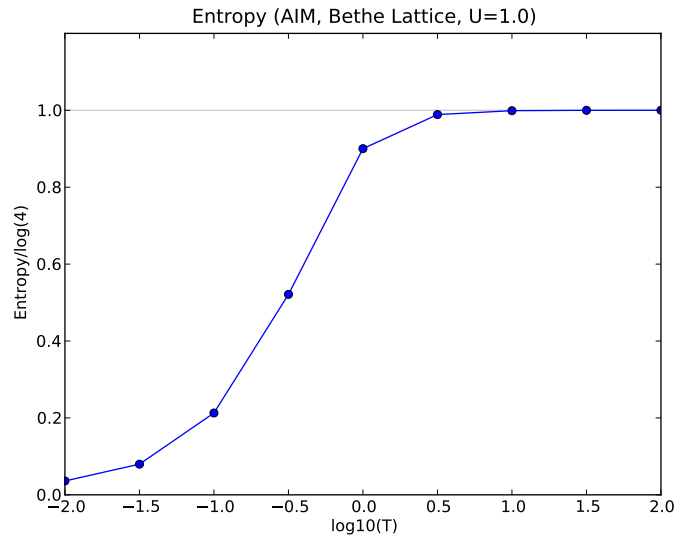


Figure 5.2: Entropy for the same impurity model as Fig. 5.1 computing using reciprocal distribution sampling.

temperatures. In Fig. 5.2 we plot the entropy of the same model computed by the reciprocal distribution sampling algorithm.

The advantage of sampling the reciprocal distribution is its high accuracy and low computational cost. There is essentially no additional overhead in sampling the reciprocal distribution at each perturbation order. Future directions include extending the derivation to models with general atomic interactions, for example, to cluster models or multi-orbital systems where the atomic interactions do not conserve orbital number.

Chapter 6

Valence Fluctuations and Quasiparticle Multiplets in Pu Chalcogenides and Pnictides

The application of our code to plutonium binary alloys was one of the first tests of our DFT+DMFT implementation in the full-potential basis. Plutonium is an element with enormous importance to our nation's energy and weapons needs [59]. Plutonium is mostly known for its nuclear properties, but its structural and electronic properties happen to also be incredibly complex, exhibiting six distinct phases as a function of temperature (Fig. 6.1). Compounds containing plutonium are key test cases for two reasons. First, its partially-filled $5f$ -shell is extremely small compared to the lattice spacing, causing the element to retain much of its atomic character even when embedded in a solid. This provides an ideal system to test the local approximation lying at the heart of DMFT. Second, plutonium lies at the boundary of the localization-delocalization transition in the actinide series (Fig. 6.2). The early actinides exhibit itinerant electronic behavior, while the late actinides are localized. The active $5f$ -electrons in plutonium can be driven to be metallic or insulating as a function of external parameters like pressure and temperature, or as a function of chemistry via alloying.

In this chapter, published as Ref. [61], we compare the effect of alloying plutonium with an element from the nitrogen column (pnictide) versus the oxygen column (chalcogenide). Experimentally, it is known that these two families of compounds exhibit contrasting electronic behavior, which we seek to understand using our electronic structure methods. In this work, the spectra of these compounds are computed with

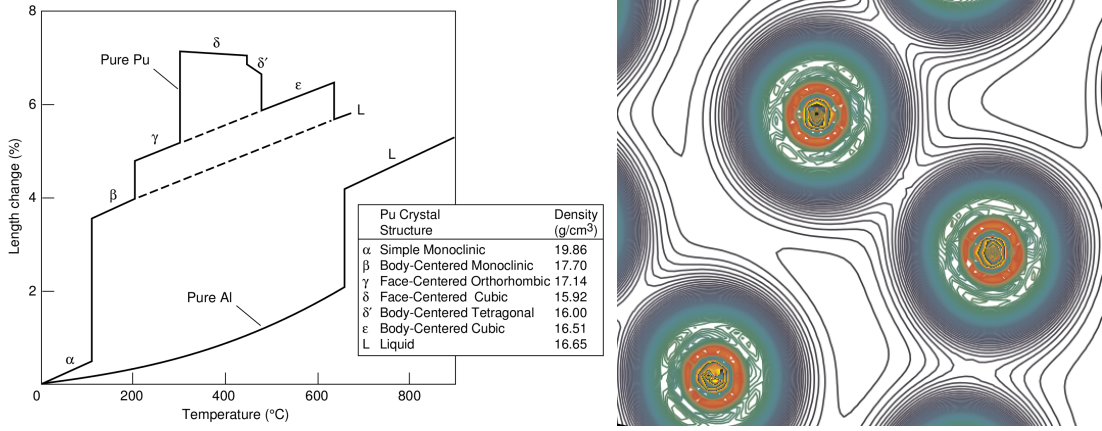


Figure 6.1: The rich electronic and structural behavior of plutonium [60]. (left) As a function of temperature, Pu exhibits six distinct structural phases with differing electronic properties. The comparatively sedate behavior of aluminum is shown for comparison. (right) The charge density of α -plutonium, showing the extreme spatial localization of the $5f$ -electrons as compared to the lattice spacing.

DFT+DMFT and interpreted with the aid of valence histograms and slave-boson calculations. We find the chalcogenides are mixed-valent ($n_f = 5.2$) materials with a strongly T -dependent low-energy density of states and a triplet of quasiparticle peaks below the Fermi level. Furthermore, we predict a doublet of reflected peaks above the Fermi level. In the pnictides, the raising of f^6 states relative to f^5 suppresses valence fluctuations, resulting in integral-valent ($n_f = 5.0$) local moment metals.

6.1 Introduction

The stark contrast in behavior between the plutonium monochalcogenides and monpnictides is a longstanding issue in strongly-correlated physics (Fig. 6.3). The pnictides (PuSb, PuAs, PuP) are comparatively simple metals [62] with embedded f -moments arising from trivalent Pu ions which order in the range $T_c = 85$ to 126 K [63]. In contrast, the chalcogenides (PuTe, PuSe, PuS) exhibit seemingly contradictory behavior: they have a large room temperature specific heat [64], yet the resistivity indicates a small gap [65, 66, 67]. Also, their lattice constant rules out the full-shell divalent Pu state, yet the susceptibility shows no evidence of Curie-Weiss behavior [63]. Furthermore, photoemission observes a triplet of peaks (the “photoemission triplet”) near the Fermi level [68, 69, 70, 71] whose origin is still hotly debated [68, 69].

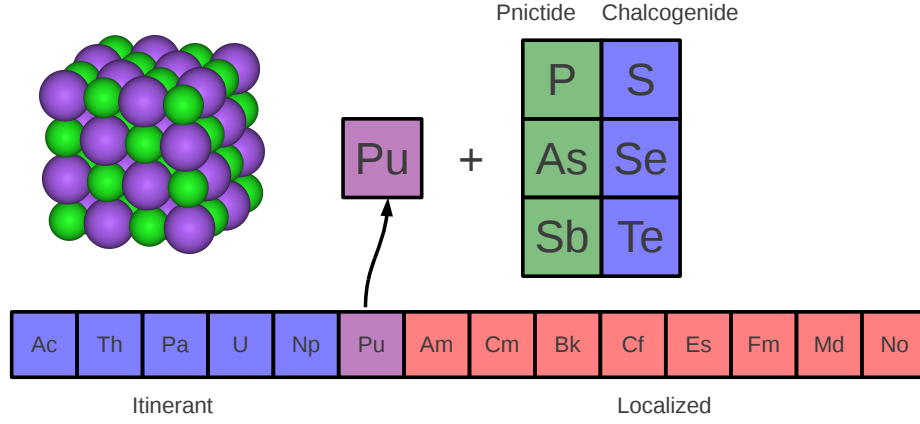


Figure 6.2: In the actinide series, plutonium lies at the border between itinerant and localized electronic behavior. Alloying plutonium with an element from the pnictide or chalcogenide stabilizes tips the scale to favor one behavior over the other. All binary alloys considered in this work form rock salt crystal structures.

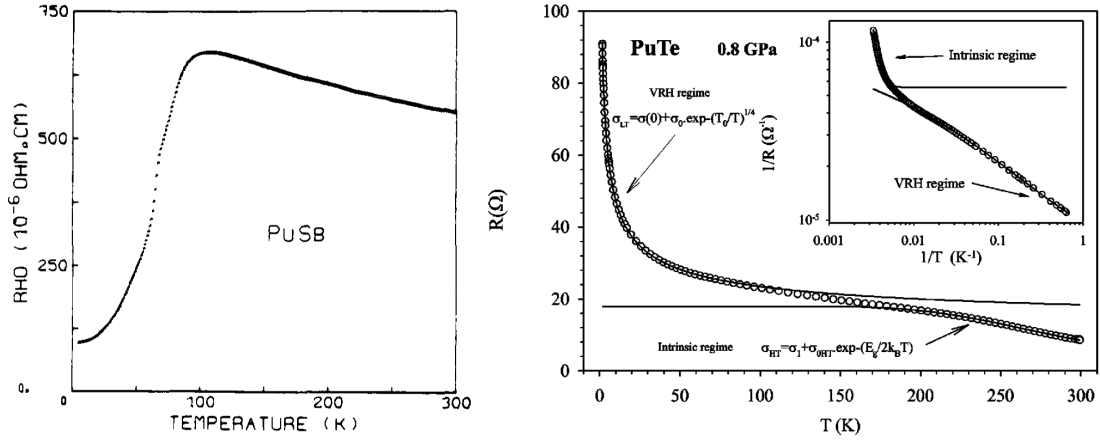


Figure 6.3: Observed electrical resistivities of representative plutonium alloys as a function of temperature. (left) The pnictide PuSb exhibits metallic behavior: the resistivity decreases as the temperature is lowered in the relevant range of 0-100 K [62]. (right) The chalcogenide PuTe is insulating [67]. The strong rise in resistivity with the decrease in temperature indicates the presence of a gap.

The contrast between the Pu chalcogenides and pnictides exemplifies the view that the Pu $5f$ electrons sit at the edge of a localization-delocalization transition, where small changes in their electronic environment can drive a transition to itinerancy or localization, thus posing a major challenge to electronic structure methods. Theoretical studies of the chalcogenides within LDA [72, 73] predict a metal and do not account for the photoemission triplet. Methods treating correlations beyond LDA have improved the situation, but cannot fully integrate the available experimental data within a single theory. Non-charge-self-consistent LDA+DMFT with FLEX [74] predicts metallic behavior and misses the photoemission triplet. Adding charge-self-consistency [75] opens a gap, but still misses the photoemission triplet. LDA+DMFT with either exact diagonalization in a small Hilbert space [76] or Hubbard-I [77] as the impurity solver describes the photoemission triplet but fails to explain the resistivity.

In this article, we elucidate the mechanism driving the electronic trends between the pnictides and chalcogenides within a single framework. We find that the chalcogenides are mixed-valent compounds where valence fluctuations combine with the underlying Pu atomic multiplet structure to drive the formation of a multiplet of many-body quasiparticle peaks (“quasiparticle multiplets”) which correspond to the observed photoemission triplet. These heavy quasiparticles strongly affect the density of states at the Fermi level as a function of temperature, corroborating the gap-like resistivity and large specific heat at room temperature. Using analytic methods, we provide a description of the quasiparticle multiplet formation and their coexistence with the development of a gap. In contrast, the chemistry of the pnictides shifts the atomic multiplet energies, rendering valence fluctuations too costly, thereby localizing the f electrons.

6.2 Numerical Method and Results

We use LDA+DMFT [9, 14] with OCA [78] as the impurity solver to model the chalcogenides and pnictides, taking PuTe and PuSb as representatives of the two groups due to the special attention [65, 67, 68, 71, 62] accorded to them in the available experimental data. In our calculations, we use the projective orthogonalized LMTO basis set [79]. We use $F^0 = 4.5$ eV for the Hartree component of the Coulomb interaction,

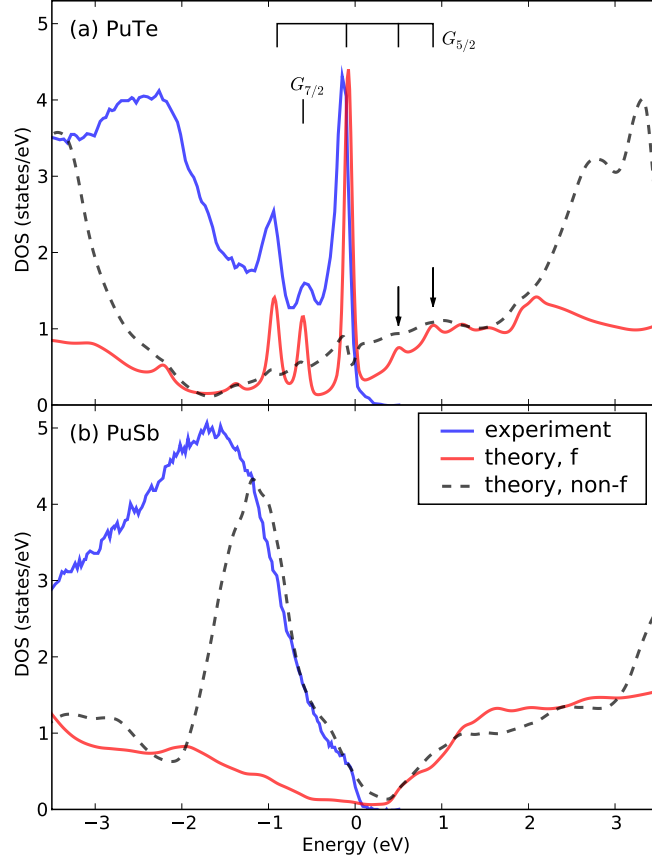


Figure 6.4: Computed spectra for (a) PuTe and (b) PuSb, separated into f and non- f (uncorrelated spd) partial densities, compared with photoemission [71]. A triplet of peaks are present in PuTe, as well as a predicted reflected doublet of peaks (arrows), while neither appear in PuSb. Application of broadening (40 meV) has blurred the gap in PuTe (see Fig. 6.5).

consistent with previous work [80, 81, 82]. The remaining Slater integrals $F^2 = 6.1$ eV, $F^4 = 4.1$ eV and $F^6 = 3.0$ eV are calculated using Cowan’s atomic structure code [83] and reduced by 30 % to account for screening. The double counting energy is taken to be $E_{DC} = U(n_f^0 - 1/2) - J(n_f^0 - 1)/2$ where $n_f^0 = 5$ is the central f -valence. We want to emphasize that identical correlations are applied to PuTe and PuSb, which translates to using a single set of atomic parameters F^n and E_{DC} for all computations. The differences in physics originate entirely from changing the alloying element from Te to Sb in the chemical structure.

In Fig. 6.4, we show the computed spectral functions for PuTe and PuSb, resolution-broadened by 40 meV and overlaid with experimental photoemission data [71]. The calculations clearly corroborate the presence of the photoemission triplet in PuTe at

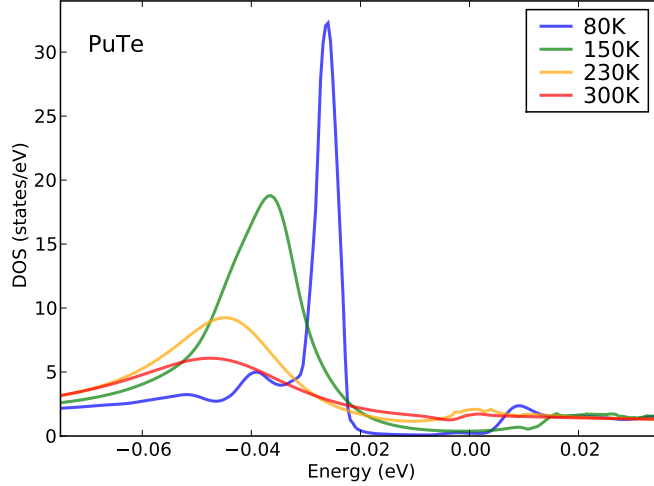


Figure 6.5: Detail of PuTe spectrum near Fermi level, showing development of gap and formation of main quasiparticle peak with decreasing temperature.

the correct energies, and their absence in PuSb. Furthermore, we predict the existence of a doublet of peaks (arrows) in PuTe at reflected energies about the Fermi level. The strong temperature dependence of all five peaks indicates they are quasiparticle resonances. Examining the main quasiparticle peak at the Fermi level (Fig. 6.5), we find it is composed of heavily renormalized quasiparticles with $Z \approx 0.1$, giving a greatly enhanced specific heat. Additionally, the peak sharpens with decreasing temperature, considerably reducing the density of states at the Fermi level, leading to the formation of a gap and the observed temperature dependence in the specific heat [64]. Together, the reduction of Fermi level density and heavy renormalization explain how a gap-like resistivity can coexist with a large specific heat coefficient at room temperatures.

A useful way to analyze the Pu atomic environment is to quantify the amount of time the f -electrons spend in each atomic configuration as they fluctuate between the atom and conduction band. To this end, we project the DMFT ground state $|\Omega\rangle$ onto the Pu f -electron atomic eigenstates, resulting in the probabilities $P_m = Z^{-1}\langle\Omega|X_{mm}|\Omega\rangle$, where $Z = \sum_m \langle\Omega|X_{mm}|\Omega\rangle$ is the normalization and X_{mm} is the Hubbard operator which projects onto the m th atomic eigenstate [82]. Plotting P_m against the atomic energies gives a valence histogram (Fig. 6.6) which graphically represent the relative weights of the atomic configurations comprising $|\Omega\rangle$. The f valence can then be defined by $\langle n_f \rangle = \sum_m P_m n_m$, where n_m is the number of electrons in the m th state.

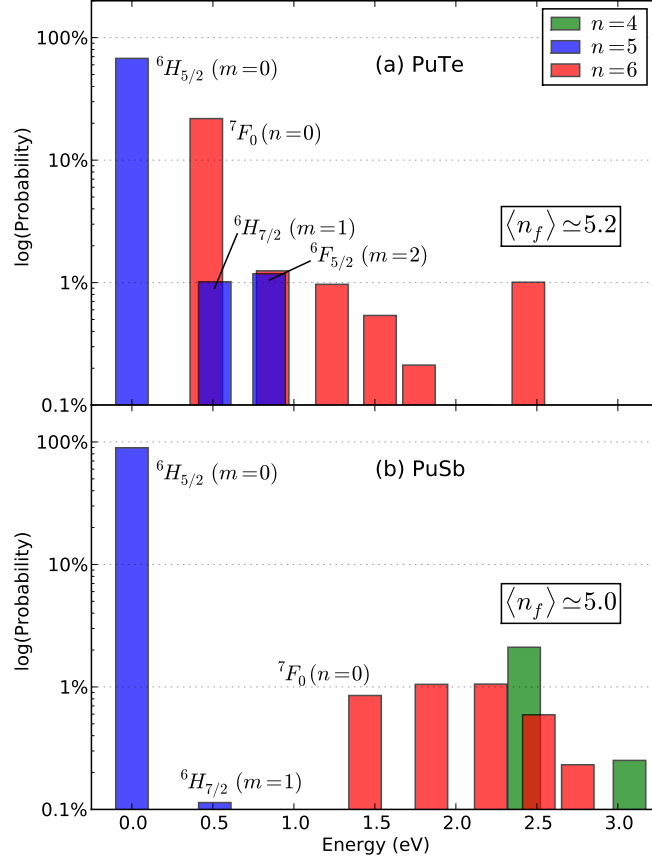


Figure 6.6: Valence histograms obtained by projection of DMFT solution ($T = 60$ K) onto Pu atomic eigenstates, plotted with energies relative to lowest-energy atomic state. The height of each bar represents the percentage of time the atom spends in each configuration. PuTe is strongly mixed-valent due to the small energy cost (≈ 0.5 eV) of valence fluctuations from f^5 to f^6 , while PuSb is integral valent due to the large cost of fluctuations to both f^4 and f^6 . In PuTe, additional fluctuations to atomic multiplets ${}^6H_{7/2}$ and ${}^6F_{5/2}$ are crucial to the creation of the photoemission triplet. All quantum numbers are gathered into a single index m or n used in the slave-boson calculation. Approximate term symbols are given although L and S strictly are not good quantum numbers.

The histograms show that the Pu atom is restricted to just one or two valences in both compounds. In fact, the atom mostly exists in a single f^5 configuration (${}^6H_{5/2}$, tall blue bar), which we loosely call the “ground state”. However, PuTe differs from PuSb in that its electrons have an over 20 % probability to fluctuate to the lowest f^6 state (7F_0 , leftmost red bar) due to this state’s small 0.5 eV separation from the “ground state”. The resulting mixed-valent ($\langle n_f \rangle = 5.2$) Pu atom strongly suggests a Kondo-like, and thus nonmagnetic, ground state in PuTe. Additionally, the proximity in energy of the next two higher f^5 states (${}^6H_{7/2}$ at 0.5 eV and ${}^6F_{5/2}$ at 0.9 eV) renders

these multiplets accessible to valence fluctuations, which will play a role in generating the photoemission triplet. In contrast, the Pu atom is integral-valent ($\langle n_f \rangle = 5.0$) in PuSb. Within LDA, the $j = 5/2$ f -bands are higher in energy in PuSb, raising the energy of the f^6 states relative to the f^5 . The resulting 1.5 eV gap locks Pu into the lowest f^5 state and PuSb remains a local moment metal.

6.3 Slave-Boson Analysis

To gain additional insight into the LDA+DMFT solution, we construct a Hamiltonian for the DMFT quantum impurity. The histograms indicate we only need to keep two valences in the atomic Hilbert space for a low-energy model,

$$H_{\text{atom}} = \sum_m E_m^f f_m^\dagger f_m + \sum_n E_n^b b_n^\dagger b_n, \quad (6.1)$$

where the auxiliary fermions $f_m^\dagger|0\rangle = |m; f^5\rangle$ and bosons $b_n^\dagger|0\rangle = |n; f^6\rangle$ create the atomic eigenstates, and E_m^f and E_n^b are the corresponding atomic eigenenergies. The Hamiltonian is supplemented by the constraint $Q = \sum_m f_m^\dagger f_m + \sum_n b_n^\dagger b_n = 1$, in the same spirit as the slave-boson construction [22, 84]. The atom hybridizes with an auxiliary conduction bath,

$$H_{\text{c,mix}} = \sum_{k\alpha} \epsilon_{k\alpha} n_{k\alpha} + \sum_{k\alpha} (V_{k\alpha} d_\alpha^\dagger c_{k\alpha} + \text{h.c.}), \quad (6.2)$$

where d_α^\dagger creates an electron in the α th atomic crystal field basis and k is the dispersion of the conduction bath. Since we work in the atomic eigenbasis, we eliminate d^\dagger in favor of the auxiliary particles by expanding $d_\alpha^\dagger = b_n^\dagger (F^{\alpha\dagger})_{nm} f_m$, where $(F^{\alpha\dagger})_{nm} = \langle n | d_\alpha^\dagger | m \rangle$ are the matrix elements of the physical electron creation operator.

This model is equivalent to the slave-boson treatment of the multi-orbital Anderson impurity model [23, 24], so we can compute the mean-field solution and fluctuations. At the mean-field level, we replace the bosonic operators by their averages, $\langle b_n^\dagger \rangle^2 = \langle b_n \rangle^2 \equiv z_n$ which are the probabilities of the f^6 atomic states (red bars in Fig. 6.6). Then, the physical Green's function is

$$G_{\alpha'\alpha}(i\omega) = \sum_{m'n'nm} F_{m'n'}^{\alpha'} (F^{\alpha\dagger})_{nm} \sqrt{z_{n'} z_n} G_{m'm}^f(-i\omega), \quad (6.3)$$

where the auxiliary f propagator and hybridization are

$$G^f(i\omega)_{m'm}^{-1} = (i\omega - E_m^f - \lambda)\delta_{m'm} + i\Delta_{m'm} \text{sgn } \omega, \quad (6.4)$$

$$\Delta_{m'm} = \sum_{n'n\alpha} F_{m'n'}^\alpha (F^{\alpha\dagger})_{nm} \sqrt{z_{n'} z_n} \Delta_{\alpha\alpha}, \quad (6.5)$$

and the hybridization $\Delta_{\alpha\alpha'}$ is approximated as an energy-independent constant. Here, λ is the Lagrange multiplier used to maintain $\langle Q \rangle = 1$. The crucial minus sign $G_{m'm}^f(-i\omega)$ arises because the propagation of a physical electron $\sim \langle d(\tau)d^\dagger \rangle$ corresponds to an f -hole.

In the Kondo regime, the mean-field equations (see Appendix C for an introduction to the method and detailed derivation of these results) give

$$T_K \simeq D e^{-\frac{\pi(\langle E^b \rangle - E_0^f)}{\Delta_{00}/z}} \prod_{m \neq 0} \left(\frac{D}{E_m^f - E_0^f} \right)^{\Delta_{mm}/\Delta_{00}}, \quad (6.6)$$

where $z = \sum_n z_n$ is the total f^6 probability and $\langle E^b \rangle = z^{-1} \sum_n E_n^b z_n$ is the weighted average of the f^6 energy levels. We ignored the off-diagonal components of $G_{m'm}^f$, which are negligible compared to the diagonal components when $|E_{m'}^f - E_m^f| \gg \Delta_{m'm}$. In the Kondo regime, $\lambda \approx -E_0^f$, pinning the lowest f propagator near the Fermi level.

For PuTe, we explicitly evaluate the sum in (6.3) to determine the origin of the photoemission triplet. Keeping just $z_0 \approx 0.20$ since the remaining z_n are negligible (see Fig. 6.6), we find that only three matrix elements have significant weight: $F_{00}^{5/2}$, $F_{02}^{5/2}$ and $F_{01}^{7/2}$. Again ignoring off-diagonal terms, we find for the physical Green's function

$$G_{5/2}(\omega) = z_0 |F_{00}^{5/2}|^2 G_{00}^f(-\omega) + z_0 |F_{02}^{5/2}|^2 G_{22}^f(-\omega), \quad (6.7)$$

$$G_{7/2}(\omega) = z_0 |F_{01}^{7/2}|^2 G_{11}^f(-\omega). \quad (6.8)$$

The selection rules contained in the matrix elements determine the spin-orbit structure of the spectrum: $G_{5/2}$ contains the main peak at the Fermi level and the weaker peak at -0.9 eV (labeled by brackets in Fig. 6.4), while $G_{7/2}$ contributes the third peak at -0.5 eV. Plugging in $D = 1.0$ eV and $\Delta_{5/2} = \Delta_{7/2} = 0.04$ eV into (6.6) gives $T_K \approx 500$ K in PuTe, so the peaks have sufficient width to be seen in photoemission. Numerical solution of the mean-field equations with a small hybridization

gap, $\Delta_{\alpha\alpha}(\omega) = \Delta_{\alpha\alpha}[\theta(\omega - E_g) + \theta(-\omega - E_g)]$, confirms that for $2E_g \lesssim T_K$, the resonances are not destroyed. Thus, in PuTe, valence fluctuations create three Kondo peaks in the DMFT quantum impurity with spacings determined by the underlying atomic multiplets, corresponding to the quasiparticle triplet in the lattice.

Proceeding to PuSb, the decrement in valence allows Pu to fully transfer three electrons to the pnictogen and exist purely in a trivalent state. Energetically, this is accomplished by raising the f^6 multiplets with respect to the f^5 states, inducing a four-fold increase in $\langle E^b \rangle - E_0^f$ from 0.5 eV to 2.0 eV. This exponentially suppresses the Kondo temperature of PuSb to under 1 K, eliminating the Kondo peaks, localizing the f -electrons and allowing magnetically-ordered states at low temperature.

To explain the Hubbard bands and reflected doublet of peaks above the Fermi level, we compute corrections to the mean-field solution. These corrections show that the bare atomic multiplets generate Hubbard bands, which are too broad to be seen in Fig. 6.4. We emphasize that the photoemission triplet is not directly attributed to atomic multiplets, but rather to quasiparticles. Additionally, the corrections to mean-field show that the reflected doublet of peaks arises from overlap of the ground state Kondo singlet with two excited Kondo singlets (Fig. 6.7). While the ground state is primarily a singlet formed between f_0 and a conduction electron, the two excited states are singlets formed with f_1 and f_2 in place of f_0 . Since the atomic multiplets f_1 and f_2 lie at energies 0.5 eV and 0.9 eV above f_0 , the two excited Kondo singlets lie at these energies as well. To generate the spectrum, an electron is first added to the ground state singlet to create a photoelectron state (Fig. 6.7d), which is overlapped with the excited singlets. The overlap is non-zero since all states have an f^6 component due to valence fluctuations, resulting in a doublet of reflected peaks.

6.4 Summary

Our LDA+DMFT calculations account for the complex trends observed in experiment across the Pu chalcogenides and pnictides. These include the formation of a low-temperature gap at the Fermi level accompanied by quasiparticle multiplets in the

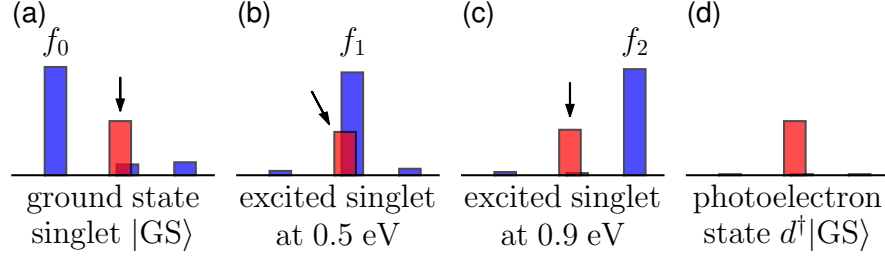


Figure 6.7: Valence histograms of states responsible for the predicted doublet of peaks above the Fermi level in PuTe. Histograms (a)-(c) depict the ground state and two excited Kondo singlets respectively. All three state have significant f^6 weight (arrows) due to strong valence fluctuations. Histogram (d) is the photoelectron state $d^\dagger|\text{GS}\rangle$ generated by the addition of an electron to the ground state. Since d^\dagger destroys f_m and creates b^\dagger , the result is a state which is entirely f^6 in character. The large f^6 admixture in the excited singlets means they will overlap strongly with the photoelectron state, giving rise to the doublet of peaks at 0.5 eV and 0.9 eV.

photoemission spectrum. Our theory elucidates the mechanism for the emergence of the quasiparticle multiplet excitations. These excitations represent the remnants of the atomic structure in the low-energy spectra, which is entirely described in terms of quasiparticles. The spectra and f -occupancy confirm that the chalcogenides are correlated low-carrier materials in the mixed-valent regime. The chemistry of the pnictides increases the cost of fluctuations and renders the pnictides divalent, thereby eliminating the quasiparticle multiplets.

Our theory has several experimental consequences for the chalcogenides: there should be a quasiparticle doublet at positive energies 0.5 eV and 0.9 eV which can be probed by inverse photoemission techniques. Furthermore, the quasiparticle multiplets can be detected as side-peaks in the optical conductivity, again at 0.5 eV and 0.9 eV. It would be interesting to study the temperature dependence of both the photoemission and optics near the coherence temperature (500 K) as we expect strong temperature dependence due to the many-body nature of the quasiparticle multiplets. Finally, the mechanism we outline is fairly general and applies to other correlated materials, provided the coherence temperature is large enough to be observed and less than the atomic multiplet splitting.

Chapter 7

Optical Conductivity in Lanthanum Nickelate Films

The rare-earth nickelates $R\text{NiO}_3$ are a well-studied family of perovskites, consisting of a cubic lattice of nickel ions with an oxygen lying on the edge between each nearest neighbor pair of nickels (Fig. 7.1). The rare earth ions R are situated at the center of the nickel cubes. As the Ni-O bond length is fairly rigid, the ionic radius of R determines the amount of distortion away from a perfect cubic lattice: the Ni-O-Ni bonds cooperatively buckle to match the volume of the nickel cubes to the space filled by the R ion. This buckling is quantified by the Goldschmidt tolerance factor $t = d_{R-O}/\sqrt{2}d_{\text{Ni-O}}$, where d_{R-O} is the distance between the rare-earth and the nearest oxygen, and $d_{\text{Ni-O}}$ is the Ni-O bond length [85]. As the value of t decreases from unity, lattice buckling increases.

Structure has a strong effect on the electronic behavior of the nickelates. As shown in Fig. 7.2, the $R\text{NiO}_3$ family exhibits a metal-insulator transition as a function of the ionic radius of the rare-earth R or equivalently the tolerance factor t . The nickelates are charge-transfer insulators [86]. The nickelate with the largest rare-earth ion, LaNiO_3 , does not exhibit any phase transitions. As the radius of R is decreased, the conventional physical picture argues that the increase in Ni-O-Ni bond bending decreases orbital overlaps, thereby reducing the kinetic energy. The Coulomb repulsion on the localized $3d$ orbitals on the nickel sites remains unchanged. Thus the overall strength of correlations is enhanced, favoring the insulating state and concomitant charge and spin ordering. In PrNiO_3 and NdNiO_3 , the metal-insulator transition is concomitant with antiferromagnetic ordering, whereas for the SmNiO_3 and beyond, the metal-insulator transition separates from the magnetic ordering temperature of the

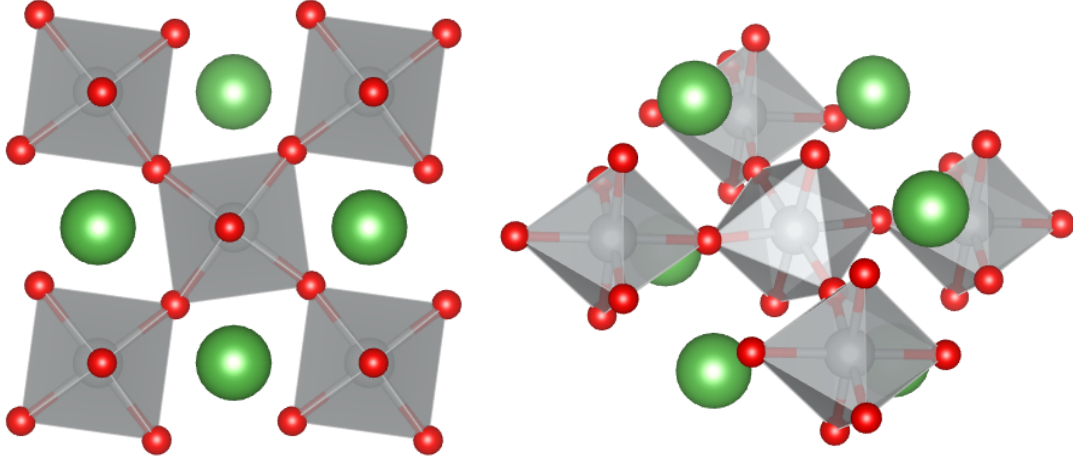


Figure 7.1: Two views of the perovskite LaNiO_3 showing the nickel ions forming a cubic lattice, surrounded by octahedral cages of oxygens.

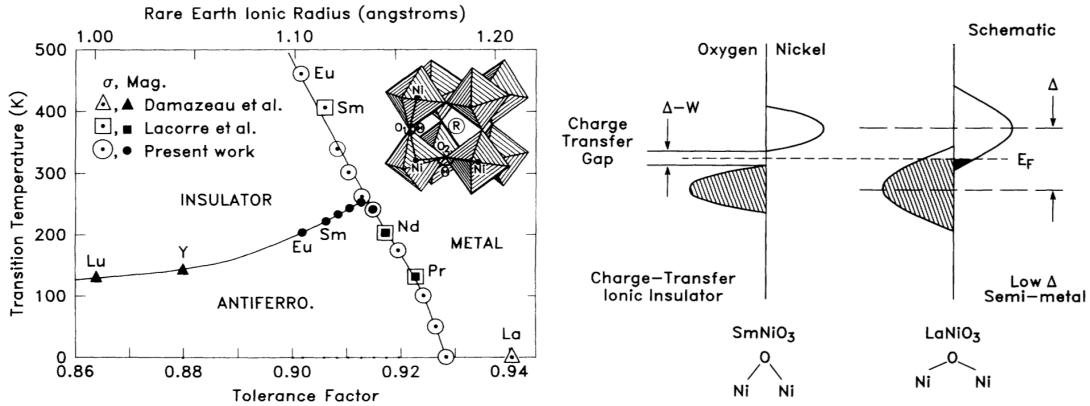


Figure 7.2: (left) Phase diagram of the rare-earth nickelates as a function of temperature and tolerance factor[87]. There is a systematic trend with the tolerance factor, or equivalently, the rare-earth ionic radius. (right) Schematic model describing the metallic and insulating states.

$3d$ electrons.

In some ways, the rare-earth nickelates are more complex than the cuprates because of orbital degrees of freedom: the $3d^7$ electronic configuration of the nickel ion combined with the octahedral environment formed by the oxygen cages implies one electron will occupy the two e_g orbitals. The interplay between the spin, orbital and structural degrees of freedom in this strongly-correlated family of compounds makes them a challenge for first-principles modeling, and a stringent test of our DFT+DMFT implementation.

This chapter contains our contributions to the work published in Refs. [88] and [89].

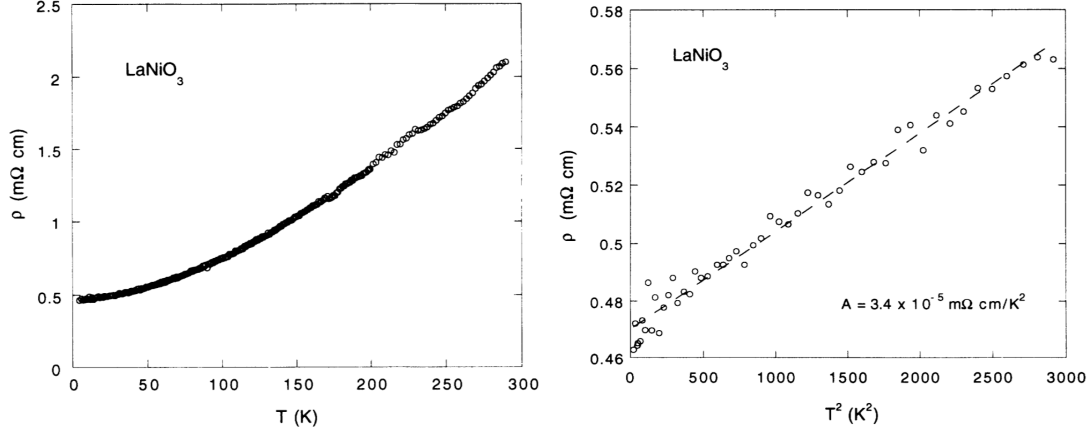


Figure 7.3: (left) The resistivity of bulk polycrystalline LaNiO_3 shows metallic behavior [92]. (right) Low-temperature zoom of resistivity, plotted as a function of T^2 [92]. The straight line implies Fermi liquid behavior.

7.1 Introduction

The proposal of superconducting superlattices formed by layering the two perovskites LaNiO_3 and LaAlO_3 is an ambitious attempt to engineer novel electronic states [90, 91]. LaAlO_3 (LAO) is wide band gap insulator, while LaNiO_3 (LNO) is a correlated metal (Fig. 7.3). Structurally, LNO is similar to the copper-oxide superconductors, but its electronic state differs in one key respect: it has one electron in two degenerate e_g orbitals. In order to mimic cuprate superconductivity, the proposals call for synthesizing superlattices of LAO/LNO. The symmetry of the nickel site in LNO is now tetragonal, breaking the degeneracy between the $d_{x^2-y^2}$ and d_{z^2} orbitals. Combined with the lack of hopping perpendicular to the NiO_2 planes in the LNO, since it has been sandwiched between layers of insulating LAO, the proposal hoped to create a single half-filled band of 2D electrons in a non-cuprate-based material. Successfully inducing strongly-correlated superconductivity in the assemblage of two non-superconducting materials would be a breakthrough.

However, our limited understanding of LNO in isolation hinders the ability to reliably predict its behavior in heterostructures. A detailed optical study of this oxide, combined with realistic first-principles modeling would be of great use. Additionally, LNO has not been thoroughly characterized in thin-film form. A second, more fundamental reason for studying LNO lies in understanding spectral weight transfer in

strongly-correlated systems [10]. Starting from the insulating side of a metal-insulator transition, the creation of the low-energy conducting quasiparticles involves the transfer of spectral weight across many eV of energy. LNO offers a clean system to study this spectral weight transfer as it does not exhibit any competing spin, charge or structural orderings.

The experimental data to which we compare our theoretical results are epitaxial LNO films grown by pulsed laser deposition, controlled by reflection high-energy electron diffraction (RHEED) [88, 89]. The films were grown on LaAlO_3 (LAO) and SrTiO_3 (STO) substrates, with -1.2% and +1.7% lattice mismatches, respectively. Two thicknesses of films were grown on both substrates: thick films of height 200 nm, and ultrathin films of height 12 nm (equivalent to approximately 510 and 30 unit cells thick, respectively). Optical measurements were performed carried out via variable angle spectroscopic ellipsometry (VASE) between 20 and 298 K.

The DFT bandstructures were computed within the FP-LAPW scheme [48] using room temperature bulk LNO structural parameters [93], as well as the strained structures as determined for LNO epitaxy on STO and LAO [94]. The calculations were performed on a $9 \times 9 \times 9$ k -space grid with RKMAX set to 9.0, and converged to 0.1 mRy in energy and 0.0005 in charge distance.

Charge self-consistent DFT+DMFT [9] calculations were performed using the implementation described in Ref. [31]. We used $U = 7.3$ eV and $J = 1$ eV for the strength of the Coulomb repulsion on Ni d -orbitals, and $E_{\text{dc}} = U(n_d - 1/2) - J(n_d - 1)/2$ as the standard double counting energy, where $n_d = 7.3$ is the average d valence. A range for J and U was determined based on previous studies of this class of compounds and then scanned to obtain the best fit to our optics data as well as to ARPES [95] and thermal measurements [96]. In order to compute the optical conductivity, we analytically continued the self-energy using modified Gaussians [31] and cross-checked the result with maximum entropy. The conductivity was then computed using the DFT momentum matrix elements and convolving the correlated Greens function for all values between 6 eV and 6 eV, relative to the Fermi level.

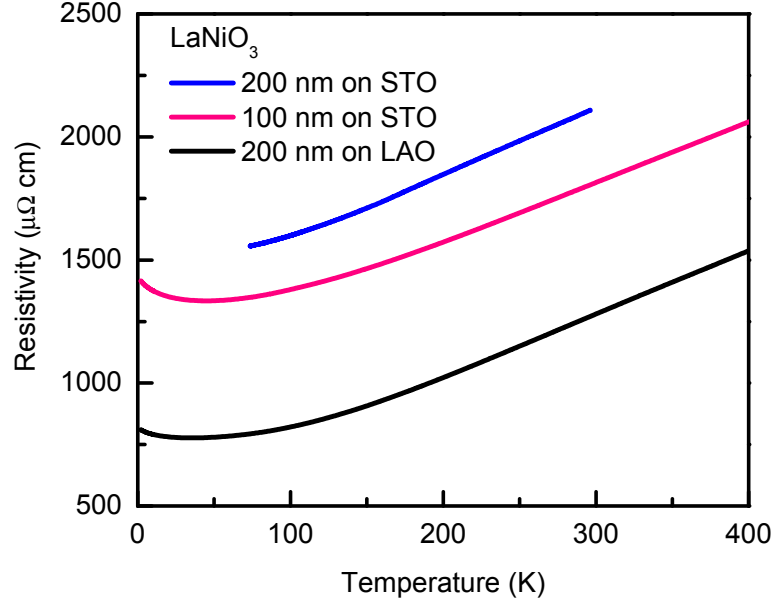


Figure 7.4: Resistivity of LaNiO_3 thin films deposited on SrTiO_3 (STO) and LaAlO_3 (LAO). We note the resistivity of the films are two to three times larger than bulk measurements. Figure courtesy Ref. [88].

7.2 Optical Conductivity of LNO Films

Resistivity data of the thick LNO films, plotted in Fig. 7.4 over a wide temperature range, show metallic behavior similar to the bulk polycrystalline samples. The 100-200 nm thick films are expected to be essentially strain-free, while the ultrathin films are expected to be coherently strained due to the lattice mismatch with the substrate. For these thick films, we find the LNO films on LAO to be more metallic than those on STO.

To probe the electronic structure, the optical conductivity $\sigma(\omega)$ was measured, which is related to the complex dielectric function via $\epsilon(\omega) = 1 - 4\pi\sigma(\omega)/i\omega$. The real (dissipative) part of the conductivity measured at room temperature is plotted in Fig. 7.5. The most surprising aspect is the lack of a well-defined Drude peak, considering the metallic transport of LNO. The main features above 1 eV, which have been labeled B-E, vary little across the films. However, the mid-infrared feature A exhibits stronger variation, presumably due to strain at the interface, even though the majority of the 200 nm thick film should be relaxed. The broad peaks centered at $\approx 300 \text{ cm}^{-1}$ are due to phonons.

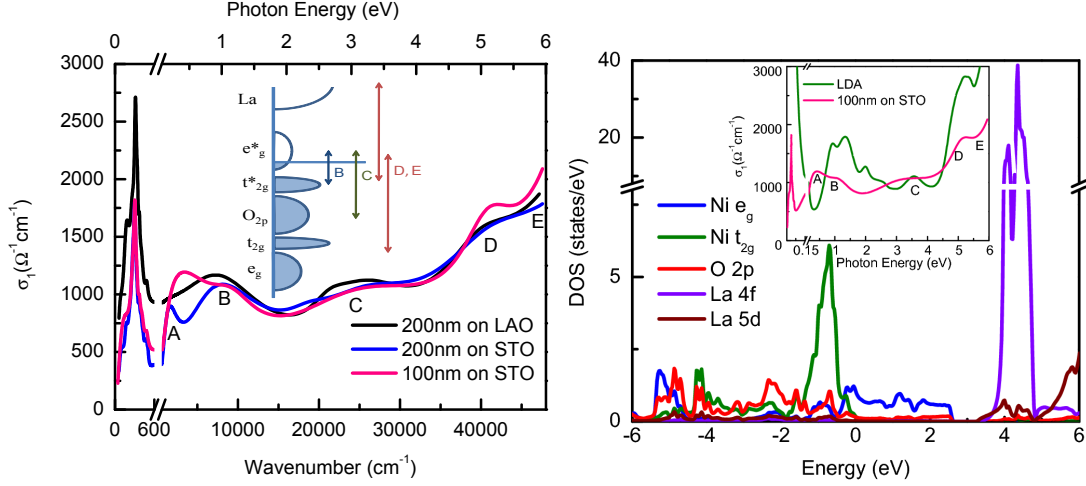


Figure 7.5: (left) Real part of the optical conductivity for three different thick LNO films measured at $T = 298$ K. The inset shows a rough sketch of the LNO density of states and interband transitions contributing to various observed peaks. (right) Partial density of states for LNO computed using DFT for bulk lattice parameters. The inset shows a comparison between the DFT optics as compared to the curve measured on the 100 nm LNO film on STO. The film shows a distinct lack of a Drude peak, in contrast to the DFT results. The sharp peaks observed at ≈ 0.05 eV are due to phonons. Figure courtesy Ref. [88].

We turn to DFT calculations to assist our understanding. In right panel of Fig. 7.5, we plot the calculated LDA partial density of states. At the Fermi level, there is a finite density of states arising from bands of nickel e_g character, so we expect a robust Drude peak. The inset in Fig. 7.5 shows a comparison between the calculated DFT optics and experiment. The agreement at energies above ≈ 2 eV is acceptable. Decomposing the optical transitions between filled and unfilled states, we attempt to assign features B-D in Fig. 7.5 (left) to specific interband transitions. We suggest that B corresponds to transitions from the Ni t_{2g}^* and e_g^* levels to the Ni e_g^* orbitals. C could be due to transitions from the O 2p to the e_g^* orbitals. D and E may be the result of transitions from t_{2g}^* to the La 4f and 5d levels and from the bonding Ni e_g and t_{2g} orbitals to the e_g^* orbitals. However, there are strong deviations at low energies: DFT does not capture feature labeled A and produces a strong Drude peak, in contrast to experiment. These mismatches suggest correlations play an important role in LNO, and that methods such as DFT+DMFT, which capture the spectral weight rearrangement caused by electronic interactions, must be used for realistic descriptions.

7.3 Temperature-Dependence of Spectral Weight Transfer

In an effort to reduce the amount of structural defects due to the relaxation of the epitaxial strain, and to compare with the ostensibly “bulk” nature of the thick films, ultrathin samples of LNO on LAO and STO were synthesized [89]. The DFT+DMFT calculations have a better chance of good agreement with the optics measured on these cleaner, fully strained samples.

We show in Fig. 7.6 the real part of the optical conductivity for the ultrathin LNO samples grown on LAO and STO respectively (plotted on a log-log scale). In both films, a clear Drude peak characteristic of metals is visible. Four peaks A-D were observed, in agreement with the thick films. Additionally, an enhancement in the spectral weight under the Drude peak is observed as the temperature is lowered. In order to quantify the origin of this spectral weight transfer, the ratio of the low-temperature optics curves to the curve at room temperature was plotted. It was concluded that much of the weight is transferred from feature C located at 2 to 3 eV into the Drude peak as the temperature is lowered. The area under the Drude peak measures the kinetic energy K_{exp} of the conducting electrons. In the inset in Fig. 7.8, the extracted kinetic energies for the two thick (bulk) films as well as the two thin films is plotted. We find that both compressive (LAO) and tensile (STO) epitaxial strain enhances the weight under the Drude peak.

These results pose a challenge for first-principles methods. In Fig. 7.7, we plot the electronic spectral function $A(\mathbf{k}, \omega)$ for LNO computed using DFT+DMFT for bulk lattice parameters at 116 K. This quantity is directly probed in ARPES measurements, and gives valuable insight into the optical properties. The DFT+DMFT spectrum is strongly rearranged and broadened as compared to the bare LDA bandstructure. The nickel e_g bands, which cross the Fermi level, are broadened at higher energies, but remain sharp near the Fermi level. Thus we expect a robust, but reduced, Drude peak. Due to the renormalization factor $Z \approx 1/2$ to $1/3$, the e_g bands are compressed, which we expect to cause peaks A and B to shift downwards in energy. The strong broadening of the t_{2g} and oxygen $2p$ bands will cause the higher-energy features C-E to become

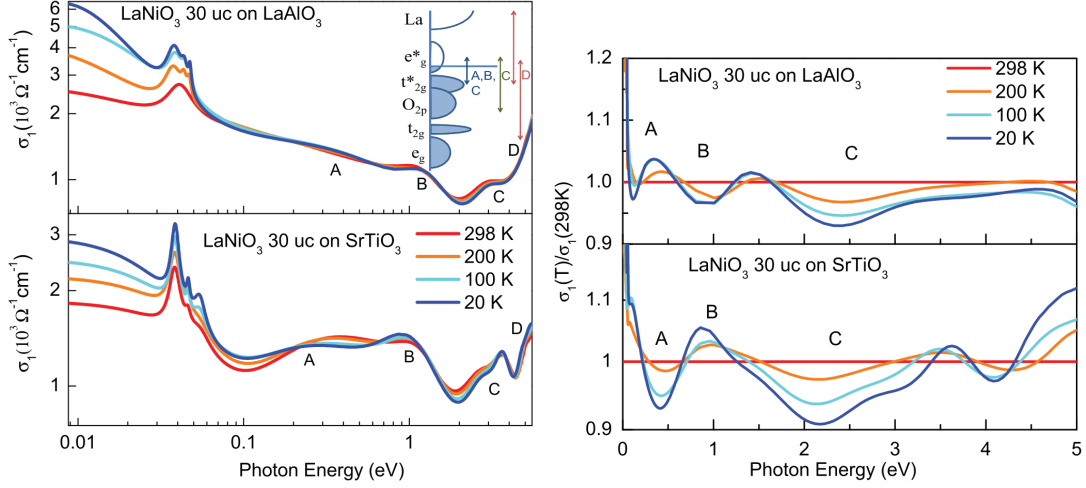


Figure 7.6: (left) Real part of the optical conductivity for LNO on LAO and STO, at four different temperatures. There is a clear Drude peak, which shows enhancement with the decrease in temperature. We show in the inset the interband transitions contributing to the features A-D, in agreement with the thick films (Fig. 7.5). The peaks at ≈ 0.04 eV are phonons. (right) Ratio of real part of optical conductivity at low temperatures to the curve at $T = 298$ K for LNO films on LAO and STO. This plot shows the spectral weight transfer from high energies, especially feature C, to the Drude peak, as the temperature is lowered. Figures courtesy Ref. [89].

much less sharp.

In Fig. 7.8, we plot the DFT+DMFT optical conductivity. DFT+DMFT provides a more accurate description of our experimental data than LDA. In particular, feature A is not evident in the LDA $\sigma_1(\omega)$ but is present in the DFT+DMFT results. The two peaks seen at 1 eV and 1.5 eV (A and B, respectively) in LDA shift to lower energy when correlations are included in DFT+DMFT, resulting in better agreement with experiment. In this picture, feature A is due to interband transitions from the t_{2g}^* and e_g^* orbitals. A redshift of feature C is also evident in DFT+DMFT, consistent with the scenario in which electronic correlations suppress the energy of interband transitions due to the quasiparticle renormalization. We note that even though the DFT+DMFT results reproduce the key experimental trends, the agreement is less than perfect. This is not surprising given that optics is one of the most challenging probes to match well theoretically. This is because the description of the optics data relies on the convolution of two Green's functions, which in turn is very sensitive to any small errors in the individual Green's functions. However, DFT+DMFT undoubtedly brings the bare LDA integrated spectral weight SW into better agreement with experiment. As

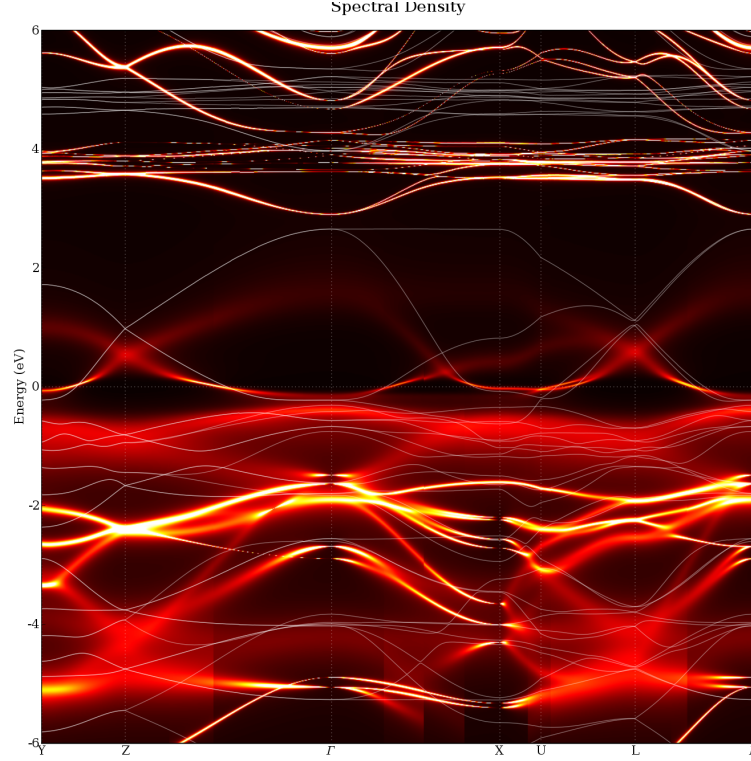


Figure 7.7: The spectral function $A(\mathbf{k}, \omega)$ for LaNiO_3 computed using DFT+DMFT for bulk lattice parameters at $T = 116$ K. The thin lines are the bare DFT bands. See text for description.

shown in Fig. 7.8 (bottom), DFT+DMFT transfers weight to higher energies, resulting in a ratio $SW_{\text{exp}}/SW_{\text{DMFT}}$ closer to unity.

The temperature dependence of the spectral weight transfer is also poses a challenge for theory. We display in Fig. 7.9 the temperature dependence of the computed optics curves. In contrast to experiment, we find that most of the spectral weight transfer occurs between the low-energy feature A and the Drude peak, rather than the higher interband peak C. Additionally, for the curves on STO, we observe that feature C fills in with the decrease in temperature, in opposition to experimental observations. We conclude that further studies are necessary to understand the temperature dependence of optical weight transfer in realistic models.

Returning to the Drude peak itself, one possible way to reconcile presence of a Drude peak in the ultrathin samples, but its absence in the thick samples is to point to sample morphology. In Fig. 7.10, we depict an educated guess regarding the structure of the LNO films. In thick films, the relaxation of epitaxial strain drives the formation of

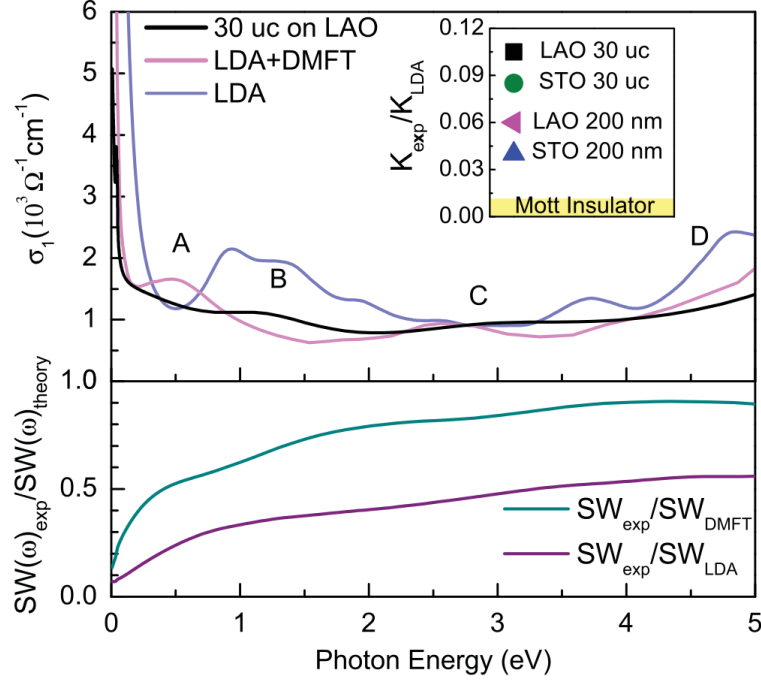


Figure 7.8: (top) Real part of the optical conductivity for an ultrathin 12 nm LNO film (compressively strained) on LAO substrate. Plotted for comparison are the computed LDA and LDA+DMFT optical conductivities. LDA+DMFT provides a better match to the features and spectral weight within the Drude peak. (inset) Electronic kinetic energy as determined by integrating under the Drude peak. (bottom) Ratio of integrated spectral weight obtained in experiment to the theoretically calculated weight in LDA and DFT+DMFT. Figure courtesy Ref. [89].

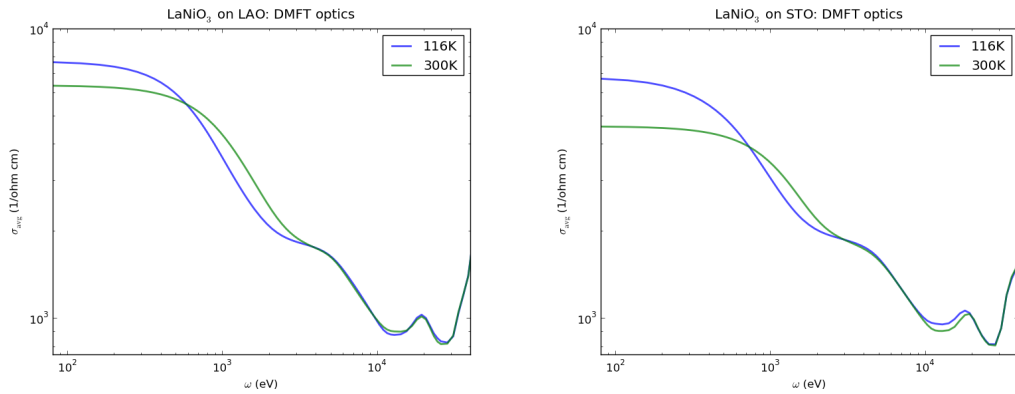


Figure 7.9: Temperature dependence of the optical conductivity of LNO on LAO (left) and STO (right) computed using DFT+DMFT. We find that the transfer of spectral weight is mostly between the Drude peak and the low-lying feature A, rather than with peak C as observed in experiment.

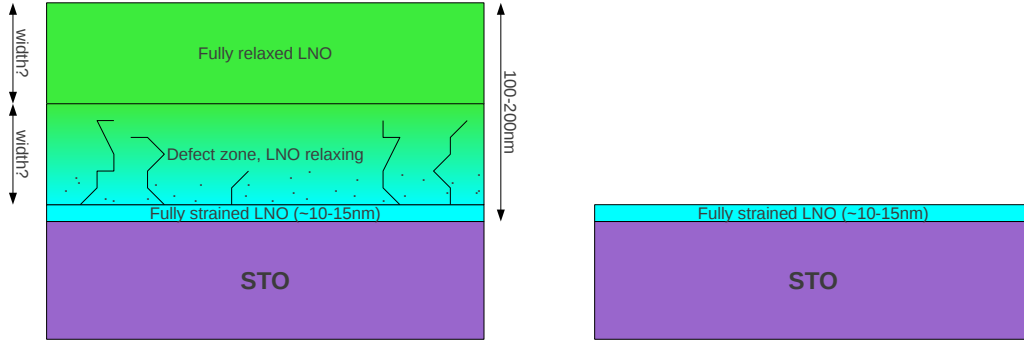


Figure 7.10: An educated guess regarding the structure of the thick (left) and ultrathin (right) LNO films. In thick films, the relaxation of epitaxial strain drives the formation of defects, causing poor electronic conduction and a large scattering rate of the Drude peak in the optical conductivity. In the thin films, the lack of defects due to strain relaxation gives good conductivity and a sharper Drude peak.

defects, causing poor electronic conduction and a large scattering rate of the Drude peak in the optical conductivity. In fact, there should be varying scattering rates since optics is a bulk-averaging probe. For the ultrathin films, the LNO film is coherently strained. The lack of defects due to strain relaxation implies a much sharper Drude peak. A possible test of this hypothesis is to compare the thick versus the ultrathin samples. We should find the Drude weight is only broadened about zero frequency, and not shifted to higher energies, but this comparison is difficult across sample preparations.

7.4 Summary

The optical conductivity of LNO films of varying thicknesses was measured on two different substrates: LAO and STO. The thick films, which are ostensibly fully relaxed, show no Drude peak, while the fully strained thin films exhibit enhanced metallicity and a clear Drude peak. The strong correlations present in the films cause spectral weight transfer over several eV of energy, which require many-body methods for accurate description. DFT+DMFT provides a satisfactory model of the higher energy features, above ≈ 1 eV, but there are discrepancies at low energies and in temperature trends. Considerations of sample disorder, the choice of orbitals within DFT+DMFT and double-counting corrections could help improve the agreement between theory and experiment.

Chapter 8

Correlating Superconducting Transition Temperatures in Hole-Doped Cuprates with the Charge-Transfer Energy

Superconductivity is a remarkable quantum state of matter some materials enter when cooled below a transition temperature, known as the critical temperature T_c . Depending on the material, the critical temperatures range from millikelvin to over 130 K. In terms of transport, the state is characterized by zero electrical resistivity, making them natural candidates for technological applications. However, even more remarkable is the thermodynamic property known as the Meissner effect: a superconductor completely expels magnetic fields below its transition temperature, even if the sample is cooled in-field (Fig. 8.1).

The history of superconductivity began with the discovery in 1911 by Kamerlingh Onnes that elemental mercury became superconducting at 4.2 K. The transition temperatures of these “conventional” superconductors inched upwards with the synthesis of simple binary metals (Fig. 8.1). The development of the BCS theory in 1957 [98] led to a firm microscopic understanding of conventional superconductors, showing that the interaction between electrons and phonons glued pairs of electrons together into Cooper pairs. It was believed that T_c ’s could never rise far above 30 K. In 1986, Bednorz and Müller discovered a new class of superconductors based on strongly-correlated transition metal oxides with complicated stoichiometries and materials chemistry [99].

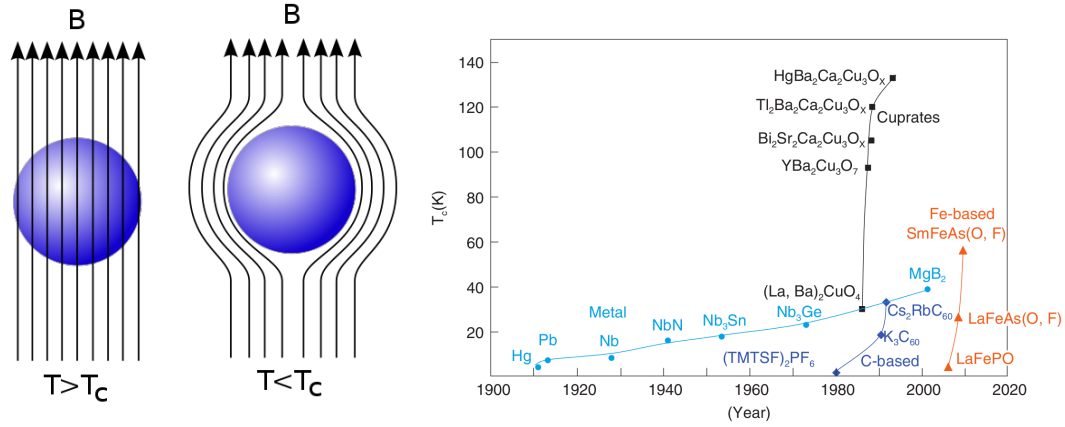


Figure 8.1: (left) Superconductors completely expel (quasi-static) magnetic fields, a phenomena termed the Meissner effect (image courtesy Wikipedia). (right) The trend of superconducting transition temperatures versus the year of discovery. The conventional superconductors, well-described by the BCS theory, show a slow upward trend stretching a century. In contrast, the high-temperature superconductors were first discovered in 1986, and in the time-span of a few years, their transition temperatures were pushed to above 130 K, but have not increased much further ever since. Figure courtesy Ref. [97].

In the span of a few years, the transition temperatures in these high-temperature superconductors jumped to over 130 K, above the boiling temperature of liquid nitrogen. However, the transition temperatures have not risen much in the intervening quarter of a century, and a consensus in theoretical understanding has likewise been slow to emerge.

The superconducting cuprates derive from a group of insulating, antiferromagnetic parent compounds. As explained in Fig. 8.3, the strength of electronic correlations in the cuprates is controlled by the charge-transfer energy. The copper ions in the CuO_2 planes are divalent, adopting a $3d^9$ configuration, leaving one hole per Cu site. The copper atoms are surrounded by a tetragonally distorted oxygen cage, so group theoretical arguments combined with electrostatics of the negative oxygen ions imply the hole in the d -shell must reside in the e_g orbitals. The combination of crystal field splittings and the lack of orbital overlaps along the c -axis lowers the $3d_{z^2}$ orbital below the Fermi level, rendering it fully filled by electrons. The hole resides in the half-filled $3d_{x^2-y^2}$ orbital, which hybridizes strongly with the in-plane oxygens. In these parent compounds, the lattice of $S = 1/2$ holes are localized due to the strong coulomb repulsion, and orders antiferromagnetically. The planes of CuO_2 planes are separated

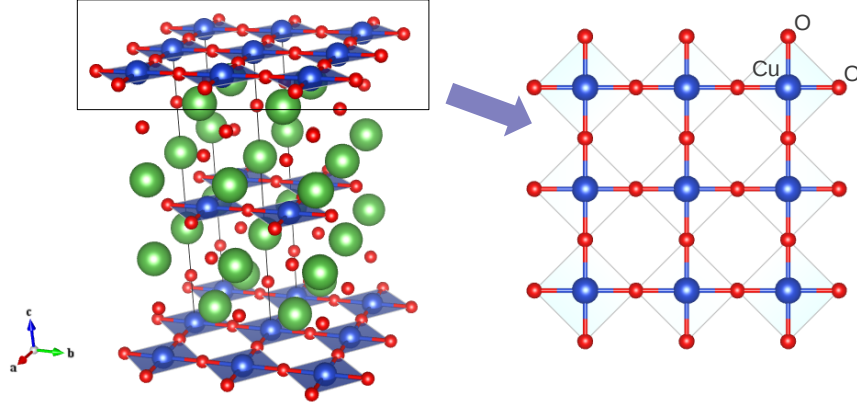


Figure 8.2: (left) The cuprates are layered compounds, containing square CuO_2 planes separated by spacer layers, generally composed of rare earth elements. The Cooper pairs responsible for superconductivity reside in the CuO_2 planes, which are the common structural motif across all members of the cuprate family. The spacer layers distinguish one cuprate from another, and their chemical properties tune the transition temperatures. (right) A vertical view of one CuO_2 plane, showing the square lattice of coppers, with the oxygens lying on the bonds.

by spacer layers, usually containing rare-earth elements.

Chemical doping p tunes through the cuprate phase diagram, as shown in Fig. 8.4. The doping is accomplished by varying the chemical composition of the spacer layers. Pushing the valence of the copper in the CuO_2 planes away from the integer $3d^9$ valence results in suppression of antiferromagnetic order and produces a dome of superconductivity in the doping-temperature phase diagram. Further doping produces a Fermi liquid. Doping with holes ($p > 0$) produces a much larger region of superconductivity than doping with electrons, as well as a finite-temperature phase known as the pseudogap, which exhibits various anomalous properties.

There is no universally accepted low-energy theory of cuprate superconductivity. However, since modern electronic structure methods can realistically capture intermediate energy scales (at the level of chemical bonding), we can approach the problem semi-empirically. In this work, we use first-principles calculations to extract two essential microscopic parameters, the charge-transfer energy and the inter-cell oxygen-oxygen hopping, which correlate with the maximum superconducting transition temperature $T_{c,\text{max}}$ across the cuprates. We explore the superconducting state in the three-band model of the copper-oxygen planes using cluster Dynamical Mean-Field Theory. We find that the variation in the charge-transfer energy largely accounts for the empirical

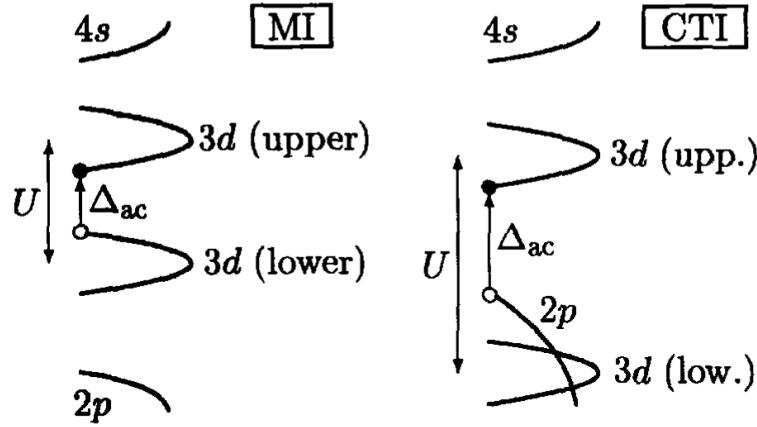


Figure 8.3: The cuprates are charge-transfer insulators (CTI), not Mott insulators (MI). In transition metal oxides, the presence of two different chemical species introduces a new energy scale in addition to the Coulomb repulsion U which controls the strength of electronic correlations: the relative energy level alignment between the transition metal $3d$ orbital ϵ_d and the oxygen $2p$ orbital ϵ_p . In Mott insulators, U is the smallest energy scale, the lowest-energy excitation is between the lower and upper Hubbard bands on the $3d$ site. In contrast, when $\epsilon_d - \epsilon_p < U$, the hopping of charge between the two chemical species is the lowest-energy excitation, termed a *charge-transfer* process, which controls the strength of electronic correlations. Image courtesy of Ref. [100].

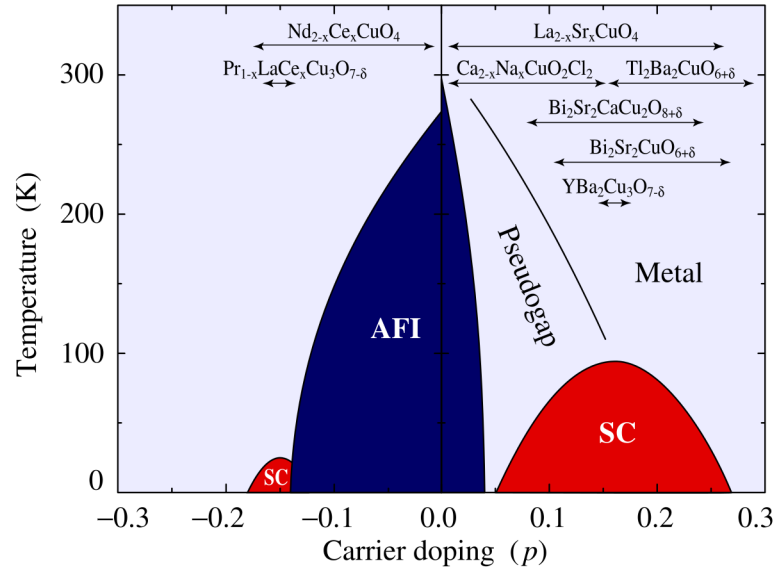


Figure 8.4: General doping-temperature phase diagram of the cuprate superconductors, showing the antiferromagnetic, superconducting and metallic phases [101]. Arrows mark the doping ranges experimentally accessible for various compounds.

trend in $T_{c,\max}$, resolving a long-standing contradiction with theoretical calculations.

8.1 Introduction

Despite an immense body of theoretical and experimental work, we have limited microscopic insights of which materials-specific parameters govern the trends in the maximum transition temperature $T_{c,\max}$ across the copper oxide superconductors. Structurally, all the cuprate families have in common CuO_2 planes which support superconductivity. They are described by the chemical formula $XS_{n-1}(\text{CuO}_2)_n$, where n CuO_2 planes are interleaved with $n - 1$ spacer layers S to form a multi-layer. These multi-layers are then stacked along the c -axis, separated by a different spacer layer X . Empirically, it is known that $T_{c,\max}$ is strongly materials-dependent, ranging from 40 K in La_2CuO_4 to 138 K in $\text{HgBa}_2\text{Ca}_2\text{Cu}_3\text{O}_8$. Additionally, $T_{c,\max}$ can be tuned both as a function of doping and the number n of CuO_2 planes.

Studies linking the known empirical trends to microscopics have generally established that the properties of the apical atoms (O, F or Cl, depending on the cuprate family) are the relevant materials-dependent parameters. However, conclusions vary regarding their effects on electronic properties, especially in multi-layer cuprates where not all CuO_2 have apical atoms. Early theoretical work by Ohta, *et. al.*, found correlations between T_c and the Madelung potential of the apical oxygen, arguing that the apical potential controls the stability of the Zhang-Rice singlets [102]. They conclude that $d_{\text{Cu-O}}^{\text{apical}}$, the distance between the Cu and apical O, is uncorrelated with superconductivity. In a more recent DFT study, Pavarini, *et. al.*, argue that $d_{\text{Cu-O}}^{\text{apical}}$ tunes between the single-layer cuprate families, affecting the electronic structure primarily via the one-electron part of the Hamiltonian [103]. Moving the apical oxygens away from the copper oxide plane allows stronger coupling of in-plane O $2p$ orbitals to the Cu $4s$, enhancing the strength of longer ranged hoppings. This effect is characterized by the increase of a range parameter $r \sim t'/t$, describing the relative strength of the next-nearest neighbor hopping t' to nearest neighbor hopping t in a one-band model. They find that materials with larger r have larger $T_{c,\max}$. Many-body corrections to t' were included by Yin, *et. al.* [104].

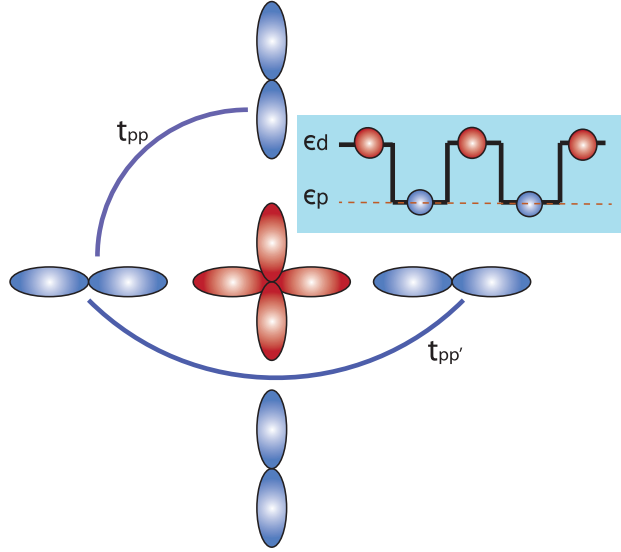


Figure 8.5: Parameters of the three-band p - d model for the CuO_2 planes in the cuprate superconductors. We show the two shortest-ranged oxygen-oxygen hoppings t_{pp} and $t_{pp'}$, and the on-site energies ϵ_d and ϵ_p .

The development of cluster Dynamical Mean-Field Theory (c-DMFT) combined with first-principles calculations (for reviews, see [105, 17]) has advanced our qualitative and quantitative understanding of the cuprates [106, 107]. A satisfactory description of these materials at intermediate energy scales has been achieved, and the consensus is that the cuprates lie in the regime of intermediate correlation strength [108, 109, 110, 111] near the Zaanen-Sawatzky-Allen (ZSA) boundary [86]. However, all numerical studies [112, 113, 114] contradict the empirical trend of $T_{c,\text{max}}$ with the range parameter r .

In this work, we address the origin of the variation of the experimental $T_{c,\text{max}}$ across the cuprates using recent advances in electronic structure methods. We carry out first-principles calculations of the hole-doped cuprates, extract chemical parameters by downfolding to the 3-band p - d model, and correlate them against $T_{c,\text{max}}$. Using c-DMFT, we explore the superconducting state and identify which parameter is the key driver of transition temperatures, resolving the conflict between numerics and the empirical findings of Ref. [103]. We conclude with suggestions for possible improvements in materials design to reach higher critical temperatures.

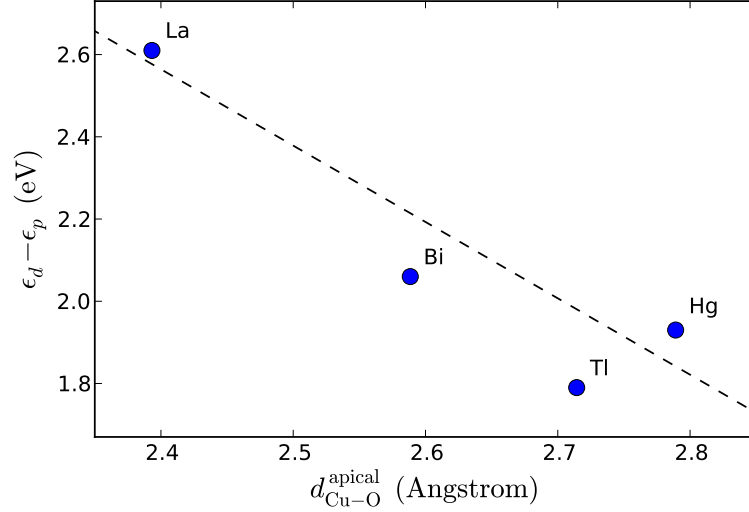


Figure 8.6: In single-layer cuprates, increasing the apical oxygen distance reduces the charge-transfer energy.

8.2 Extracting Chemical Parameters and Identifying Correlations

Effective low-energy hamiltonians containing the minimal set of bands are important tools for understanding chemical trends. We use the Wien2K code [48] to perform Linearized Augmented Plane Wave (LAPW) calculations on all major copper oxide families, and then extract model hamiltonian parameters by downfolding [115] to orbitals constructed in the manner described in Ref. [31]. In this work, we choose to downfold to a 3-band hamiltonian describing the in-plane $\text{Cu-}3d_{x^2-y^2}$ and $\text{O-}2p$ orbitals (Fig. 8.5). We believe four parameters capture the essential physics: the charge-transfer energy $\epsilon_d - \epsilon_p$ between the Cu and O atoms, the direct Cu-O hopping t_{pd} and the two shortest-ranged O-O hoppings t_{pp} , and $t_{pp'}$. The extracted values are tabulated in Table D.1 in Appendix D.

We find that only two parameters, $\epsilon_d - \epsilon_p$ and $t_{pp'}$, vary significantly across the cuprates. Although not crucial for our subsequent work, one would like to have a simple structural explanation for these trends. For the single-layer cuprates, the variation can be directly connected to $d_{\text{Cu-O}}^{\text{apical}}$ (also tabulated in Table I). As we bring the negatively-charged apical oxygen towards the CuO plane, the resulting electrostatic repulsion suppresses the hopping $t_{pp'}$, since $t_{pp'}$ describes transitions of electrons past the Cu site,

and provides justification for fact that $t_{pp'}$ is smaller than t_{pp} [112]. This mechanism for the dependence of hoppings on $d_{\text{Cu-O}}^{\text{apical}}$ has been pointed out in Ref. [103] for one-band models. However, we show in Fig. 8.6 that the electrostatic repulsion simultaneously increases $\epsilon_d - \epsilon_p$ by rendering it costly to place an electron on the Cu site. These simple structural trends are less clear for multi-layer cuprates, where additional variables such as the inter-layer distance introduce additional complexity.

Having identified the two relevant parameters, we plot $T_{\text{c,max}}$ against these quantities in Fig. 8.7a and Fig. 8.7b to identify possible correlations. Beginning with La_2CuO_4 (LSCO), the limiting case among the cuprates since it has the largest $\epsilon_d - \epsilon_p$ as well as the smallest $t_{pp'}$, the figures show that both (i) decreasing $\epsilon_d - \epsilon_p$ and (ii) increasing $t_{pp'}$ correlates with a enhanced $T_{\text{c,max}}$. To map our results to the one-band Hubbard model, we integrate out the oxygen orbitals to extract the range-parameter $r \sim t'/t$ (shown in Fig. 8.7c), and use the fact that the effective one-band correlation strength is controlled by $\epsilon_d - \epsilon_p$ in charge-transfer materials [116]. Our results show that both the *correlation strength* and *range parameter* vary significantly across the cuprates, in contrast with Ref. [103] which focused only on the latter.

8.3 Calculating Transition Temperatures Using Cluster-DMFT

In order to clarify how the identified microscopic parameters control $T_{\text{c,max}}$, we use c-DMFT in the cellular form [105, 17] with a 2×2 cluster of impurities to solve the downfolded three-band model. The non-local self-energy in c-DMFT captures the short-ranged correlations which are crucial to describe *d*-wave superconductivity. Since the fermionic minus sign problem prevents impurity solvers based on quantum monte carlo from accessing the low-temperature superconducting regime, we use finite-temperature exact diagonalization (ED) at $T = 30$ K as the impurity solver [117]. In this work, we extend previous c-DMFT calculations of the one-band model [113, 118] to the three-band model, with realistic parameters obtained from first-principles calculations. The refinement captures the admixture of the Cu and O character near the Fermi level via a bath representing both the Cu and O degrees of freedom in the DMFT self-consistency condition.

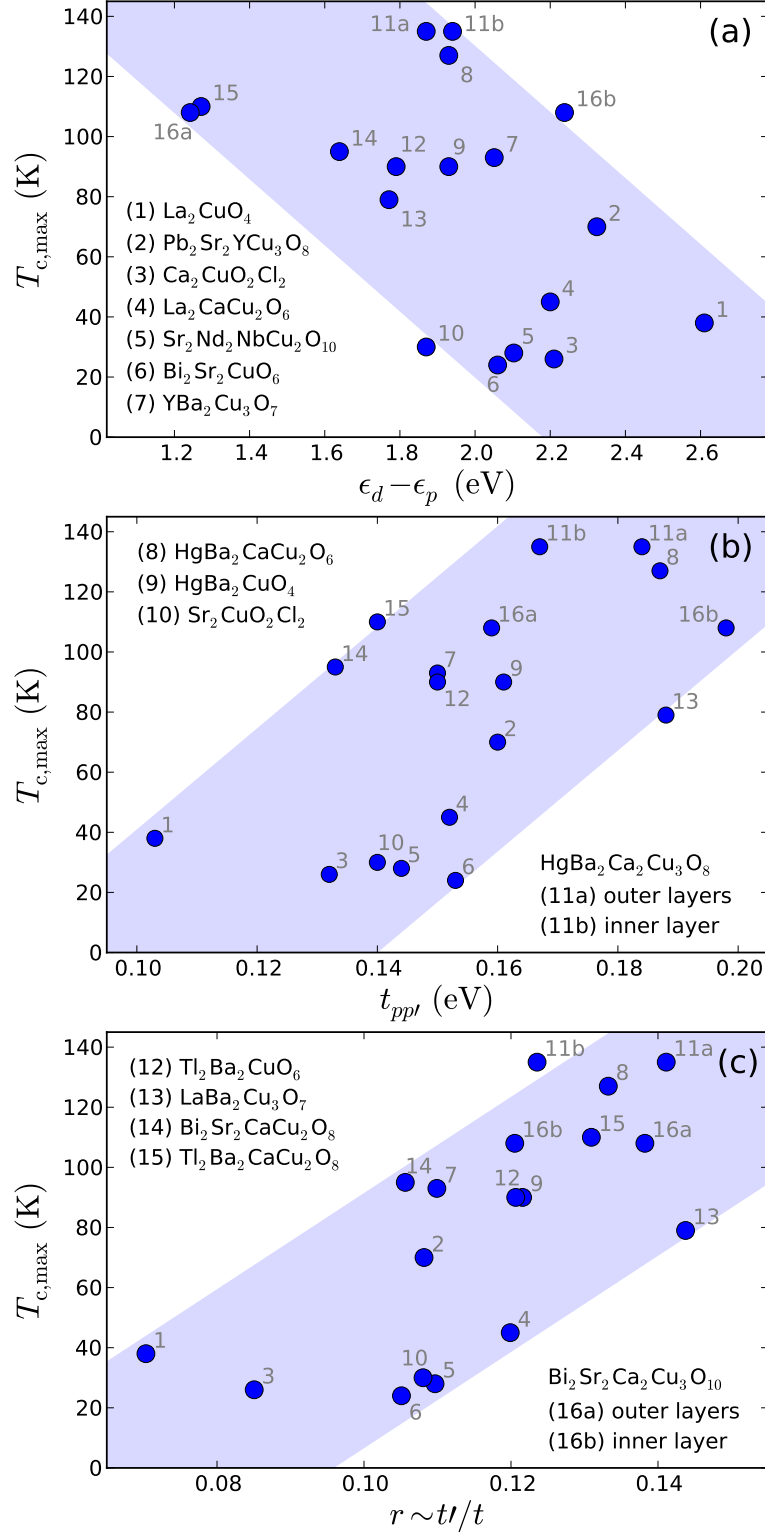


Figure 8.7: Correlations of $T_{c,max}$ in the copper oxides with the microscopic parameters of the three-band model Hamiltonian with (a) the charge-transfer energy $\epsilon_d - \epsilon_p$ (b) the next-nearest neighbor oxygen-oxygen hopping $t_{pp'}$ (c) the effective one-band range parameter $r \sim t'/t$. The trend of the dependence of the one-band range parameter agrees with Ref. [103].

The three-band hamiltonian we treat with c-DMFT is as follows:

$$H = \sum_{i\alpha j\beta\sigma} t_{ij}^{\alpha\beta} c_{i\alpha\sigma}^\dagger c_{j\beta\sigma} + \sum_{i\alpha\sigma} \epsilon_\alpha n_{i\alpha\sigma} + U_{dd} \sum_{i\sigma} n_{id\uparrow} n_{id\downarrow}$$

where i, j run over the in-plane CuO_2 unit cells, α, β label the orbitals p_x , p_y and $d_{x^2-y^2}$, and σ is the electron spin. The hoppings $t_{ij}^{\alpha\beta}$ and onsite energies ϵ_α are those sketched in Fig. 8.5, except for the d -orbital onsite energy, where we subtract out a doping- and material-independent double-counting correction E_{dc} to account for correlations included in both LDA and DMFT. The atomic double-counting [39], which is very successful for all-electron DFT+DMFT [31], cannot be used because the Wannier functions of the three-band model significantly depart from the atomic wavefunctions. To determine E_{dc} for the Wannier representation, we match the low-energy Matsubara Green's function of the three-band model to the corresponding quantity in the *ab initio* all-electron calculation (see Fig. D.2). A good match was attained for $E_{\text{dc}} = 3.12$ eV for an $d_{x^2-y^2}$ on-site Coulomb repulsion of $U_{dd} = 8$ eV.

To test our method, we use the extracted parameters for the canonical cuprate LSCO and explore the $T = 0$ phase diagram as a function of doping. Our results, shown in Fig. 8.8, are qualitatively similar to experiment. The calculations stabilize antiferromagnetism for low dopings $x < 0.05$, which gives way to a dome of d -wave superconductivity. The static order parameter $\Delta = \langle\langle c_1 c_2 \rangle\rangle_{\tau=0}$, where 1 and 2 are nearest neighbor sites on the impurity plaquette, reaches a maximum Δ_{max} near $x \sim 0.13$. We take the magnitude of Δ_{max} as a proxy for the maximum superconducting temperature $T_{\text{c,max}}$. The zero-frequency limit of the anomalous self-energy Σ^{an} is an additional indicator of superconductivity, which our results show qualitatively follows the magnitude of the order parameter.

We argue that although *two independent low-energy parameters* correlate with the experimental $T_{\text{c,max}}$, it is the charge-transfer energy that controls the variation in Δ_{max} , and thus $T_{\text{c,max}}$, across the cuprate families. To address this issue, we take the most correlated cuprate, LSCO, and compute Δ_{max} as we either (i) decrease $\epsilon_d - \epsilon_p$ or (ii) increase $t_{pp'}$. Fig. 8.9a shows that reducing the correlation strength for fixed $t_{pp'}$ enhances the order parameter Δ , in agreement with the empirical trend in Fig. 8.7a. However,

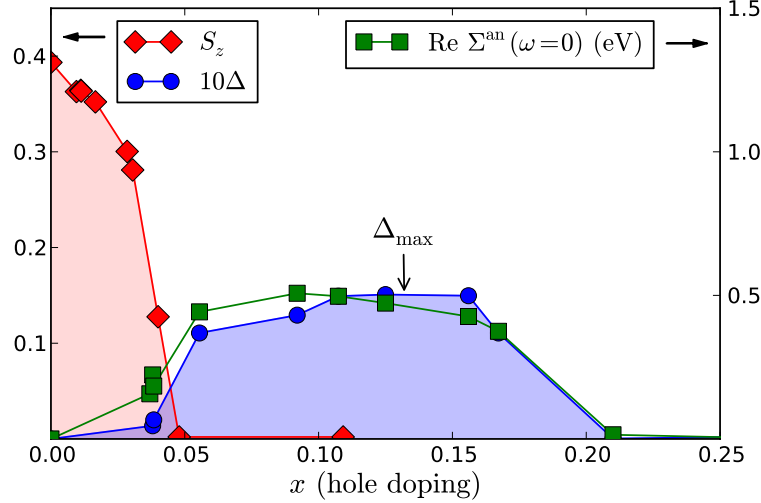


Figure 8.8: Calculated doping dependence for LSCO of the staggered magnetization $S^z = \frac{1}{2}(n_\uparrow - n_\downarrow)$ and static d -wave superconducting order parameter $\Delta \sim \langle cc \rangle_{\tau=0}$. We plot 10Δ to fit it on the same scale as S^z . Optimal superconducting strength Δ_{\max} is obtained for doping $x_{\text{opt}} \approx 0.13$. The real part of the anomalous self-energy $\text{Re} \Sigma^{\text{an}}(\omega=0)$ follows qualitatively the order parameter Δ . The calculations were performed at $T = 30$ K with c-DMFT and an ED impurity solver, using an 8-site discretization of the bath.

Fig. 8.9b shows that increasing $t_{pp'}$ across the physical parameter regime hardly modifies Δ_{\max} , in contrast with the empirical trend in Fig. 8.7b. Further increasing $t_{pp'}$ to larger, unphysical values strongly suppresses $T_{c,\max}$. Thus, our calculations support the hypothesis that a larger hopping range r suppresses $T_{c,\max}$, in agreement with calculations on the one-band [113, 114] and three-band [112] models.

The dependence of $T_{c,\max}$ on the two controlled parameters can be simply rationalized. For $\epsilon_d - \epsilon_p$, its large value in the strong correlation limit suppresses charge-fluctuations, rendering the residual superexchange interaction between the doped holes weak, resulting in low superconducting temperatures. As we decrease $\epsilon_d - \epsilon_p$, superconducting tendencies increase as we pass through the intermediate correlation regime, until we reach the weak correlation limit. Although the ground state of the 3-band model for large U_{dd} and $\epsilon_d - \epsilon_p \sim 0$ has not been rigorously established, we expect the large kinetic energy to suppress the effective interactions and thus superconductivity. Thus, we believe intermediate correlation strengths, a regime intimately related to the charge-transfer metal-to-insulator transition, is a crucial ingredient for cuprate superconductivity. Turning to $t_{pp'}$, we find that increasing this hopping amplitude lowers

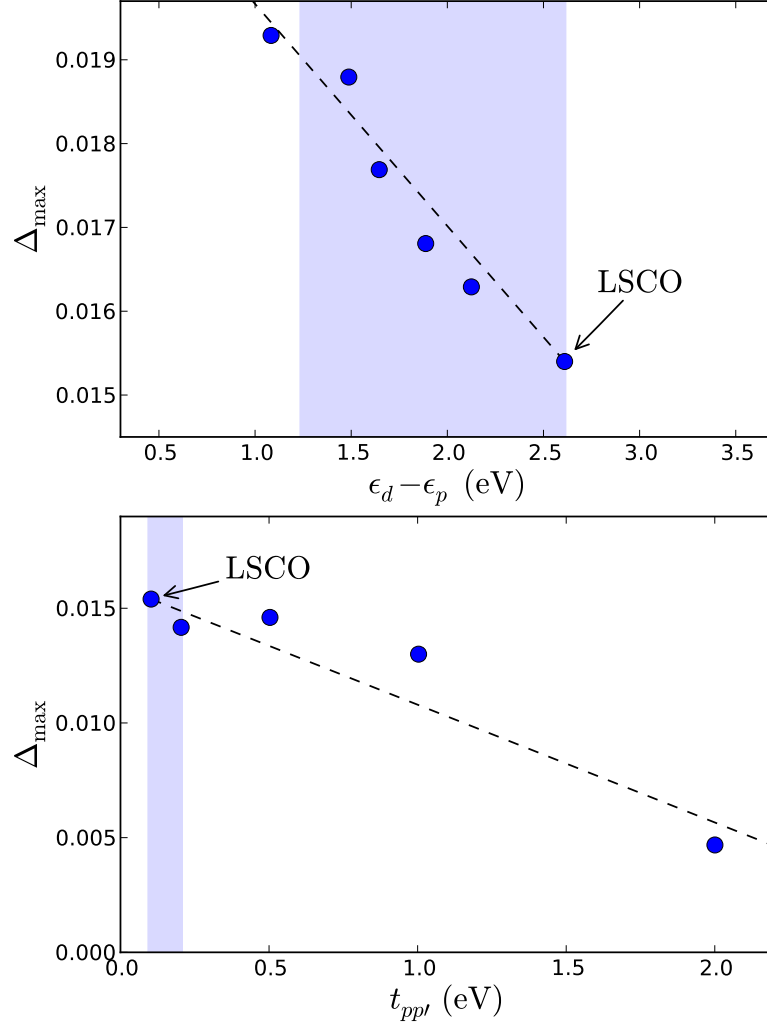


Figure 8.9: Optimal superconducting order parameter Δ_{\max} of LSCO as we (a) decrease the charge-transfer energy $\epsilon_d - \epsilon_p$ and (b) increase oxygen-oxygen hopping $t_{pp'}$. Shaded are the physical ranges spanned by the cuprate families.

the van Hove singularity at $(0, \pi)$ away from the Fermi level. The resulting decrease in density of states suppresses T_c , an effect which simple methods capture [119].

8.4 Summary

We have used electronic structure methods to identify the dependence of $T_{c,\max}$ on two fundamental parameters: the charge-transfer energy $\epsilon_d - \epsilon_p$ and inter-cell oxygen-oxygen hopping $t_{pp'}$. We find that the position of the apical oxygen tunes both parameters, but the strength of superconductivity, Δ_{\max} , is mainly sensitive to $\epsilon_d - \epsilon_p$. We expect future

refinements to explain the remaining variability in $T_{c,\text{max}}$. Our work provides a natural interpretation of experiments where epitaxial compression in LSCO resulted in a remarkable enhancement of T_c [120]. Epitaxy increases $d_{\text{Cu-O}}^{\text{apical}}$ and thus reduces $\epsilon_d - \epsilon_p$. Furthermore, our result provides microscopic insight into the multi-layer cuprates, such as Bi-2223: in addition to layer-dependent doping [121], the smaller value of the charge-transfer energy in the outer layers may explain the enhancement of superconductivity in the outer layers. It has been suggested theoretically and demonstrated experimentally [122] that proximity to a metallic layer reduces the charge-transfer energy. Using this principle in heterostructure design should result in even higher transition temperatures.

Chapter 9

Engineering the Charge-Transfer Energy in Cuprates

The work in Chapter 8 generated a clear direction for enhancing the superconducting transition temperatures of the cuprates: decrease the charge-transfer energy. In this chapter, we show that chemical substitution, combined with strain, allows the charge-transfer energy in hole-doped cuprates to be broadly tuned. We theoretically characterize the structural and electronic properties of the family of compounds $R_2\text{CuO}_2\text{S}_2$, constructed by sulfur replacement of the apical oxygens and rare earth substitutions in the parent cuprate La_2CuO_4 . Additionally, the enthalpies of formation for possible synthesis pathways are determined.

9.1 Introduction

In weakly correlated systems, analytic and computational tools, such as density functional theory (DFT), have achieved a level of control where one can reasonably contemplate materials design [123, 124]. The corresponding methods for strongly-correlated systems have not reached similar levels of accuracy. Nevertheless, materials design of correlated systems is still valuable as a tool to test our physical understanding and, should the materials be synthesized, provide experimental feedback to accelerate development of theoretical techniques.

The high-temperature cuprate superconductors have the highest transition temperatures known, but despite intense theoretical and experimental study, we have limited

first-principles understanding of the chemical parameters controlling these transition temperatures. Recently, based on a systematic *ab initio* study of the cuprates [125], we proposed that the charge-transfer energy $\epsilon_d - \epsilon_p$ controls the trends in the maximum superconducting transition temperature $T_{c,\max}$. Since the cuprates are charge-transfer materials, $\epsilon_d - \epsilon_p$ controls the strength of correlations. We found that starting with the most correlated cuprate La_2CuO_4 , decreasing the strength of correlations enhances $T_{c,\max}$. A differing conclusion was reached by Sakakibara, *et. al.*, who concluded that the reducing the mixture of the Cu d_{z^2} orbital with the in-plane $d_{x^2-y^2}$ orbital enhanced $T_{c,\max}$ [126, 127]. These studies pose a challenge for materials design to test their theoretical proposals.

In this work, we focus on our hypothesis regarding the charge-transfer energy and propose a family of hypothetical cuprate superconductors based on La_2CuO_2 to tune $\epsilon_d - \epsilon_p$. We show that chemical substitution of the apical oxygens by sulfur produces sufficiently large effects in $\epsilon_d - \epsilon_p$ to warrant careful study. We then examine the question of structure, performing necessary checks on the stability of the proposed compounds and related synthesis pathways.

9.2 Chemical Tuning of the Charge-Transfer Energy

We choose the T -type layered perovskite La_2CuO_4 (LCO) as our structural starting point. This single-layered cuprate is well-studied, supports a broad range of doping, and exhibits the largest charge-transfer energy of all the hole-doped cuprates. Guided by the intuition that the larger, more covalent, apical ions would decrease $\epsilon_d - \epsilon_p$, we replace the apical oxygens in LCO with sulfur to form the copper oxysulfide $\text{La}_2\text{CuO}_2\text{S}_2$. Due to the larger ionic radii of sulfur as compared to oxygen, we expect the LaS charge reservoir layers to be crowded. To compensate for this large sulfur in the charge reservoir layers, we explore the effect substitution of the large La ion with smaller trivalent ions $R = \text{Y, Lu, Sc, Ga}$. We structurally relax, within a single unit cell, the entire family of copper oxysulfides $R_2\text{CuO}_2\text{S}_2$. We used the VASP [128, 129, 130, 130] density functional software package with PAW potentials [131, 132]. Finally, we extract $\epsilon_d - \epsilon_p$ by performing a full-potential calculation on the relaxed structure using Wien2K [48],

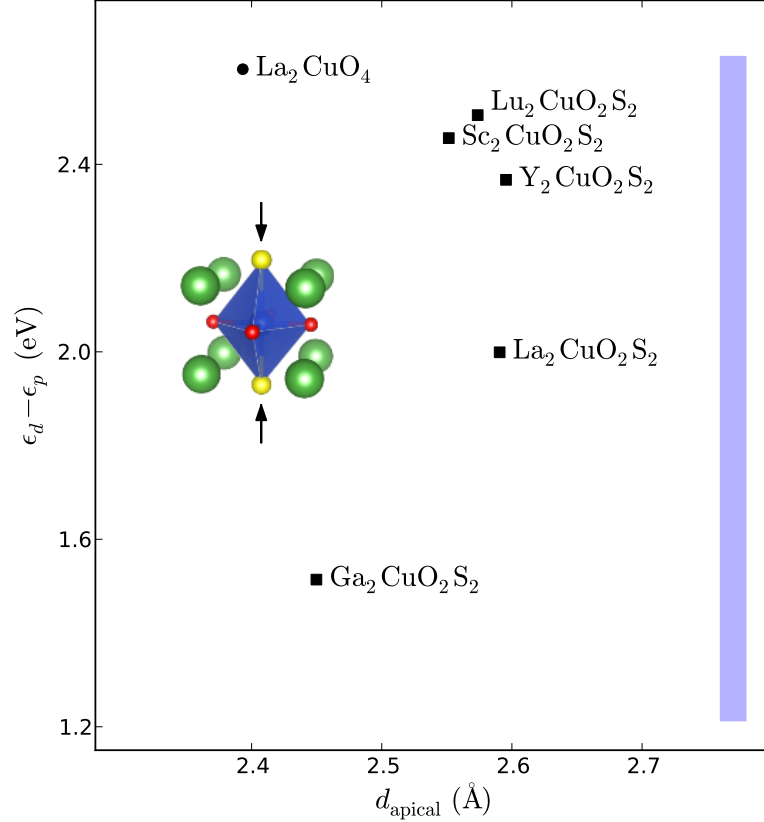


Figure 9.1: Plot of the charge-transfer energy ($\epsilon_d - \epsilon_p$) vs. the apical atom distance from the CuO_2 plane ($d_{\text{Cu-O}}^{\text{apical}}$) for the family of hypothetical copper oxysulfides $\text{R}_2\text{CuO}_2\text{S}_2$ (squares) and the parent compound La_2CuO_4 (circle). The oxysulfides are formed by the substitution of apical oxygens by sulfur (arrows in inset figure of crystal structure). Chemical substitution allows us to span nearly the entire range of charge-transfer energies (shaded bar) found in the cuprates.

then downfolding [115] to orbitals constructed in the manner described in Ref. [31].

The charge-transfer energies for the parent compound La_2CuO_4 and the family of hypothetical oxysulfides $\text{R}_2\text{CuO}_2\text{S}_2$ are shown in Fig. 9.1. The substitution of sulfur alone, leaving the La ion unmodified, decreases the charge-transfer energy by 0.6 eV, a significant reduction given that $\epsilon_d - \epsilon_p$ spans a range of 1.4 eV across all cuprate families. If no competing electronic or structural orders are introduced, we predict $\text{La}_2\text{CuO}_2\text{S}_2$ to have a higher superconducting transition temperature than LCO (which has a $T_{\text{c,max}}$ of 38 K). Further substitution of La by trivalent cations of varying ionic radii allows us to span nearly the entire range of charge-transfer energies found in the cuprates. Naïvely, the Ga analogue should have the highest $T_{\text{c,max}}$, since it has the smallest $\epsilon_d - \epsilon_p$. Additionally, we find that the apical atom distance $d_{\text{Cu-O}}^{\text{apical}}$ is increased

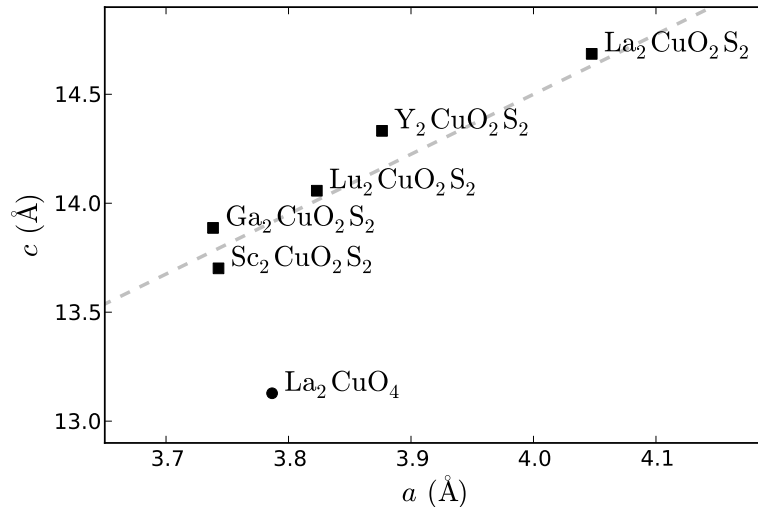


Figure 9.2: Fully relaxed conventional cell lattice parameters for $\text{R}_2\text{CuO}_2\text{S}_2$ family of compounds (squares) as compared to La_2CuO_4 (dot). Sulfur substitution increases both the a and c lattice parameters. The trend is accounted for by the decrease in ionic radii of the cation ($\text{La} \rightarrow \text{Y} \rightarrow \text{Lu} \rightarrow \text{Sc} \rightarrow \text{Ga}$), with La having the largest radius. The dotted line is a guide to the eye.

by as much as 0.2 Å in the oxysulfides, due to the large size of sulfur.

The structural effects of the sulfur and rare-earth substitutions can be rationalized entirely due to trends in ionic radii, as shown via a scatter plot of the a - and c -axis lattice constants of the proposed compounds (Fig. 9.2). The ionic radius of sulfur is greater than that of oxygen by 0.4 Å, a significant amount. Apical sulfur substitution alone enhances the c -axis length by over 1.5 Å relative to the parent compound LCO, in agreement with the fact that there are four sulfur layers in the conventional cell, giving $\Delta c \approx 4 \times 0.4$ Å. This chemically induced strain may be beneficial for superconductivity since it is known uniaxial compression strongly suppresses T_c in La_2CuO_4 [133], a point we will subsequently address. In contrast, the in-plane constant exhibits only a slight expansion by 0.2 Å, due to the restraining effect of the stiff Cu-O bonds. The subsequent rare-earth substitutions in the oxysulfides drive a clear structural trend, with both lattice parameters contracting in parallel with the decreasing ionic radius of the rare-earth ion R . The same trend is experimentally observed in the T' -type R_2CuO_4 family [134].

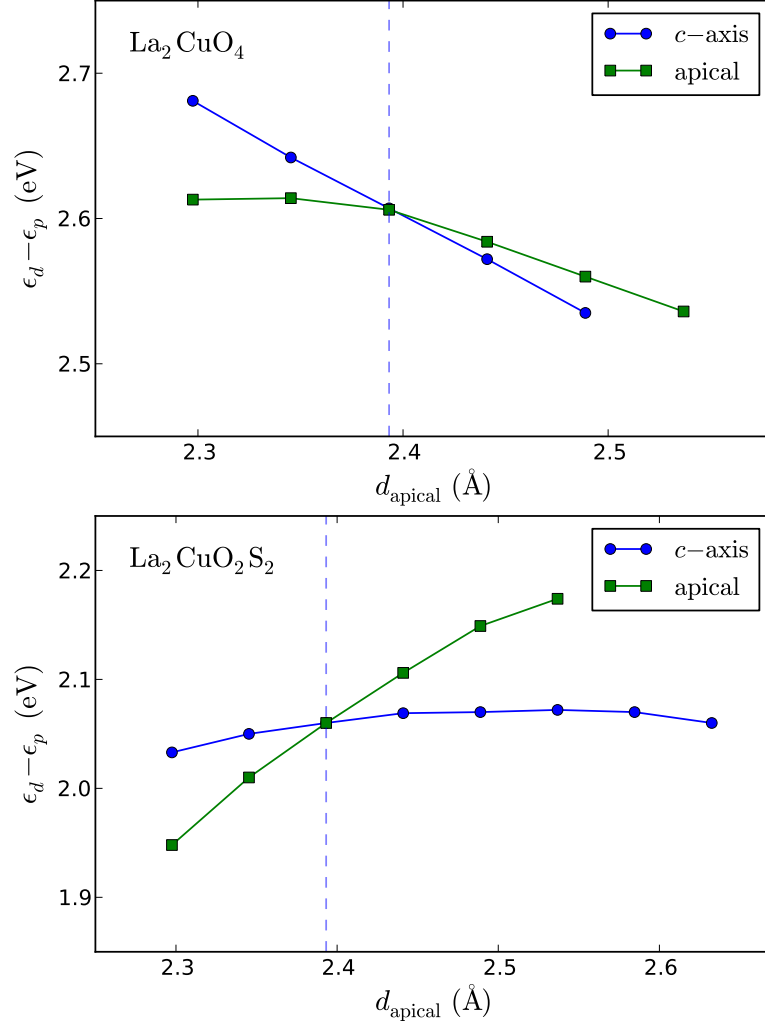


Figure 9.3: (top) Two structural modifications which tune the charge transfer energy of La_2CuO_4 : (dots) uniform c -axis strain, and (squares) tweaking only the apical oxygen position $d_{\text{Cu-O}}^{\text{apical}}$ with all other atoms held fixed. We place both curves on the same plot since uniform strain also changes the apical distance. The dotted line denotes the equilibrium $d_{\text{Cu-O}}^{\text{apical}}$. We find that $\epsilon_d - \epsilon_p$ decreases as the apical oxygen is pulled away from the CuO_2 plane. The effects due to the Madelung potential, as indicated by the difference between the two curves, is the same order of magnitude as crystal fields. Noting the vertical scale, pressure has a relatively small effect compared to chemical substitution. (bottom) The same plot for $\text{La}_2\text{CuO}_2\text{S}_2$. We find the opposite trend, that $\epsilon_d - \epsilon_p$ increases as the apical sulfur is pulled away from the CuO_2 plane.

In order to disentangle the structural contributions driving variations in the charge-transfer energy, we track the change in $\epsilon_d - \epsilon_p$ as we (1) vary the c -axis parameter, modeling uniform uniaxial strain and (2) vary $d_{\text{Cu-O}}^{\text{apical}}$ alone with all other atomic positions fixed. The difference in the resultant $\epsilon_d - \epsilon_p$ between these two structural configurations provides a rough proxy for the magnitude of effects due to the Madelung potential as compared to the local crystal fields generated in part by the apical atom. For the parent compound LCO (Fig. 9.3 top), c -axis compression enhances $\epsilon_d - \epsilon_p$. This increase in correlation strength provides a natural explanation for the observed suppression of superconductivity with uniaxial pressure [133]. Modifying $d_{\text{Cu-O}}^{\text{apical}}$ alone has a similar, albeit smaller, effect. The difference between the two curves is of the same magnitude as the total shifts in $\epsilon_d - \epsilon_p$, so we conclude that crystal fields and Madelung potentials have similar energy scales, making first-principles calculations necessary for quantitative insight. In comparison, strain has the opposite effect in the hypothetical compound $\text{La}_2\text{CuO}_2\text{S}_2$ (Fig. 9.3 bottom), with c -axis compression driving a reduction in $\epsilon_d - \epsilon_p$. Thus, $T_{\text{c,max}}$ should be observed to trend in the opposite direction as compared to the parent compound.

9.3 Structural and Thermodynamic Stability

Finally, we check the structural and thermodynamic stability of the hypothetical oxysulfides. Determining the lowest-energy structure of a general multi-element compound is extremely challenging, and the checks we perform are by no means exhaustive. However, guided by knowledge of typical competing phases and structural distortions, we show the $R_2\text{CuO}_2\text{S}_2$ family passes several basic criteria for stability.

In La_2CuO_4 , when the large La ion is replaced by the smaller Nd and Pr atoms, the oxygens in the rock-salt LaO layers in the T -type structure tend to be unstable towards rearrangement into the fluorite structure, forming the T' -type structure associated with the electron-doped cuprates [135]. We check whether our T -type oxysulfides are locally stable against distortion into the T' -type structure by performing a full structural relaxation in a $2 \times 2 \times 1$ supercell with no symmetry constraints. We choose $\text{Sc}_2\text{CuO}_2\text{S}_2$ as a representative compound, since we believe that the smaller Sc cation will help

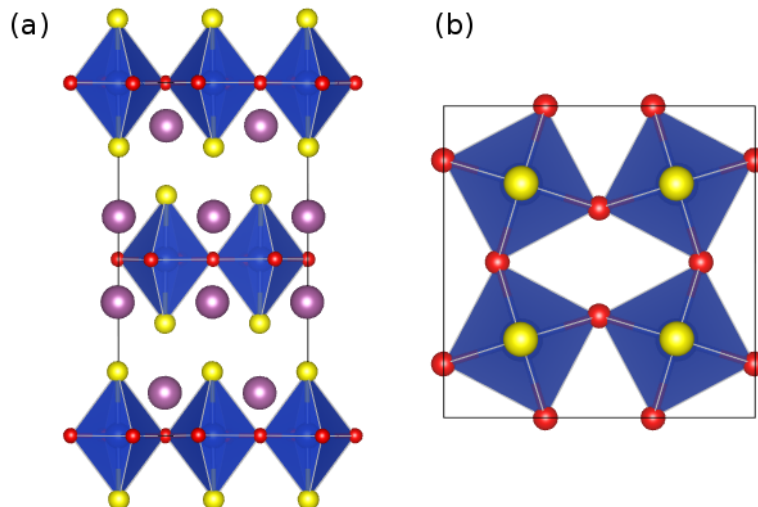


Figure 9.4: Octahedral rotations in $\text{Sc}_2\text{CuO}_2\text{S}_2$ as shown by (a) a view along the a -axis, and (b) a section of the CuO_2 plane. We structurally relaxed a $2 \times 2 \times 1$ supercell with no symmetry constraints. While there is no out-of-plane buckling of the Cu-O bonds, the small Sc ion causes strong in-plane rotations of the octahedral cages (denoted $a^0a^0c_p^-$ in Glazer notation). The compound remains in the tetragonal T -type phase.

create room for the large sulfur anion. The resultant structure (Fig. 9.4) shows strong octahedral rotations along the c -axis, denoted $a^0a^0c_p^-$ in Glazer notation [136]. Perovskite structures often exhibit octahedral rotations when the Goldschmidt tolerance factor $t = (r_A + r_O)/\sqrt{2}(r_B + r_O)$ is less than unity as the octahedra rotate to fill the empty space left by substitution of small rare-earth ions. However, we find the T -type structure to be locally stable and expect the rotations to be smaller in magnitude for the larger $R = \text{La}$ ion. Additionally, the system remains tetragonal and shows no out-of-plane buckling of the Cu-O bonds known to be detrimental to superconductivity [137]. We note that recent advances have allowed experimental control over the two competing structures in compound synthesis [134], which will help overcome these structural hurdles.

In addition to local structural stability, we check the thermodynamic stability of the proposed compounds with respect to competing phases. We assemble the computed internal energies of formation $\Delta E = E_{\text{products}} - E_{\text{reactants}}$ in Table 9.1 (units of kJ/mol). That the quantities are positive imply the that these standard pathways are not energetically favorable. However, it is known that many functional materials are

ΔE	ΔV	Synthesis pathway
141	-7.3	$\text{La}_2\text{O}_2\text{S} + \text{CuS} \rightarrow \text{La}_2\text{CuO}_2\text{S}_2$
223	-3.4	$\text{Y}_2\text{O}_2\text{S} + \text{CuS} \rightarrow \text{Y}_2\text{CuO}_2\text{S}_2$
267	-5.0	$\text{Lu}_2\text{O}_2\text{S} + \text{CuS} \rightarrow \text{Lu}_2\text{CuO}_2\text{S}_2$
356	-3.0	$\text{Sc}_2\text{O}_2\text{S} + \text{CuS} \rightarrow \text{Sc}_2\text{CuO}_2\text{S}_2$
101	-4.9	$\text{La}_2\text{O}_2\text{S}_2 + \text{Cu} \rightarrow \text{La}_2\text{CuO}_2\text{S}_2$
148	-3.3	$\text{La}_2\text{O}_3 + \text{CuS} \rightarrow \text{La}_2\text{CuO}_3\text{S}$
454	-0.7	$\text{Sc}_2\text{O}_3 + \text{CuS} \rightarrow \text{Sc}_2\text{CuO}_3\text{S}$
97	-4.9	$\text{La}_2\text{O}_2\text{S} + \text{CuO} \rightarrow \text{La}_2\text{CuO}_3\text{S}$
269	2.8	$\text{Sc}_2\text{O}_2\text{S} + \text{CuO} \rightarrow \text{Sc}_2\text{CuO}_3\text{S}$
28	-5.1	$\text{La}_2\text{O}_3 + \text{CuO} \rightarrow \text{La}_2\text{CuO}_4$

Table 9.1: Synthesis pathways for various cuprate oxysulfides based on substitution of sulfur for both (top block) or only one (middle block) of the apical oxygens in $R_2\text{CuO}_4$. Energies in kJ/mol and volumes in kJ/mol/GPa. Since the energies of formation ($\Delta E = E_{\text{products}} - E_{\text{reactants}}$) are positive, none of these pathways appear favorable at ambient conditions. However, high-pressure synthesis will help stabilize these pathways, since the majority of volume differentials ($\Delta V = V_{\text{products}} - V_{\text{reactants}}$) are negative. We benchmark our method against the standard synthesis pathway for La_2CuO_4 , shown on the last line. Surprisingly, ΔE is +28 kJ/mol, so either DFT systematically overestimates enthalpies (which means the actual enthalpies for our hypothetical compounds are *smaller*, in our favor), or we must add a bi-directional uncertainty of ± 30 kJ/mol to the computed enthalpies. Additionally, positional entropy of the apical S in the half-substituted $R_2\text{CuO}_3\text{S}$ compounds should also assist in synthesis.

metastable, protected from decay by large energetic barriers, resulting in technologically useful lifetimes [124]. Typical energetic deficits range from 5 to 30 kJ/mol, when translated to the oxysulfide compound stoichiometries. Accompanied by the fact that the volume differentials $\Delta V = V_{\text{products}} - V_{\text{reactants}}$ are negative, high pressure synthesis may allow the products to form. Furthermore, we included in Table 9.1 compounds of the form $R_2\text{CuO}_3\text{S}$, where only half of the apical oxygens are replaced by sulfur. The configurational entropy of the sulfur-oxygen arrangement in the charge-reservoir blocks will further encourage product formation.

9.4 Summary

We have identified chemical handles which allow us to broadly tune the charge-transfer energy in the hypothetical $R_2\text{CuO}_2\text{S}_2$ family of copper oxysulfides. If the systems are synthesized, this broad tunability allows us to test our hypothesis regarding the correlation between the charge-transfer energy and the maximum superconducting transition temperatures. Natural extensions of our work include testing for competing T' -type

phases, like those found in the electron-doped cuprates. Additionally, similar substitutions could be pursued in the Bi, Tl and Hg-based cuprates.

Chapter 10

Conclusion

In this thesis, we have discussed the DFT+DMFT framework, through which we have pursued an *ab initio* understanding of strongly-correlated materials. These theoretical techniques are under active development, and we hope that in the near future, they will reach the level of stability and predictive power of DFT. We believe that the modeling of strongly-correlated materials, as well as rational design of new compounds, is a fruitful direction of research. Additionally, the increase in computational power has begun to allow large-scale scans of materials phase space, providing a complementary, global view of materials.

In the vein of research outline in this thesis, there are natural open questions in both method development and applications. The algorithms presented for entropy should be generalized for arbitrary interactions and extended to lattice systems. The pursuit of truly *ab initio* determination of the interaction parameters U and J remain an open problem. In the cuprates, the presence of disorder, constraints on doping, and structural stability introduce uncontrolled variables. Computation of the superconducting order parameter within a first-principles framework would help clarify the trends we have observed in the charge-transfer energy. Additionally, molecular beam epitaxy allows the synthesis of novel compounds with extreme precision. Juxtaposing the copper-oxygen planes in the cuprates with other structural motifs may lead to new insights into the mechanism of superconductivity.

Bibliography

- [1] E. Pavarini, I. Dasgupta, T. Saha-Dasgupta, O. Jepsen, and O. K. Andersen. Band-structure trend in hole-doped cuprates and correlation with t_{max} . *Phys. Rev. Lett.*, 87(4):047003, Jul 2001.
- [2] David Young. *Phase Diagram of the Elements*. National Technical Information Service, Sep 1975.
- [3] G. Keller, K. Held, V. Eyert, D. Vollhardt, and V. I. Anisimov. Electronic structure of paramagnetic v_2O_3 : Strongly correlated metallic and mott insulating phase. *Phys. Rev. B*, 70:205116, Nov 2004.
- [4] D. B. McWhan, A. Menth, J. P. Remeika, W. F. Brinkman, and T. M. Rice. Metal-insulator transitions in pure and doped v_2O_3 . *Phys. Rev. B*, 7:1920–1931, Mar 1973.
- [5] Siegfried S. Hecker. Plutonium and its alloys: From atoms to microstructure. *Los Alamos Science*, 2(26):290–335, 2000.
- [6] A. Blaise, J. M. Collard, J. M. Fournier, J. Rebizant, J. C. Spirlet, and O. Vogt. Electrical resistivity of v_2O_3 single crystals. *Physica B+C*, 130(1-3):99 – 101, 1985.
- [7] V. Ichas, J. C. Griveau, J. Rebizant, and J. C. Spirlet. High-pressure resistance of v_2O_3 up to 25 gpa. *Phys. Rev. B*, 63(4):045109, Jan 2001.
- [8] T. Durakiewicz, J. J. Joyce, G. H. Lander, C. G. Olson, M. T. Butterfield, E. Guziewicz, A. J. Arko, L. Morales, J. Rebizant, K. Mattenberger, and O. Vogt.

- Electronic structure of actinide antimonides and tellurides from photoelectron spectroscopy. *Phys. Rev. B*, 70(20):205103, Nov 2004.
- [9] J. B. Torrance, P. Lacorre, A. I. Nazzari, E. J. Ansaldo, and Ch. Niedermayer. Systematic study of insulator-metal transitions in perovskites RnO_3 ($r = \text{pr, nd, sm, eu}$) due to closing of charge-transfer gap. *Phys. Rev. B*, 45:8209–8212, Apr 1992.
- [10] K. Sreedhar, J. M. Honig, M. Darwin, M. McElfresh, P. M. Shand, J. Xu, B. C. Crooker, and J. Spalek. Electronic properties of the metallic perovskite LaNiO_3 : Correlated behavior of $3d$ electrons. *Phys. Rev. B*, 46:6382–6386, Sep 1992.
- [11] M. K. Stewart, Jian Liu, R. K. Smith, B. C. Chapler, C.-H. Yee, R. E. Baumbach, M. B. Maple, K. Haule, J. Chakhalian, and D. N. Basov. Optical probe of strong correlations in LaNiO_3 thin films. *Journal of Applied Physics*, 110(3):033514, 2011.
- [12] M. K. Stewart, C.-H. Yee, Jian Liu, M. Kareev, R. K. Smith, B. C. Chapler, M. Varela, P. J. Ryan, K. Haule, J. Chakhalian, and D. N. Basov. Optical study of strained ultrathin films of strongly correlated LaNiO_3 . *Phys. Rev. B*, 83:075125, Feb 2011.
- [13] Hiroyuki Shibata. Superconducting single-photon detectors. *NTT Technical Review*, 9(9), Sep 2011.
- [14] Patrik Fazekas. *Lecture Notes on Electron Correlation and Magnetism*. World Scientific, 1999.
- [15] D C Peets, J D F Mottershead, B Wu, I S Elfimov, Ruixing Liang, W N Hardy, D A Bonn, M Raudsepp, N J C Ingle, and A Damascelli. $\text{Ti}_2\text{Ba}_2\text{CuO}_6+\delta$ brings spectroscopic probes deep into the overdoped regime of the high- T_c cuprates. *New Journal of Physics*, 9(2):28, 2007.
- [16] Xu Du, Ivan Skachko, Fabian Duerr, Adina Luican, and Eva Andrei. Fractional

- quantum hall effect and insulating phase of dirac electrons in graphene. *Nature*, 462(7270):192–195, Nov 2009.
- [17] Kirill Bolotin, Fereshte Ghahari, Michael Shulman, Horst Stormer, and Philip Kim. Observation of the fractional quantum hall effect in graphene. *Nature*, 462(7270):196–199, Nov 2009.
- [18] P. Limelette, A. Georges, D. Jrome, P. Wzietek, P. Metcalf, and J. M. Honig. Universality and critical behavior at the mott transition. *Science*, 302(5642):89–92, 2003.
- [19] Walter Metzner and Dieter Vollhardt. Correlated lattice fermions in $d = \infty$ dimensions. *Phys. Rev. Lett.*, 62:324–327, Jan 1989.
- [20] Antoine Georges and Gabriel Kotliar. Hubbard model in infinite dimensions. *Phys. Rev. B*, 45:6479–6483, Mar 1992.
- [21] G. Kotliar, S. Y. Savrasov, K. Haule, V. S. Oudovenko, O. Parcollet, and C. A. Marianetti. Electronic structure calculations with dynamical mean-field theory. *Rev. Mod. Phys.*, 78(3):865, 2006.
- [22] M. J. Rozenberg, G. Kotliar, H. Kajueter, G. A. Thomas, D. H. Rapkine, J. M. Honig, and P. Metcalf. Optical conductivity in mott-hubbard systems. *Phys. Rev. Lett.*, 75:105–108, Jul 1995.
- [23] P. Hohenberg and W. Kohn. Inhomogeneous electron gas. *Phys. Rev.*, 136:B864–B871, Nov 1964.
- [24] W. Kohn and L. J. Sham. Self-consistent equations including exchange and correlation effects. *Phys. Rev.*, 140:A1133–A1138, Nov 1965.
- [25] Gabriel Kotliar and Dieter Vollhardt. Strongly correlated materials: Insights from dynamical mean-field theory. *Physics Today*, 57(3):53–59, 2004.
- [26] K. Held. Electronic structure calculations using dynamical mean field theory. *Advances in Physics*, 56:829, 2007.

- [27] A. Georges, Gabriel Kotliar, Werner Krauth, and Marcelo J. Rozenberg. 1996. *Rev. Mod. Phys.*, 68:13, 1996.
- [28] Antoine Georges. Strongly correlated electron materials: Dynamical mean-field theory and electronic structure. *AIP Conference Proceedings*, 715(1):3–74, 2004.
- [29] Thomas Maier, Mark Jarrell, Thomas Pruschke, and Matthias H. Hettler. Quantum cluster theories. *Rev. Mod. Phys.*, 77(3):1027–1080, Oct 2005.
- [30] J. Hubbard. Electron correlations in narrow energy bands. iii. an improved solution. *Proceedings of the Royal Society of London. Series A. Mathematical and Physical Sciences*, 281(1386):401–419, 1964.
- [31] Cyrano De Dominicis and Paul C. Martin. Stationary entropy principle and renormalization in normal and superfluid systems. i. algebraic formulation. *Journal of Mathematical Physics*, 5(1):14–30, 1964.
- [32] Cyrano De Dominicis and Paul C. Martin. Stationary entropy principle and renormalization in normal and superfluid systems. ii. diagrammatic formulation. *Journal of Mathematical Physics*, 5(1):31–59, 1964.
- [33] N. Andrei, K. Furuya, and J. H. Lowenstein. Solution of the kondo problem. *Rev. Mod. Phys.*, 55:331–402, Apr 1983.
- [34] Piers Coleman. New approach to the mixed-valence problem. *Phys. Rev. B*, 29(6):3035–3044, Mar 1984.
- [35] N. E. Bickers, D. L. Cox, and J. W. Wilkins. Self-consistent large- n expansion for normal-state properties of dilute magnetic alloys. *Phys. Rev. B*, 36(4):2036–2079, Aug 1987.
- [36] J. Kroha, S. Kirchner, G. Sellier, P. Wölfle, D. Ehm, F. Reinert, S. Hufner, and C. Geibel. Structure and transport in multi-orbital kondo systems. *Physica E: Low-dimensional Systems and Nanostructures*, 18(1-3):69 – 72, 2003. 23rd International Conference on Low Temperature Physics (LT23).

- [37] J. E. Hirsch and R. M. Fye. Monte carlo method for magnetic impurities in metals. *Phys. Rev. Lett.*, 56:2521–2524, Jun 1986.
- [38] A. N. Rubtsov, V. V. Savkin, and A. I. Lichtenstein. Continuous-time quantum monte carlo method for fermions. *Phys. Rev. B*, 72:035122, Jul 2005.
- [39] Philipp Werner, Armin Comanac, Luca de’ Medici, Matthias Troyer, and Andrew J. Millis. Continuous-time solver for quantum impurity models. *Phys. Rev. Lett.*, 97:076405, Aug 2006.
- [40] Kristjan Haule. Quantum monte carlo impurity solver for cluster dynamical mean-field theory and electronic structure calculations with adjustable cluster base. *Phys. Rev. B*, 75:155113, Apr 2007.
- [41] Philipp Werner and Andrew J. Millis. Hybridization expansion impurity solver: General formulation and application to kondo lattice and two-orbital models. *Phys. Rev. B*, 74:155107, Oct 2006.
- [42] Emanuel Gull, Andrew J. Millis, Alexander I. Lichtenstein, Alexey N. Rubtsov, Matthias Troyer, and Philipp Werner. Continuous-time monte carlo methods for quantum impurity models. *Rev. Mod. Phys.*, 83:349–404, May 2011.
- [43] Kristjan Haule, Chuck-Hou Yee, and Kyoo Kim. Dynamical mean-field theory within the full-potential methods: Electronic structure of *ceirin5*, *cecoin5*, and *cerhin5*. *Phys. Rev. B*, 81(19):195107, May 2010.
- [44] D. M. Ceperley and B. J. Alder. Ground state of the electron gas by a stochastic method. *Phys. Rev. Lett.*, 45:566–569, Aug 1980.
- [45] D. R. Hamann, M. Schlüter, and C. Chiang. Norm-conserving pseudopotentials. *Phys. Rev. Lett.*, 43:1494–1497, Nov 1979.
- [46] D. Vanderbilt. Soft self-consistent pseudopotentials in a generalized eigenvalue formalism. *Phys. Rev. B*, 41:7892, 1990.
- [47] D. J. Singh and L. Nordstrom, editors. *Planewaves, Pseudopotentials, and the LAPW Method*. Springer, New York, 2006.

- [48] F. Aryasetiawan, K. Karlsson, O. Jepsen, and U. Schönberger. Calculations of hubbard u from first-principles. *Phys. Rev. B*, 74:125106, Sep 2006.
- [49] F. Aryasetiawan, M. Imada, A. Georges, G. Kotliar, S. Biermann, and A. I. Lichtenstein. Frequency-dependent local interactions and low-energy effective models from electronic structure calculations. *Phys. Rev. B*, 70:195104, Nov 2004.
- [50] A. Kutepov, K. Haule, S. Y. Savrasov, and G. Kotliar. Self-consistent gw determination of the interaction strength: Application to the iron arsenide superconductors. *Phys. Rev. B*, 82:045105, Jul 2010.
- [51] V I Anisimov, A I Poteryaev, M A Korotin, A O Anokhin, and G Kotliar. First-principles calculations of the electronic structure and spectra of strongly correlated systems: dynamical mean-field theory. *Journal of Physics: Condensed Matter*, 9(35):7359, 1997.
- [52] A. I. Lichtenstein and M. I. Katsnelson. Ab initio calculations of quasiparticle band structure in correlated systems: Lda++ approach. *Phys. Rev. B*, 57:6884–6895, Mar 1998.
- [53] S. Y. Savrasov and G. Kotliar. Spectral density functionals for electronic structure calculations. *Phys. Rev. B*, 69:245101, Jun 2004.
- [54] E. Pavarini, S. Biermann, A. Poteryaev, A. I. Lichtenstein, A. Georges, and O. K. Andersen. Mott transition and suppression of orbital fluctuations in orthorhombic $3d^1$ perovskites. *Phys. Rev. Lett.*, 92:176403, Apr 2004.
- [55] L. V. Pourovskii, B. Amadon, S. Biermann, and A. Georges. Self-consistency over the charge density in dynamical mean-field theory: A linear muffin-tin implementation and some physical implications. *Phys. Rev. B*, 76:235101, Dec 2007.
- [56] B. Amadon, F. Lechermann, A. Georges, F. Jollet, T. O. Wehling, and A. I. Lichtenstein. Plane-wave based electronic structure calculations for correlated materials using dynamical mean-field theory and projected local orbitals. *Phys. Rev. B*, 77:205112, May 2008.

- [57] Dm. Korotin, A. Kozhevnikov, S. Skornyakov, I. Leonov, N. Binggeli, V. Anisimov, and G. Trimarchi. Construction and solution of a wannier-functions based hamiltonian in the pseudopotential plane-wave framework for strongly correlated materials. *The European Physical Journal B - Condensed Matter and Complex Systems*, 65:91–98, 2008. 10.1140/epjb/e2008-00326-3.
- [58] Nicola Marzari and David Vanderbilt. Maximally localized generalized wannier functions for composite energy bands. *Phys. Rev. B*, 56:12847–12865, Nov 1997.
- [59] P. Novak. *Program QTL - technical report*. Institute of Physics of ASCR, Cukrovarnicka 10, 162 53 Prague 6, Czech Republic, Apr 2008.
- [60] P. Blaha, K. Schwarz, G. K. H. Madsen, D. Kvasnicka, and J. Luitz. *WIEN2K, An Augmented Plane Wave + Local Orbitals Program for Calculating Crystal Properties*. Karlheinz Schwarz, Techn. Universität Wien, Austria, 2001.
- [61] A. B. Shick, A. I. Liechtenstein, and W. E. Pickett. Implementation of the lda+u method using the full-potential linearized augmented plane-wave basis. *Phys. Rev. B*, 60:10763–10769, Oct 1999.
- [62] A. B. Shick, J. Kolorenč, A. I. Lichtenstein, and L. Havela. Electronic structure and spectral properties of am, cm, and bk: Charge-density self-consistent LDA + HIA calculations in the fp-lapw basis. *Phys. Rev. B*, 80:085106, Aug 2009.
- [63] P. W. Anderson. Localized magnetic states in metals. *Phys. Rev.*, 124:41–53, Oct 1961.
- [64] Jun Kondo. Resistance minimum in dilute magnetic alloys. *Progress of Theoretical Physics*, 32(1):37–49, 1964.
- [65] P. W. Anderson and G. Yuval. Exact results in the kondo problem: Equivalence to a classical one-dimensional coulomb gas. *Phys. Rev. Lett.*, 23:89–92, Jul 1969.
- [66] P W Anderson. A poor man’s derivation of scaling laws for the kondo problem. *Journal of Physics C: Solid State Physics*, 3(12):2436, 1970.

- [67] Kenneth G. Wilson. The renormalization group: Critical phenomena and the kondo problem. *Rev. Mod. Phys.*, 47:773–840, Oct 1975.
- [68] David P. Landau and Kurt Binder. *A Guide to Monte Carlo Simulations in Statistical Physics*. Cambridge University Press, Oct 2009.
- [69] Andreas M. Läuchli and Philipp Werner. Krylov implementation of the hybridization expansion impurity solver and application to 5-orbital models. *Phys. Rev. B*, 80:235117, Dec 2009.
- [70] Brigitte Surer, Matthias Troyer, Philipp Werner, Tim O. Wehling, Andreas M. Läuchli, Aljoscha Wilhelm, and Alexander I. Lichtenstein. Multiorbital kondo physics of co in cu hosts. *Phys. Rev. B*, 85:085114, Feb 2012.
- [71] Necia Grant Cooper, editor. *Challenges in Plutonium Science*. Number 26 in 1. Los Alamos National Laboratory, 2006.
- [72] Chuck-Hou Yee, Gabriel Kotliar, and Kristjan Haule. Valence fluctuations and quasiparticle multiplets in plutonium chalcogenides and pnictides. *Phys. Rev. B*, 81:035105, Jan 2010.
- [73] G. H. Lander, J. Rebizant, J. C. Spirlet, A. Delapalme, P. J. Brown, O. Vogt, and K. Mattenberger. Neutron scattering and magnetization studies of plutonium monochalcogenides. *Physica B+C*, 146(3):341 – 350, 1987.
- [74] G.R. Stewart, R.G. Haire, J.C. Spirlet, and J. Rebizant. Specific heats of npte and pute. *Journal of Alloys and Compounds*, 177(1):167 – 171, 1991.
- [75] P. G. Therond, A. Blaise, J. M. Fournier, J. Rossat-Mignod, J. C. Spirlet, J. Rebizant, and O. Vogt. Transport properties of the pusb1-xtex solid solution. *J. Magn. Magn. Mat.*, 63-64:142 – 144, 1987.
- [76] J.M. Fournier, E. Pleska, J. Chiapusio, J. Rossat-Mignod, J. Rebizant, J.C. Spirlet, and O. Vogt. Electrical resistivity of plutonium monochalcogenides. *Physica B: Condensed Matter*, 163(1-3):493 – 495, 1990.

- [77] T. Gouder, F. Wastin, J. Rebizant, and L. Havela. $5f$ -electron localization in pure and pure. *Phys. Rev. Lett.*, 84(15):3378–3381, Apr 2000.
- [78] L. Havela, T. Gouder, F. Wastin, and J. Rebizant. Photoelectron spectroscopy study of the $5f$ localization in pure. *Phys. Rev. B*, 65(23):235118, Jun 2002.
- [79] P. Wachter. Intermediate valence of plutonium chalcogenides as determined by photoemission. *Solid State Communications*, 127(9-10):599 – 603, 2003.
- [80] P. M. Oppeneer, T. Kraft, and M. S. S. Brooks. Electronic structure of plutonium monochalcogenides. *Phys. Rev. B*, 61(19):12825–12834, May 2000.
- [81] A. O. Shorikov, A. V. Lukoyanov, M. A. Korotin, and V. I. Anisimov. Magnetic state and electronic structure of the δ and α phases of metallic pure and its compounds. *Phys. Rev. B*, 72(2):024458, Jul 2005.
- [82] L. V. Pourovskii, M. I. Katsnelson, and A. I. Lichtenstein. Correlation effects in electronic structure of actinide monochalcogenides. *Phys. Rev. B*, 72(11):115106, Sep 2005.
- [83] M.-T. Suzuki and P. M. Oppeneer. Dynamical mean-field theory of a correlated gap formation in plutonium monochalcogenides. *Physical Review B (Condensed Matter and Materials Physics)*, 80(16):161103, 2009.
- [84] A. Svane. Dynamical mean-field theory of photoemission spectra of actinide compounds. *Solid State Communications*, 140(7-8):364 – 368, 2006.
- [85] A. Shick, J. Koloren, L. Havela, V. Drchal, and T. Gouder. Multiplet effects in the electronic structure of δ -pure, am and their compounds. *Europhysics Letters*, 77(1):17003, jan 2007.
- [86] K. Haule, S. Kirchner, J. Kroha, and P. Wölfle. Anderson impurity model at finite coulomb interaction u: Generalized noncrossing approximation. *Phys. Rev. B*, 64(15):155111, Sep 2001.

- [87] A. Toropova, C. A. Marianetti, K. Haule, and G. Kotliar. One-electron physics of the actinides. *Physical Review B (Condensed Matter and Materials Physics)*, 76(15):155126, 2007.
- [88] S. Y. Savrasov, G. Kotliar, and E. Abrahams. Correlated electrons in $[\delta]$ -plutonium within a dynamical mean-field picture. *Nature*, 410:793, 4 2001.
- [89] Jian-Xin Zhu, A. K. McMahan, M. D. Jones, T. Durakiewicz, J. J. Joyce, J. M. Wills, and R. C. Albers. Spectral properties of delta-plutonium: Sensitivity to 5f occupancy. *Physical Review B (Condensed Matter and Materials Physics)*, 76(24):245118, 2007.
- [90] J. H. Shim, K. Haule, and G. Kotliar. Fluctuating valence in a correlated solid and the anomalous properties of $[\delta]$ -plutonium. *Nature*, 446:513, 03 2007.
- [91] R. D. Cowan. *The Theory of Atomic Structure and Spectra*. Univ. California Press, Berkeley, 1981.
- [92] Gabriel Kotliar and Andrei E. Ruckenstein. New functional integral approach to strongly correlated fermi systems: The gutzwiller approximation as a saddle point. *Phys. Rev. Lett.*, 57(11):1362–1365, Sep 1986.
- [93] V. M. Goldschmidt. Die gesetze der krystallochemie. *Naturwissenschaften*, 14:477–485, 1926. 10.1007/BF01507527.
- [94] J. Zaanen, G. A. Sawatzky, and J. W. Allen. 1985. *Phys. Rev. Lett.*, 55:418, 1985.
- [95] Jiří Chaloupka and Giniyat Khaliullin. Orbital order and possible superconductivity in $\text{LaNiO}_3/\text{LaMO}_3$ superlattices. *Phys. Rev. Lett.*, 100:016404, Jan 2008.
- [96] P. Hansmann, Xiaoping Yang, A. Toschi, G. Khaliullin, O. K. Andersen, and K. Held. Turning a nickelate fermi surface into a cupratelike one through heterostructuring. *Phys. Rev. Lett.*, 103:016401, Jun 2009.
- [97] J. L. Garc´ıa-Muñoz, J. Rodr´ıguez-Carvajal, P. Lacorre, and J. B. Torrance. Neutron-diffraction study of RNiO_3 ($R=\text{La, Pr, Nd, Sm}$): Electronically induced structural

- changes across the metal-insulator transition. *Phys. Rev. B*, 46:4414–4425, Aug 1992.
- [98] S. J. May, J.-W. Kim, J. M. Rondinelli, E. Karapetrova, N. A. Spaldin, A. Bhattacharya, and P. J. Ryan. Quantifying octahedral rotations in strained perovskite oxide films. *Phys. Rev. B*, 82:014110, Jul 2010.
- [99] R. Eguchi, A. Chainani, M. Taguchi, M. Matsunami, Y. Ishida, K. Horiba, Y. Senba, H. Ohashi, and S. Shin. Fermi surfaces, electron-hole asymmetry, and correlation kink in a three-dimensional fermi liquid LaNiO_3 . *Phys. Rev. B*, 79:115122, Mar 2009.
- [100] K.P. Rajeev, G.V. Shivashankar, and A.K. Raychaudhuri. Low-temperature electronic properties of a normal conducting perovskite oxide (LaNiO_3). *Solid State Communications*, 79(7):591 – 595, 1991.
- [101] J. Bardeen, L. N. Cooper, and J. R. Schrieffer. Microscopic theory of superconductivity. *Phys. Rev.*, 106:162–164, Apr 1957.
- [102] J. G. Bednorz and K. A. Müller. Possible high- T_c superconductivity in the BaCuO_2 system. *Zeitschrift für Physik B Condensed Matter*, 64:189–193, 1986. 10.1007/BF01303701.
- [103] Y. Ohta, T. Tohyama, and S. Maekawa. Apex oxygen and critical temperature in copper oxide superconductors: Universal correlation with the stability of local singlets. *Phys. Rev. B*, 43(4):2968–2982, Feb 1991.
- [104] Wei-Guo Yin and Wei Ku. Tuning the in-plane electron behavior in high- T_c cuprate superconductors via apical atoms: A first-principles wannier-states analysis. *Phys. Rev. B*, 79(21):214512, Jun 2009.
- [105] G. Kotliar, S. Y. Savrasov, K. Haule, V. S. Oudovenko, O. Parcollet, and C. A. Marianetti. 2006. *Rev. Mod. Phys.*, 78:865, 2006.

- [106] Emanuel Gull, Olivier Parcollet, Philipp Werner, and Andrew J. Millis. Momentum sector-selective metal-insulator transition in the eight-site dynamical mean-field approximation to the hubbard model in two dimensions. *Phys. Rev. B*, 80(24):245102, Dec 2009.
- [107] Kristjan Haule and Gabriel Kotliar. Strongly correlated superconductivity: A plaquette dynamical mean-field theory study. *Phys. Rev. B*, 76(10):104509, Sep 2007.
- [108] A. Comanac, L. de' Medici, M. Capone, and A. J. Millis. 2008. *Nature Physics*, 4:287, 2008.
- [109] David Sénéchal and A.-M. S. Tremblay. Hot spots and pseudogaps for hole- and electron-doped high-temperature superconductors. *Phys. Rev. Lett.*, 92:126401, Mar 2004.
- [110] Cedric Weber, Kristjan Haule, and Gabriel Kotliar. Strength of correlations in electron and hole doped cuprates. *Nature Physics*, 6:574 – 578, 2010.
- [111] Xin Wang, Emanuel Gull, Luca de' Medici, Massimo Capone, and Andrew J. Millis. Antiferromagnetism and the gap of a mott insulator: Results from analytic continuation of the self-energy. *Phys. Rev. B*, 80(4):045101, Jul 2009.
- [112] P. R. C. Kent, T. Saha-Dasgupta, O. Jepsen, O. K. Andersen, A. Macridin, T. A. Maier, M. Jarrell, and T. C. Schulthess. Combined density functional and dynamical cluster quantum monte carlo calculations of the three-band hubbard model for hole-doped cuprate superconductors. *Phys. Rev. B*, 78(3):035132, Jul 2008.
- [113] S. S. Kancharla, B. Kyung, D. Sénéchal, M. Civelli, M. Capone, G. Kotliar, and A.-M. S. Tremblay. Anomalous superconductivity and its competition with antiferromagnetism in doped mott insulators. *Phys. Rev. B*, 77(18):184516, May 2008.

- [114] Th. Maier, M. Jarrell, Th. Pruschke, and J. Keller. d -wave superconductivity in the hubbard model. *Phys. Rev. Lett.*, 85(7):1524–1527, Aug 2000.
- [115] Ivo Souza, Nicola Marzari, and David Vanderbilt. Maximally localized wannier functions for entangled energy bands. *Phys. Rev. B*, 65:035109, Dec 2001.
- [116] G. Kotliar. Strong correlation transport and coherence. *Int. J. Mod. Phys. B*, 5:341, 1991.
- [117] Michel Caffarel and Werner Krauth. Exact diagonalization approach to correlated fermions in infinite dimensions: Mott transition and superconductivity. *Phys. Rev. Lett.*, 72(10):1545–1548, Mar 1994.
- [118] M. Civelli. The doping-driven evolution of the superconducting state of a doped mott insulator: a key for the high temperature superconductivity. *Phys. Rev. B*, 79:195113, 2009.
- [119] Gabriel Kotliar and Jialin Liu. Superexchange mechanism and d-wave superconductivity. *Phys. Rev. B*, 38(7):5142, 1988.
- [120] J.-P. Locquet, J. Perret, J. Fompeyrine, E. Mchler, J. W. Seo, and G. Van Tendeloo. Doubling the critical temperature of $\text{La}_{1.9}\text{Sr}_{0.1}\text{CuO}_4$ using epitaxial strain. *Nature*, 394:453–456, Jul 1998.
- [121] A. Trokiner, L. Le Noc, J. Schneck, A. M. Pougnet, R. Mellet, J. Primot, H. Savary, Y. M. Gao, and S. Aubry. ^{67}Zn nuclear-magnetic-resonance evidence for distinct carrier densities in the two types of CuO_2 planes of $(\text{Bi,Pb})_2\text{Sr}_2\text{Ca}_2\text{Cu}_3\text{O}_{10}$. *Phys. Rev. B*, 44(5):2426–2429, Aug 1991.
- [122] S. Altieri, L. H. Tjeng, F. C. Voogt, T. Hibma, and G. A. Sawatzky. Reduction of coulomb and charge-transfer energies in oxide films on metals. *Phys. Rev. B*, 59(4):R2517–R2520, Jan 1999.
- [123] Jrgen Hafner, Christopher Wolverton, and Gerbrand Ceder. Toward computational materials design: The impact of density functional theory on materials research. *MRS Bulletin*, 31:659–668, 2006.

- [124] Xiuwen Zhang, Liping Yu, Andriy Zakutayev, and Alex Zunger. Sorting stable versus unstable hypothetical compounds: The case of multi-functional abx half-heusler filled tetrahedral structures. *Advanced Functional Materials*, 22(7):1425–1435, 2012.
- [125] C. Weber, C.-H. Yee, K. Haule, and G. Kotliar. Scaling of T_{cmax} with the charge-transfer energy in hole-doped cuprates. *ArXiv e-prints*, August 2011.
- [126] Hirofumi Sakakibara, Hidetomo Usui, Kazuhiko Kuroki, Ryotaro Arita, and Hideo Aoki. Two-orbital model explains the higher transition temperature of the single-layer hg-cuprate superconductor compared to that of the la-cuprate superconductor. *Phys. Rev. Lett.*, 105:057003, Jul 2010.
- [127] Hirofumi Sakakibara, Hidetomo Usui, Kazuhiko Kuroki, Ryotaro Arita, and Hideo Aoki. Origin of the material dependence of T_c in the single-layered cuprates. *Phys. Rev. B*, 85:064501, Feb 2012.
- [128] G. Kresse and J. Hafner. Ab initio molecular dynamics for liquid metals. *Phys. Rev. B*, 47:558, 1993.
- [129] G. Kresse and J. Hafner. Ab initio molecular-dynamics simulation of the liquid-metal-amorphous-semiconductor transition in germanium. *Phys. Rev. B*, 49:14251, 1994.
- [130] G. Kresse and J. Furthmüller. Efficiency of ab-initio total energy calculations for metals and semiconductors using a plane-wave basis set. *Comput. Mat. Sci.*, 6:15, 1996.
- [131] P. E. Blchl. Projector augmented-wave method. *Phys. Rev. B*, 50:17953, 1994.
- [132] G. Kresse and D. Joubert. From ultrasoft pseudopotentials to the projector augmented-wave method. *Phys. Rev. B*, 59:1758, 1999.
- [133] J.-P. Locquet, J. Perret, J. Fompeyrine, E. Mchler, J. W. Seo, and G. Van Tendeloo. Doubling the critical temperature of $\text{La}_{1.9}\text{Sr}_{0.1}\text{CuO}_4$ using epitaxial strain. *Nature*, 394:453–456, Jul 1998.

- [134] R. Hord, H. Luetkens, G. Pascua, A. Buckow, K. Hofmann, Y. Krockenberger, J. Kurian, H. Maeter, H.-H. Klauss, V. Pomjakushin, A. Suter, B. Albert, and L. Alff. Enhanced two-dimensional behavior of metastable T' - La_2CuO_4 , the parent compound of electron-doped cuprate superconductors. *Phys. Rev. B*, 82:180508, Nov 2010.
- [135] A. Tsukada, Y. Krockenberger, M. Noda, H. Yamamoto, D. Manske, L. Alff, and M. Naito. New class of t' -structure cuprate superconductors. *Solid State Communications*, 133(7):427 – 431, 2005.
- [136] Meghan Knapp. *Investigations Into The Structure And Properties Of Ordered Perovskites, Layered Perovskites, And Defect Pyrochlores*. PhD thesis, Ohio State University, 2006.
- [137] Shiro Kambe, Yoko Ichimaru, Eiji Sato, Chika Yoshida, and Osamu Ishii. Correlation between transition temperature, in-plane copper-oxygen bond length, and tilt/buckling of the CuO_2 plane in cuprate superconductors. *Bull. Yamagata Univ. (Eng.)*, 27(1), February 2002.
- [138] Jan Kuneš, Ryotaro Arita, Philipp Wissgott, Alessandro Toschi, Hiroaki Ikeda, and Karsten Held. Computer physics communications; wien2wannier: From linearized augmented plane waves to maximally localized wannier functions. *Computer Physics Communications*, 181(11):1888 – 1895, 2010.
- [139] Arash A. Mostofi, Jonathan R. Yates, Young-Su Lee, Ivo Souza, David Vanderbilt, and Nicola Marzari. wannier90: A tool for obtaining maximally-localised wannier functions. *Computer Physics Communications*, 178(9):685–699, 2008.
- [140] Gabriel Kotliar, Sergej Y. Savrasov, Gunnar Pálsson, and Giulio Biroli. Cellular dynamical mean field approach to strongly correlated systems. *Phys. Rev. Lett.*, 87(18):186401, Oct 2001.
- [141] C. A. Perroni, H. Ishida, and A. Liebsch. Exact diagonalization dynamical mean-field theory for multiband materials: Effect of coulomb correlations on the fermi surface of $\text{Na}_0.3\text{CoO}_2$. *Phys. Rev. B*, 75(4):045125, Jan 2007.

- [142] X. Y. Zhang, M. J. Rozenberg, and G. Kotliar. Mott transition in the $d=\infty$ hubbard model at zero temperature. *Phys. Rev. Lett.*, 70:1666–1669, Mar 1993.
- [143] Henrik Kajueter and Gabriel Kotliar. New iterative perturbation scheme for lattice models with arbitrary filling. *Phys. Rev. Lett.*, 77:131–134, Jul 1996.
- [144] F. Werner, O. Parcollet, A. Georges, and S. R. Hassan. Interaction-induced adiabatic cooling and antiferromagnetism of cold fermions in optical lattices. *Phys. Rev. Lett.*, 95:056401, Jul 2005.

Appendix A

Nonorthonormal Basis Sets

When discussing the APW and DMFT bases, we must establish some notation for nonorthonormal basis sets. We must do this because the basis sets used in DFT calculations (namely the APW sets) are not orthonormal and this fact directly impacts our construction of the DMFT impurity Green's function.

Consider a nonorthonormal basis $|u^\kappa\rangle$, written with superscripts, which spans some Hilbert space. To deal with the nonorthonormality, conceptually and notionally, the best thing to do is to introduce a basis $|u_\kappa\rangle$, written with subscripts, dual to the original basis $|u^\kappa\rangle$. We want the dual basis to obey the following nice properties:

$$\delta_\lambda^\kappa = \langle u_\kappa | u^\lambda \rangle = \langle u^\kappa | u_\lambda \rangle \quad (\text{A.1})$$

$$1 = \sum_\kappa |u^\kappa\rangle \langle u_\kappa| = \sum_\kappa |u_\kappa\rangle \langle u^\kappa| \quad (\text{A.2})$$

To create such a dual basis, we first define the overlap matrix $S^{\kappa\lambda} = \langle u^\kappa | u^\lambda \rangle$, which is Hermitian and written with superscripts. Its inverse, written with subscripts, is defined by $\sum_\lambda (S^{-1})_{\kappa\lambda} S^{\lambda\mu} = \delta_\kappa^\mu$. Then the key equation defining a dual basis having all these properties is

$$|u_\kappa\rangle = \sum_\lambda |u^\lambda\rangle (S^{-1})_{\lambda\kappa}, \quad (\text{A.3})$$

and so we see that $(S^{-1})_{\kappa\lambda} = \langle u_\kappa | u_\lambda \rangle$. Any arbitrary state $|\psi\rangle$ can be expanded in terms of either basis,

$$|\psi\rangle = \sum_\kappa \psi_\kappa |u^\kappa\rangle = \sum_\kappa \psi_\kappa |u_\lambda\rangle S^{\lambda\kappa} = \sum_\kappa \psi^\lambda |u_\lambda\rangle. \quad (\text{A.4})$$

From this, we see that the matrix elements transform as

$$\psi^\lambda = S^{\lambda\kappa} \psi_\kappa. \quad (\text{A.5})$$

In the following, instead of writing raised and lowered indices, we will denote the dual basis by placing a bar over the appropriate index. With this notation, the position (subscript or superscript) of the index does not matter. Writing out the formulas defining unity and the overlap, we get

$$\delta_{\kappa\lambda} = \langle \bar{\kappa} | \lambda \rangle = \langle \kappa | \bar{\lambda} \rangle \quad S^{\kappa\lambda} = \langle \kappa | \lambda \rangle \quad (\text{A.6})$$

$$1 = \sum_{\kappa} |\kappa\rangle \langle \bar{\kappa}| = \sum_{\kappa} |\bar{\kappa}\rangle \langle \kappa| \quad (S^{-1})_{\kappa\lambda} = \langle \bar{\kappa} | \bar{\lambda} \rangle \quad (\text{A.7})$$

and the transformation (index “raising” and “lowering”) equations are

$$|\bar{\kappa}\rangle = \sum_{\lambda} |\lambda\rangle (S^{-1})_{\lambda\kappa} \quad \psi_\kappa = S^{\kappa\lambda} \psi_{\bar{\lambda}} \quad (\text{A.8})$$

$$|\kappa\rangle = \sum_{\lambda} |\lambda\rangle S^{\lambda\kappa} \quad \psi_{\bar{\kappa}} = (S^{-1})_{\kappa\lambda} \psi_\lambda. \quad (\text{A.9})$$

We use the “bar” notation in our discussion of the implementation of DFT+DMFT in the FP-LAPW formalism.

Appendix B

APW Symmetries

Taking advantage of lattice symmetries reduces the computational cost of calculating the projector. The symmetries are described by a space group whose elements are denoted Γ_α , where $\alpha = 1, 2, \dots, N$ indexes the N elements of the space group. The space group elements are decomposed into a rotation $R(\theta, \phi, \psi)$ followed by a translation $T_{\mathbf{t}}$, so $\Gamma_\alpha = T_{\mathbf{t}_\alpha} R_\alpha$. The key matrix element to calculate is $\langle \tau_i \kappa l m | n \mathbf{k} \rangle$, where we have assumed the DMFT basis is located in the first unit cell ($\mathbf{R} = 0$), and ignored spin. Here, the crystal momentum \mathbf{k} runs over the entire Brillouin zone, and i indexes the equivalent atoms in the unit cell.

Now we make use of symmetries. We only need to specify the KS eigenstates in the irreducible Brillouin zone, $|n \mathbf{k}_{\text{IBZ}}\rangle$, and from this the full set of eigenstates can be generated by $\Gamma_\alpha^{-1} |n \mathbf{k}_{\text{IBZ}}\rangle$. Additionally, we only need to specify the DMFT orbitals at the origin $|\kappa l m\rangle$. We can transform these orbitals to be centered at the position of the first atom τ_1 by applying $T_{\tau_1} |\kappa l m\rangle$. Additionally, if we want the orbitals to be oriented at some arbitrary direction with respect to the global coordinate system, we can first apply a local rotation R_0 . Thus the DMFT basis for the first atom is $|\tau_1 \kappa l m\rangle = T_{\tau_1} R_0 |\kappa l m\rangle$. Finally, orbitals for the remainder of the equivalent atoms are generated by applying the space group operations $|\tau_i \kappa l m\rangle = \Gamma_i |\tau_1 \kappa l m\rangle$, where the space group element Γ_i takes us from the first to the i th atom.

Assembling all the pieces, we have

$$\langle \kappa l m | \Gamma_1^{-1} \Gamma_i^{-1} \Gamma_\alpha^{-1} | n \mathbf{k}_{\text{IBZ}} \rangle = \sum_{\mathbf{G}} \langle \kappa l m | \Gamma_1^{-1} \Gamma_i^{-1} \Gamma_\alpha^{-1} | \mathbf{G} \rangle \langle \mathbf{G} | n \mathbf{k}_{\text{IBZ}} \rangle, \quad (\text{B.1})$$

where we have defined $\Gamma_1 \equiv T_{\tau_1} R_0$. Since the APW code specifies the eigenvectors in the APW basis $|\mathbf{G}\rangle$, we inserted unity in the form of $1 = \sum_{\mathbf{G}} |\mathbf{G}\rangle \langle \mathbf{G}|$ after the equality. We concentrate on computing $\langle \kappa l m | \Gamma_1^{-1} \Gamma_i^{-1} \Gamma_\alpha^{-1} | \mathbf{G} \rangle$.

We need to figure out how Γ^{-1} acts on APW states $|\mathbf{G}\rangle$. Since the APW states transform like plane waves, we have

$$\langle \mathbf{r} | \Gamma^{-1} | \mathbf{G} \rangle = \langle \Gamma \mathbf{r} | \mathbf{G} \rangle = \langle T_{\mathbf{t}} R \mathbf{r} | \mathbf{G} \rangle = \langle R \mathbf{r} + \mathbf{t} | \mathbf{G} \rangle = e^{i(R\mathbf{r}+\mathbf{t}) \cdot \mathbf{G}} = e^{i\mathbf{t} \cdot \mathbf{G}} \langle \mathbf{r} | R^{-1} \mathbf{G} \rangle, \quad (\text{B.2})$$

which can be summarized as

$$\Gamma^{-1} | \mathbf{G} \rangle = e^{i\mathbf{t} \cdot \mathbf{G}} | R^{-1} \mathbf{G} \rangle. \quad (\text{B.3})$$

Applying this formula three times, we get

$$\Gamma_1^{-1} \Gamma_i^{-1} \Gamma_\alpha^{-1} | \mathbf{G} \rangle = e^{i(\mathbf{t}_\alpha \cdot \mathbf{G} + \mathbf{t}_i \cdot R_\alpha^{-1} \mathbf{G} + \tau_1 \cdot R_i^{-1} R_\alpha^{-1} \mathbf{G})} | R_0^{-1} R_i^{-1} R_\alpha^{-1} \mathbf{G} \rangle \quad (\text{B.4})$$

Appendix C

Slave-bosons for the Anderson Impurity Model

This appendix details the slave-boson mean-field theory for the Anderson impurity model. We work in the infinite- U limit and with multiple impurity levels to model the effects of spin-orbit splitting on the Kondo resonance. We also consider the effect of a conduction band gap at the fermi level on Kondo and multiplet physics.

We take as our model the Anderson impurity hamiltonian generalized to multiple orbitals, indexed by m . For example, in the case of the f -shell, spin-orbit coupling splits the fourteen orbitals into a $j = 5/2$ sextet and a $j = 7/2$ octet. We map these quantum numbers $|j j_z\rangle$ onto a single index $|m\rangle$. The impurity electrons hybridize with a single band of conduction electrons,

$$H = \sum_{\vec{k}\sigma} \epsilon_{\vec{k}} n_{\vec{k}\sigma} + \sum_m \epsilon_m n_m + \sum_{\vec{k}\sigma m} (V_{\vec{k}\sigma m} d_m^\dagger c_{\vec{k}\sigma} + \text{h.c.}) + \frac{U}{2} \sum_{m' \neq m} n_{m'} n_m. \quad (\text{C.1})$$

We take the fermi level to be at zero, so the impurity levels ϵ_m are negative. Unfortunately, the current basis doesn't make the symmetries of the hopping process clearly appear in the matrix elements $V_{\vec{k}\sigma m}$. In particular, if we consider the conduction electrons to be in a large spherical box, the model posses rotational symmetry, so angular momentum must be conserved.

Conservation of angular momentum means that hoppings out of the f -shell only couple to the $j = 5/2$ and $j = 7/2$ modes of the conduction electrons. Given these symmetries, it's better to work in the radial spin-orbit coupled basis $|k m\rangle$ for the conduction electrons as well where m is the mapped quantum number which runs over the fourteen angular momentum states and k is the radial quantum number. There is

no translational symmetry due to the presence of the impurity so linear momentum is not conserved in the hopping process.

With this change of basis, our hamiltonian becomes,

$$H = \sum_{km} \epsilon_{km} n_{km} + \sum_m \epsilon_m n_m + \sum_{km} (V_{km} d_m^\dagger c_{km} + \text{h.c.}) + \frac{U}{2} \sum_{m' \neq m} n_{m'} n_m. \quad (\text{C.2})$$

Although we choose the same notation as in the first version of the hamiltonian, the conduction dispersion ϵ_k is now the radial dispersion for the fourteen relevant angular modes.

The next step is to implement the infinite- U limit by introducing slave-bosons b and b^\dagger via the substitution $d_m^\dagger \rightarrow f_m^\dagger b$. The idea is to remap the original impurity hilbert space $\{|0\rangle, d_m^\dagger|0\rangle\}$ onto $\{b^\dagger|0\rangle, f_m^\dagger|0\rangle\}$. However, we need to make sure we stay within the physical hilbert space since states like $|0\rangle$ and $f_m^\dagger f_{m'}^\dagger|0\rangle$ are unphysical. To do this, we introduce the charge operator

$$Q = b^\dagger b + \sum_m f_m^\dagger f_m. \quad (\text{C.3})$$

We must constrain Q to unity at all times, which we do by using a functional δ -function,

$$\prod_\tau \delta(Q(\tau) - 1) = \prod_\tau \Delta\tau \int \frac{d\lambda}{2\pi} e^{-i\Delta\tau\lambda(\tau)(Q(\tau)-1)} \quad (\text{C.4})$$

$$= \int \mathcal{D}\lambda e^{-\int_0^\beta d\tau i\lambda(\tau)(Q(\tau)-1)}. \quad (\text{C.5})$$

Here, we work at finite temperature β with $\Delta\tau = \beta/N$, where N is the number of time steps before the continuum limit is taken. The effect of the constraint is into introduce a new bosonic field λ , which has units of temperature β^{-1} . When we make the slave-boson substitution, the interaction term disappears because there can be at most one electron occupying the impurity level in the infinite- U limit.

Including the constraint, we arrive at the infinite- U lagrangian,

$$\begin{aligned} \mathcal{L}(\tau) = & \sum_{km} c_{km}^\dagger (\partial_\tau + \epsilon_{km}) c_{km} + \sum_m f_m^\dagger (\partial_\tau + \epsilon_m + i\lambda) f_m \\ & + \sum_{km} (V_{km} f_m^\dagger b c_{km} + \text{h.c.}) + b^\dagger (\partial_\tau + i\lambda) b - i\lambda. \end{aligned} \quad (\text{C.6})$$

The partition function is given by,

$$Z = \int \mathcal{D}[f^\dagger f b^\dagger b c^\dagger c \lambda] e^{-S}, \quad S = \int_0^\beta d\tau \mathcal{L}(\tau). \quad (\text{C.7})$$

C.1 Review of Mean-field theory

There are two ways to do mean-field theory, differing on whether or not the fermionic fields are integrated out. For sake of simplicity, let's consider the following action with only one bosonic field ϕ ,

$$Z = \int \mathcal{D}[\psi^\dagger \psi \phi] e^{-S[\psi^\dagger \psi \phi]}. \quad (\text{C.8})$$

The goal is to find the one configuration of the bosonic field $\phi_0(\tau)$, called the *mean-field configuration* or simply *mean-field*, which minimizes the free energy $F = -T \log Z$. This approximation freezes out quantum fluctuations (these quantum fluctuations are represented by the path integral over ϕ , which will disappear), meaning the mean-field is effectively classical.

The more intuitive approach is to immediately make the mean-field approximation $\phi(\tau) = \phi_0 = \text{const.}$ Generally, we assume the mean-field is independent of time, although there are cases where the mean-field configuration is time-dependent. Taking ϕ constant means the action becomes a regular function of ϕ and that the path integral over ϕ can be done since $\int \mathcal{D}\phi = 1$. Thus we get for the partition function

$$Z(\phi_0) = \int \mathcal{D}[\psi^\dagger \psi] e^{-S[\psi^\dagger \psi](\phi_0)}. \quad (\text{C.9})$$

Minimizing F is equivalent to extremizing Z , so we need to solve

$$0 = \frac{\partial Z}{\partial \phi_0} = - \int \mathcal{D}[\psi^\dagger \psi] \frac{\partial S}{\partial \phi_0} e^{-S(\phi_0)} = - \left\langle \frac{\partial S}{\partial \phi_0} \right\rangle_{\text{MF}}. \quad (\text{C.10})$$

The brackets denote the expectation value under the path integral with ϕ already taken equal to its mean-field value ϕ_0 .

The equation can be simplified even further by recalling that

$$S = \int d\tau \left(\psi^\dagger \partial_\tau \psi + \phi \partial_\tau \phi + H \right). \quad (\text{C.11})$$

When we make the mean-field approximation, the term $\phi \partial_\tau \phi$ vanishes, and when we take the derivative with respect to ϕ_0 , we kill the first term $\psi^\dagger \partial_\tau \psi$. These manipulations reduce our extremization condition to

$$0 = \int d\tau \left\langle \frac{\partial H}{\partial \phi_0} \right\rangle_{\text{MF}}. \quad (\text{C.12})$$

If the physics is time-translation invariant, meaning H is time-independent, then the expectation of the any combination of operators $\langle \psi^\dagger(\tau)\psi(\tau)\cdots \rangle$ is independent of the time τ at which the expectation is taken. Specifically, the expectation of ∂H is independent of time, so we can replace the integral over τ by a factor of β , which then drops out of the equation. The final form of our condition is

$$0 = \left\langle \frac{\partial H}{\partial \phi_0} \right\rangle_{\text{MF}}, \quad (\text{C.13})$$

called the *mean-field equation* (MFE). The quantity $H = H(\phi_0)$ is called the *mean-field hamiltonian* from which we can often derive a good deal of insight. The task is to calculate the expectation value and then solve for value of ϕ_0 which minimizes the free energy. It's worth mentioning that the MFE is often solved at $T = 0$, a limit which can be taken only after we have derived the MFE.

The second, more formal and perhaps less intuitive approach is to integrate over the fermionic degrees of freedom first, leaving only the bosonic field ϕ ,

$$Z = \int \mathcal{D}\phi e^{-S_{\text{eff}}[\phi]}. \quad (\text{C.14})$$

Again we make the (temporally constant) mean-field approximation $\phi(\tau) = \phi_0$, whereby the path integral vanishes and we are left with

$$Z = e^{-S_{\text{eff}}(\phi_0)}. \quad (\text{C.15})$$

In this simple form, we see that the mean-field free energy $F = TS_{\text{eff}}(\phi_0)$. The extremization condition is

$$0 = \frac{\partial S_{\text{eff}}}{\partial \phi_0}, \quad (\text{C.16})$$

which is the MFE.

Each method has its strengths. The second approach generally requires the evaluation of various traces (in the form of Matsubara summations) when the fermions are integrated out. This can be a delicate step especially when branch cuts are involved. In contrast, the hard part of the first method is evaluation of the expectation values $\sim \langle \psi^\dagger \psi \rangle$, which require the computation of Green's functions from diagrammatics.

In the following sections, we will use the first method to obtain the mean-field theory for the AIM.

C.2 Mean-Field Equations of the Anderson Impurity Model

The first step is to establish notation for the mean-fields. For the bosons b , it turns out the mean-field is purely real, so we replace $b(\tau)$, $b^\dagger(\tau) \rightarrow \sqrt{z}$. The constraint field λ will turn out to be purely imaginary, so we replace $\lambda(\tau) \rightarrow -i\lambda$. Making these substitutions, we get the mean-field hamiltonian,

$$H_{\text{MF}} = \sum_{km} \epsilon_{km} n_{km} + \sum_m (\epsilon_m + \lambda) n_m + \sqrt{z} \sum_{km} (V_{km} f_m^\dagger c_{km} + \text{h.c.}) + \lambda(z - 1). \quad (\text{C.17})$$

We can read out a good deal of physics from the form of H_{MF} . The hamiltonian is of the single-particle form, and is separable into a sum of terms, one for each angular momentum mode m , so we can consider them separately. The f density of states for mode m is a lorentzian centered at the renormalized energy $\epsilon_m + \lambda$ with width proportional to a renormalized hybridization strength $\sim zV^2$. Alternatively, we can think of a set of bare atomic f levels at energies ϵ_m which all have been rigidly translated by an amount λ and broadened by $\sim zV^2$. In this model, multiplets are renormalized atomic levels.

Having interpreted the result, we will solve the mean-field equations which give the values of z and λ . Taking the derivatives with respect to \sqrt{z} and λ , we arrive at

$$0 = \sum_{km} V_{km} \langle f_m^\dagger c_{km} \rangle + \lambda \sqrt{z} \quad (\text{C.18})$$

$$0 = \sum_m \langle n_m \rangle + z - 1. \quad (\text{C.19})$$

In deriving these equations, we took V_{km} and $\langle f_m^\dagger c_{km} \rangle$ to be real.

To compute the expectation values, we need the f - f and f - c Green's functions, which we will derive from diagrammatics. We'll work with retarded propagators since we eventually want physical quantities (retarded Green's functions do not have factors of the Fermi-Dirac distribution). The f Green's function is

$$G_m^f(\omega) = \frac{1}{\omega - \epsilon_m - \lambda - \Delta_m(\omega)}, \quad (\text{C.20})$$

where the hybridization is

$$\Delta_m(\omega) = z\Delta_m^0(\omega) = \sum_k \frac{zV_{km}^2}{\omega - \epsilon_{km} + i\eta}. \quad (\text{C.21})$$

We can get a very explicit expression for the hybridization by taking the thermodynamic limit and by assuming that the matrix element V is momentum independent,

$$\Delta_m(\omega) = \int d\epsilon \rho_m(\epsilon) zV_m^2 \frac{1}{\omega - \epsilon + i\eta}. \quad (\text{C.22})$$

Here, ρ_m is the density of states of the m conduction band, $\rho_m(\epsilon) = \sum_k \delta(\epsilon - \epsilon_{km})$.

Using Cauchy's principal value formula, we get

$$\Delta_m(\omega) = zV_m^2 \cdot \mathcal{P} \int d\epsilon \frac{\rho_m(\epsilon)}{\omega - \epsilon} - i\pi \rho_m(\omega) zV_m^2. \quad (\text{C.23})$$

The integral takes a little care to evaluate. In the limit of a wide flat conduction band from $-D$ to D ,

$$\mathcal{P} \int_{-D}^D d\epsilon \frac{1}{\omega - \epsilon} = \log \left| \frac{\omega - D}{\omega + D} \right| \rightarrow \frac{2\omega}{D}, \quad (\omega \ll D), \quad (\text{C.24})$$

which is small so we can ignore it. As a consequence of these approximations, we need to keep in mind that our results are only valid for energies well away from the bandwidth D . The result for the hybridization is

$$\Delta_m(\omega) \equiv -i\Delta_m \equiv -iz\Delta_m^0 = -i\pi\rho_m zV_m^2. \quad (\text{C.25})$$

Now we can calculate the f -electron occupancy via an expression reminiscent of the Friedel sum rule,

$$\langle n_m \rangle = \int d\omega f(\omega) \cdot -\frac{1}{\pi} \text{Im} \frac{1}{\omega - \epsilon_m - \lambda + i\Delta_m}. \quad (\text{C.26})$$

Taking the limit $T = 0$, we get

$$\langle n_m \rangle = \int_{-\infty}^0 d\omega \frac{1}{\pi} \frac{\Delta_m}{(\omega - \epsilon_m - \lambda)^2 + \Delta_m^2} = \frac{1}{\pi} \arctan \frac{\Delta_m}{\epsilon_m + \lambda}. \quad (\text{C.27})$$

The f - c Green's function can be written in terms of the full f - f propagator and the bare c - c propagator,

$$G_{km}^{fc}(\omega) = \sqrt{z}V_{km}G_m^f(\omega)G_{km}^{c(0)}(\omega), \quad (\text{C.28})$$

$$G_{km}^{c(0)}(\omega) = \frac{1}{\omega - \epsilon_{km} + i\eta}. \quad (\text{C.29})$$

The expectation value, summed over the radial momenta, is again given by a Friedel sum rule-like expression,

$$\sum_k V_{km} \langle f_m^\dagger c_{km} \rangle = \sum_k \sqrt{z} V_{km}^2 \int d\omega f(\omega) \cdot -\frac{1}{\pi} \text{Im} G_m^f(\omega) G_{km}^{c(0)}(\omega) \quad (\text{C.30})$$

$$= \sqrt{z} \int d\omega f(\omega) \cdot -\frac{1}{\pi} \text{Im} G_m^f(\omega) \Delta_m^0(\omega). \quad (\text{C.31})$$

Working at $T = 0$ and noting that the hybridization is purely imaginary, we get

$$\frac{\sqrt{z} \Delta_m^0}{\pi} \int_{-D}^0 d\omega \frac{\omega - \epsilon_m - \lambda}{(\omega - \epsilon_m - \lambda)^2 + \Delta_m^2} = \frac{\sqrt{z} \Delta_m^0}{2\pi} \log \frac{(\epsilon_m + \lambda)^2 + \Delta_m^2}{D^2}. \quad (\text{C.32})$$

This completes the evaluation of the expectation values.

Now we can write down explicitly the mean-field equations:

$$1 - z = \frac{1}{\pi} \sum_m \arctan \frac{z \Delta_m^0}{\epsilon_m + \lambda}, \quad (\text{C.33})$$

$$-\lambda = \sum_m \frac{\Delta_m^0}{\pi} \log \frac{\sqrt{(\epsilon_m + \lambda)^2 + (z \Delta_m^0)^2}}{D}. \quad (\text{C.34})$$

C.3 Solution for Degenerate Orbitals

The sums over the orbital index m are replaced by factors of N when the orbitals are equivalent, meaning their energies, hybridizations and associated conduction density of states are all the same. It is convenient to work with new mean-fields, the renormalized impurity level $E = \epsilon + \lambda$ and the renormalized hybridization $\Delta = z \Delta^0 = \pi \rho z V^2$. In this simplifying limit, we find the mean-field equations become

$$\Delta^0 - \Delta = \frac{N \Delta^0}{\pi} \arctan \frac{\Delta}{E}, \quad (\text{C.35})$$

$$\epsilon - E = \frac{N \Delta^0}{\pi} \log \frac{\sqrt{E^2 + \Delta^2}}{D}. \quad (\text{C.36})$$

These equations can be recast into a particularly attractive form by introducing a complex quantity $Z = E + i\Delta$ and observing that $\arctan(\Delta/E) = \arg Z$ is an angle and $\sqrt{E^2 + \Delta^2} = |Z|$ is a magnitude. Now the mean-field equations can be combined to give

$$Z^0 - Z = \frac{N \Delta^0}{\pi} \log \frac{Z}{D}, \quad (\text{C.37})$$

where we write $Z^0 = \epsilon + i\Delta^0$.

This equation is transcendental, so they cannot be solved exactly. They can be solved numerically, taking care to place the branch cut of the logarithm appropriately (i.e. choice in branch of the arctan). However, let's say we were interested in the case when $|E| \ll |\epsilon|$ and $z \ll 1$, called the *Kondo regime*. In this regime, we can drop Z from the left hand side and solve to get

$$\begin{aligned} Z &= D \exp\left(\frac{\pi Z_0}{N\Delta^0}\right) \\ &= D e^{\pi\epsilon/N\Delta^0} \left(\cos \frac{\pi}{N} + i \sin \frac{\pi}{N}\right). \end{aligned} \quad (\text{C.38})$$

The magnitude of Z defines a new scale called the *Kondo temperature*,

$$T_K \equiv |Z| = \sqrt{E^2 + \Delta^2} = D \exp\left(\frac{\pi\epsilon}{N\Delta^0}\right). \quad (\text{C.39})$$

The real and imaginary parts of Z are the renormalized impurity level and width,

$$E = T_K \cos(\pi/N), \quad (\text{C.40})$$

$$\Delta = T_K \sin(\pi/N). \quad (\text{C.41})$$

Both quantities are proportional to T_K , a scale generated from the cutoff with exponential dependence on the bare parameters. Thus, in the Kondo regime when both $|\epsilon|$ and Δ_0 are much larger than T_K , our solutions justify the approximation made. Finally, the phase of Z is the impurity occupation in units of π ,

$$\langle n_f \rangle = \frac{\arg Z}{\pi} = \frac{1}{\pi} \arctan \frac{\Delta}{E} = \frac{1}{N}. \quad (\text{C.42})$$

The mean-field results allows us to explore the N -dependence of the physics. The Kondo temperature increases with increasing N since $T_K \sim e^{-1/N}$. For the case of a single impurity level, the Kondo resonance is pinned exactly at the Fermi surface ($E = 0$) and its width is equal to the Kondo temperature ($\Delta = T_K$). As we increase N , weight shifts from the width to the impurity level, moving it above the Fermi surface. As $N \rightarrow \infty$, the Kondo peak is located at $E \rightarrow T_K$ and has lost all weight ($\Delta \rightarrow 0$).

These mean-field results also allow us to extract the beta function for the dimensionless Kondo coupling $J = \rho N V^2 / \pi |\epsilon|$, which represents second-order processes where an electron hops onto the impurity level and then off again. The beta function provides

the answer to the question of how J must change as high-energy degrees of freedom are successively integrated out in order to give the same low-energy physics. In the Kondo model, the low-energy physics is described by T_K and integration over high-energies is equivalent to decreasing the cutoff D . The key relation is the definition of the Kondo temperature,

$$T_K = D e^{-1/J}, \quad (\text{C.43})$$

Differentiating both sides by D gives,

$$0 = 1 + D \frac{\partial_D J}{J^2} \quad \rightarrow \quad \frac{\partial J}{\partial \log D} = -J^2, \quad (\text{C.44})$$

which is the beta function. The Kondo temperature T_K is the physical low-energy scale in the problem, so it is unchanged when high-energy features, namely the cutoff D , are varied. The negative sign is crucial, because it implies the coupling becomes weak at high-energies, and its presence is the definition of *asymptotic freedom*.

Finally, we can compute the physical impurity Green's function

$$G_m^d(t) = -i \langle T d_m(t) d_m^\dagger \rangle = -i \langle b^\dagger(t) f_m(t) f_m^\dagger b \rangle. \quad (\text{C.45})$$

The bosons are replaced by their mean-field value so the result is just the f Green's function rescaled:

$$G_m^d(\omega) = \frac{z}{\omega - E_m + i\Delta_m}. \quad (\text{C.46})$$

This expression does not obey the conventional normalization of the spectral function $\int d\omega (-1/\pi) \text{Im} G(\omega) = 1$, and instead we have

$$\int d\omega \frac{1}{\pi} \frac{z\Delta_m}{(\omega - E_m)^2 + \Delta_m^2} = z \ll 1. \quad (\text{C.47})$$

The mean-field approximation captures only the quasiparticle spectral weight. Describing the remaining, high-energy physics requires the inclusion of fluctuations, which we describe in a later section.

C.4 Solution for Atomic Multiplets

When the impurity levels do not all have the same energy, the Kondo resonance is split into a multiplet of peaks spaced by the original impurity energy splittings. Again,

we denote by $E_m = \epsilon_m + \lambda$ the renormalized impurity levels and define the complex quantities $Z_m = E_m + i\Delta_m$, $Z_0 = \epsilon_0 + i\Delta_0^0$. The mean-field equations can be cast into the following form:

$$Z_0^0 - Z_0 = \frac{\Delta_0^0}{\pi} \sum_m \left(\frac{\Delta_m^0}{\Delta_0^0} \log \frac{|Z_m|}{D} + i \arg Z_m \right). \quad (\text{C.48})$$

This isn't quite as pretty as in the degenerate case because the hybridizations Δ_m^0 in general can be different for each orbital channel. In the Kondo regime, again $|E_0| \ll |\epsilon_0|$ and $z \ll 1$ so we can drop Z_0 from the left hand side. Isolating the zeroth term in the sum gives

$$\frac{\Delta_0^0}{\pi} \log \frac{Z_0}{D} = Z_0^0 - \sum_{m \neq 0} \left(\frac{\Delta_m^0}{\Delta_0^0} \log \frac{|Z_m|}{D} + i \arg Z_m \right),$$

whereupon we solve for Z_0 to arrive at

$$Z_0 = -D e^{-\pi|\epsilon_0|/\Delta_0^0} \prod_{m \neq 0} \left(\frac{D}{|Z_m|} \right)^{\Delta_m^0/\Delta_0^0} e^{-i \arg Z_m}.$$

As before, we define the magnitude of this expression to be the Kondo temperature $T_{K,0}$ of the lowest level,

$$T_{K,0} = D e^{-\pi|\epsilon_0|/\Delta_0^0} \prod_{m \neq 0} \left(\frac{D}{\sqrt{E_m^2 + \Delta_m^2}} \right)^{\Delta_m^0/\Delta_0^0}. \quad (\text{C.49})$$

This expression isn't satisfactory because the renormalized quantities E_m and Δ_m appear in the right hand side. We remedy this by noting that the lowest (zeroth) impurity level is renormalized to nearly the Fermi level, meaning $\lambda \sim -\epsilon_0$, a fact which will be shown below. Then, $E_m = \epsilon_m + \lambda = \epsilon_m - \epsilon_0$ equal to the bare impurity level splittings, which are much greater than the renormalized hybridizations Δ_m , allowing us to drop the Δ_m^2 under the square root. Then, $|Z_m| \approx \epsilon_m - \epsilon_0$ and we get

$$T_{K,0} = D e^{-\pi|\epsilon_0|/\Delta_0^0} \prod_{m \neq 0} \left(\frac{D}{\epsilon_m - \epsilon_0} \right)^{\Delta_m^0/\Delta_0^0}. \quad (\text{C.50})$$

[what about the fact that the bottom level should be doubly degenerate?] Then, the zeroth renormalized impurity level and width are

$$E_0 = -T_{K,0} \cos \left(\sum_{m \neq 0} \arctan \frac{\Delta_m}{E_m} \right) \quad (\text{C.51})$$

$$\Delta_0 = T_{K,0} \sin \left(\sum_{m \neq 0} \arctan \frac{\Delta_m}{E_m} \right). \quad (\text{C.52})$$

Again, to eliminate renormalized quantities from the right hand side, we use the approximation $E_m \approx \epsilon_m - \epsilon_0$ and define the Kondo temperature of the m th Kondo peak by its width, $T_{K,m} = \Delta_m$. Additionally, since $\Delta_m \ll E_m$, we can approximate the arctangents by the value of their arguments. Finally, we can expand out the sine and cosine to get

$$E_0 = -T_{K,0} + \frac{T_{K,0}}{2} \left(\sum_{m \neq 0} \frac{T_{K,m}}{\epsilon_m - \epsilon_0} \right)^2 \quad (\text{C.53})$$

$$\Delta_0 = T_{K,0} \sum_{m \neq 0} \frac{T_{K,m}}{\epsilon_m - \epsilon_0}. \quad (\text{C.54})$$

Thus, the presence of split atomic levels shifts the Kondo peak up towards the Fermi surface from its original (single impurity level) value of $E_0 = -T_{K,0}$.

C.5 Effects of a Conduction Gap

There are cases (Kondo insulators come to mind) when the conduction band has a gap at the Fermi energy, leading to insulating behavior. In these systems, the ordinary hybridization gap $E_g^{(0)}$ from band theory is strongly renormalized to give an extremely narrow gap E_g , turning band gap insulators into semiconductors. Within the DMFT framework, we can describe these lattice effects via an effective impurity model where the only difference between the previous cases is the presence of the already renormalized gap in the conduction density of states $\rho_m(\omega)$. The goal of this section is to find the effect this gap on the Kondo physics.

We will take as our conduction band $\rho_m(\omega) = \rho_m \cdot (\theta(\omega - E_g) + \theta(-\omega - E_g))$, which is constant everywhere except within the gap of width $2E_g$. The key affected quantity is the hybridization, whose real part is now nonzero and will require careful evaluation of principal value integral in (C.23) to determine its value. In the text below, we will write the real and imaginary parts of the hybridization as $\Delta_m(\omega) = \Delta'_m(\omega) + i\Delta''_m(\omega)$, which is not to be confused with the constant $\Delta_m = \pi\rho_m z V_m^2$.

Using the gapped density of states, the principal value integral becomes

$$\mathcal{P} \int_{-D}^{-E_g} \frac{d\epsilon}{\omega - \epsilon} + \mathcal{P} \int_{E_g}^D \frac{d\epsilon}{\omega - \epsilon} = \log \left| \frac{(\omega + D)(\omega - E_g)}{(\omega + E_g)(\omega - D)} \right| \rightarrow \log \left| \frac{\omega - E_g}{\omega + E_g} \right|, \quad (\text{C.55})$$

where we assume $\omega \ll D$. Rewriting this result using the definition of the arctanh in terms of the logarithm,

$$\operatorname{arctanh} z = \frac{1}{2} \log \frac{1+z}{1-z}, \quad (\text{C.56})$$

we get the real part of the hybridization,

$$\Delta'_m(\omega) = zV_m^2 \cdot \mathcal{P} \int d\epsilon \frac{\rho_m(\epsilon)}{\omega - \epsilon} = -\frac{2\Delta_m}{\pi} \cdot \begin{cases} \operatorname{arctanh}(\omega/E_g) & (|\omega| < E_g) \\ \operatorname{arctanh}(E_g/\omega) & (|\omega| > E_g) \end{cases}. \quad (\text{C.57})$$

The imaginary part is directly proportional to the conduction density of states, so it acquires a gap,

$$\Delta''_m(\omega) = -\pi \rho_m(\omega) z V_m^2 = \begin{cases} -\eta & (|\omega| < E_g) \\ -\Delta_m & (|\omega| > E_g) \end{cases}, \quad (\text{C.58})$$

where the regulator η is a small positive number.

With these expressions for the hybridization, we can compute the f -electron Green's function,

$$G_m^f(\omega) = \frac{1}{\omega - E_m - \Delta'_m(\omega) - i\Delta''_m(\omega)}, \quad (\text{C.59})$$

where we write $E_m = \epsilon_m + \lambda$ for the location of the renormalized impurity level.

Taking the imaginary part, we arrive at an explicit expression for the f -electron spectral function,

$$-\frac{1}{\pi} \operatorname{Im} G_m^f(\omega) = \begin{cases} \delta\left(\omega - E_m + \frac{2\Delta_m}{\pi} \operatorname{arctanh} \frac{E_g}{\omega}\right) & (|\omega| < E_g) \\ \frac{1}{\pi} \frac{\Delta_m}{\left(\omega - E_m + \frac{2\Delta_m}{\pi} \operatorname{arctanh} \frac{E_g}{\omega}\right)^2 + \Delta_m^2} & (|\omega| > E_g) \end{cases}. \quad (\text{C.60})$$

This spectral function is plotted in Fig. C.1. The next step is to find the f -occupancy,

$$\begin{aligned} \langle n_m \rangle = \int^{-E_g} d\omega \frac{1}{\pi} \frac{\Delta_m}{(\omega - E_m + (2\Delta_m/\pi) \operatorname{arctanh}(E_g/\omega))^2 + \Delta_m^2} \\ + \int_{-E_g}^0 d\omega \delta(\omega - E_m + (2\Delta_m/\pi) \operatorname{arctanh}(\omega/E_g)), \end{aligned} \quad (\text{C.61})$$

where we worked at $T = 0$. These integrals must be evaluated numerically.

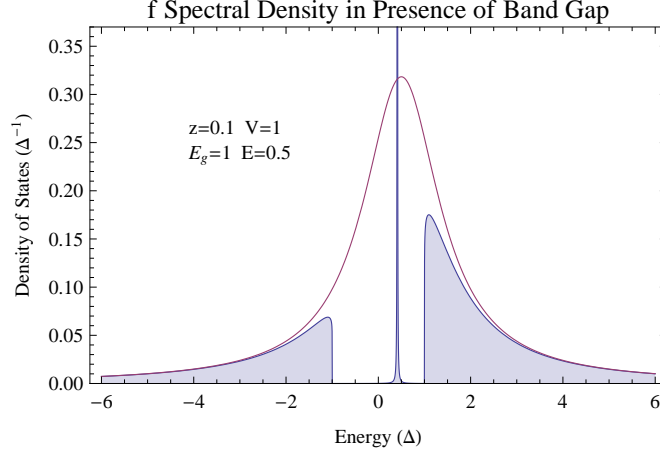


Figure C.1: The spectral density $-(1/\pi)\text{Im}G_m^f(\omega)$ for the f electron with (shaded) and without (line) a conduction band gap. The physical picture is as follows: without the gap, the density of states was a simple lorentzian of width Δ_m centered at an energy $\epsilon_m + \lambda \equiv E_m$ above the fermi surface. Turning on the gap causes the f -density to vanish within the gap, but also leaves the spectrum relatively unchanged outside the gap. The total spectral weight must be conserved, so the original weight within the gap is collected into a single delta peak located near the renormalized f -level.

We also need the second expectation value, which expands into a sum of three terms now that $\Delta'_m(\omega)$ is nonvanishing:

$$\begin{aligned}
& \sum_k V_{km} \langle f_m^\dagger c_{km} \rangle \\
&= \sqrt{z} \int_{-E_g}^{-E_g} d\omega \frac{1}{\pi} \frac{\Delta_m}{(\omega - E_m + (2\Delta_m/\pi) \text{arctanh}(E_g/\omega))^2 + \Delta_m^2} \left(-\frac{2\Delta_m^0}{\pi} \text{arctanh} \frac{E_g}{\omega} \right) \\
& \quad + \sqrt{z} \int_{-E_g}^0 d\omega \delta(\omega - E_m + (2\Delta_m/\pi) \text{arctanh}(\omega/E_g)) \left(-\frac{2\Delta_m^0}{\pi} \text{arctanh} \frac{\omega}{E_g} \right) \\
& \quad + \sqrt{z} \int_{-D}^{-E_g} d\omega \frac{\omega - E_m + (2\Delta_m/\pi) \text{arctanh}(E_g/\omega)}{(\omega - E_m + (2\Delta_m/\pi) \text{arctanh}(E_g/\omega))^2 + \Delta_m^2} \left(\frac{\Delta_m^0}{\pi} \right). \quad (\text{C.62})
\end{aligned}$$

With these expressions, we can solve the MFE numerically.

C.6 Beyond Mean-Field: Fluctuations

Quantum fluctuations of fields around their mean-field values will give rise to new physics. This is perhaps best shown in the second approach, when the fermions of our simplified system have already been integrated out and the action is a functional $S_{\text{eff}}[\phi]$. The idea is to Taylor expand the action about the mean-field value ϕ_0 , so that

the resulting expression is in powers of $\Delta\phi \equiv \phi - \phi_0$, giving:

$$S_{\text{eff}}[\phi](\phi_0) = S_{\text{eff}}[\phi_0] + \int d\tau \Delta\phi(\tau) \left(\frac{\delta S_{\text{eff}}}{\delta\phi} \right)_{\phi_0} \\ + \int d\tau \int d\tau' \Delta\phi(\tau) \left(\frac{\delta^2 S_{\text{eff}}}{\delta\phi(\tau)\delta\phi(\tau')} \right)_{\phi_0} \Delta\phi(\tau') + \dots$$

The coefficients of the expansion,

$$S_1(\tau; \phi_0) = \left(\frac{\delta S_{\text{eff}}}{\delta\phi} \right)_{\phi_0} \quad (\text{C.63})$$

$$S_2(\tau, \tau'; \phi_0) = \left(\frac{\delta^2 S_{\text{eff}}}{\delta\phi(\tau)\delta\phi(\tau')} \right)_{\phi_0}, \quad (\text{C.64})$$

are just ordinary functions of time and the scalar ϕ_0 . We see now that the MFE can equivalently be thought of as the condition that the linear coefficient vanishes for all time, $S_1(\tau; \phi_0) = 0$. Truncating the series to quadratic order, we get the partition to second order:

$$Z(\phi_0) = Z_0 \int \mathcal{D}[\phi] e^{-\int d\tau \int d\tau' \Delta\phi(\tau) S_2(\tau, \tau'; \phi_0) \Delta\phi(\tau')} \\ = Z_0 (\det S_2(\tau, \tau'; \phi_0))^{-1/2} \equiv Z_0 Z_2,$$

where $Z_0 = e^{-S_{\text{eff}}(\phi_0)}$ is the mean-field partition function. The mean-field free energy $F_0 = -T \log Z_0$ acquires a correction $F_2 = -T \log Z_2$. If $F_2 \ll F_0$, then we have confirmation that our choice of mean-field was correct.

Alternatively, we could have expanded

$$H = \sum_{km} \epsilon_{km} n_{km} + \sum_m (\epsilon_m + \lambda_0 + \lambda) n_m + \sum_{km} \{ V_{km} f_m^\dagger (\sqrt{z} + b) c_{km} + \text{h.c.} \} \\ + (\lambda_0 + \lambda) \{ b^\dagger b + \sqrt{z} (b + b^\dagger) + z - 1 \}. \quad (\text{C.65})$$

$$0 = \sum_{km} V_{km} \langle f_m^\dagger c_{km} \rangle + \lambda_0 \sqrt{z} + \langle \lambda b \rangle + \langle \lambda b^\dagger \rangle \quad (\text{C.66})$$

$$0 = \sum_m \langle n_m \rangle + \langle b^\dagger b \rangle + z - 1. \quad (\text{C.67})$$

The lowest-order correction to the boson self-energy is a f - c bubble, which gives a contribution

$$\Sigma(i\omega) = -\frac{1}{\beta} \sum_{km} \sum_{i\Omega} (-V_{km}) \frac{1}{i\Omega - E_m + i\Delta_m \text{sgn } \Omega} \cdot \frac{1}{-i\omega + i\Omega - \epsilon_{km}} (-V_{km}), \quad (\text{C.68})$$

where the external energy $i\omega$ is bosonic while the loop energy $i\Omega$ is fermionic, and the minus sign is due to the fermion loop. There are two types of Matsubara frequencies in this expression:

- The sum over internal Matsubara frequency ($i\Omega$) can either be done directly, or converted into contour integrals. This trick is called the Matsubara summation technique, and is not to be confused with analytic continuation, which strictly applies to external frequencies.
- The external frequency ($i\omega$) is treated as a Matsubara frequency while all the internal Matsubara sums are performed. In particular, if $i\Omega$ is an internal fermionic frequency, and $i\omega$ is an external bosonic frequency, then $f(i\Omega + i\omega) = f(i\Omega)$ when the Matsubara sum over $i\Omega$ is performed. Only afterwards, at the end of the calculation, is the external frequency analytically continued to the real axis. For example, $i\omega \rightarrow \omega + i0$ for retarded quantities.

First, we perform the Matsubara sum via the Matsubara formula $\beta^{-1} \sum_{i\Omega} h(i\Omega) = -\int (dz/2\pi i) h(z) f(z)$, to get

$$\Sigma(i\omega) = \frac{1}{\pi} \sum_m \Delta_m^0 \int d\epsilon \int \frac{dz}{2\pi i} \frac{1}{z - E_m + i\Delta_m \operatorname{sgn} \operatorname{Im} z} \cdot \frac{1}{-i\omega + z - \epsilon} f(z), \quad (\text{C.69})$$

where we have assumed a flat conduction band. The $\operatorname{sgn} \operatorname{Im} z$ is a significant feature whose analytic structure we now analyze. The first factor has a branch cut along the real axis and no poles, which can be seen by writing

$$\operatorname{sgn} x = \lim_{s \rightarrow 0} \frac{2}{\pi} \arctan \frac{x}{2\pi s} = \lim_{s \rightarrow 0} \frac{2}{\pi} \frac{1}{2i} \log \frac{1 + ix/2\pi s}{1 - ix/2\pi s} = \lim_{s \rightarrow 0} \frac{1}{i\pi} \log \frac{-x + i2\pi s}{x + i2\pi s}, \quad (\text{C.70})$$

which when extended to the complex plane has a branch cut along the imaginary axis. To create a sign function along the imaginary axis, we rotate this expression by 90 degrees, meaning $\operatorname{sgn} \operatorname{Im} z = \operatorname{sgn}(-iz)$. The result is a branch cut along the real axis. The second factor has a simple pole at $\epsilon + i\omega$.

Distorting the contour into a clockwise circle about the simple pole and two integrations just above and below the branch cut, we get

$$\begin{aligned} \Sigma(i\omega) = & -\frac{1}{\pi} \sum_m \Delta_m^0 \int d\epsilon \left(\frac{f(\epsilon)}{i\omega + \epsilon - E_m + i\Delta_m \operatorname{sgn} \omega} \right. \\ & \left. + \int dx \frac{1}{\pi} \frac{\Delta_m}{(x - E_m)^2 + \Delta_m^2} \frac{f(x)}{x - \epsilon - i\omega} \right). \end{aligned} \quad (\text{C.71})$$

Here, we have used the periodicity of the Fermi function to write $f(\epsilon + i\omega) = f(\epsilon)$. Also, $\operatorname{sgn} \operatorname{Im}(\epsilon + i\omega) = \operatorname{sgn} \omega$ since ϵ arises from a momentum sum and thus lives on the real axis.

At $T = 0$, the first integral is evaluated by decomposition into real and imaginary parts:

$$\begin{aligned} \int_{-D}^0 d\epsilon \frac{\epsilon - E_m - i\omega - i\Delta_m \operatorname{sgn} \omega}{(\epsilon - E_m)^2 + (\omega + \Delta_m \operatorname{sgn} \omega)^2} \\ = \frac{1}{2} \log \frac{E_m^2 + (\omega + \Delta_m \operatorname{sgn} \omega)^2}{D^2} - i \left(\arctan \frac{-E_m}{\omega + \Delta_m \operatorname{sgn} \omega} + \frac{\pi}{2} \operatorname{sgn} \omega \right), \end{aligned} \quad (\text{C.72})$$

where we simplified $\operatorname{sgn}(\omega + \Delta_m \operatorname{sgn} \omega) = \operatorname{sgn} \omega$ and assumed the bandwidth D is larger than all other scales. For the second integral, we evaluate the ϵ integral first, giving

$$\int d\epsilon \frac{1}{x - \epsilon - i\omega} = \int d\epsilon \frac{x - \epsilon + i\omega}{(x - \epsilon)^2 + \omega^2} \quad (\text{C.73})$$

$$= \frac{1}{2} \log \frac{(x - D)^2 + \omega^2}{(x + D)^2 + \omega^2} + i\pi \operatorname{sgn} \omega \longrightarrow i\pi \operatorname{sgn} \omega. \quad (\text{C.74})$$

The real part vanishes in the limit of a large symmetric bandwidth D (equivalent to taking the principal value). Now we evaluate the x integral, again at $T = 0$:

$$i\pi \operatorname{sgn} \omega \int_{-\infty}^0 dx \frac{1}{\pi} \frac{\Delta_m}{(x - E_m)^2 + \Delta_m^2} = i \left(\arctan \frac{-E_m}{\Delta_m} + \frac{\pi}{2} \right) \operatorname{sgn} \omega \quad (\text{C.75})$$

This completes the evaluation of the self-energy. We assemble here the main results: the Matsubara self-energy is

$$\begin{aligned} \Sigma(i\omega) = & -\frac{1}{\pi} \sum_m \Delta_m^0 \left[\frac{1}{2} \log \frac{E_m^2 + (\omega + \Delta_m \operatorname{sgn} \omega)^2}{D^2} \right. \\ & \left. + i \left(\arctan \frac{E_m}{\omega + \Delta_m \operatorname{sgn} \omega} - \arctan \frac{E_m}{\Delta_m \operatorname{sgn} \omega} \right) \right]. \end{aligned} \quad (\text{C.76})$$

This can be simplified to the following form which is easier for analytic continuation:

$$\Sigma(i\omega) = -\frac{1}{\pi} \sum_m \Delta_m^0 \left[\frac{1}{2} \log \frac{E_m^2 + \Delta_m^2}{D^2} + \log \frac{i\omega - E_m + i\Delta_m \operatorname{sgn} \omega}{-E_m + i\Delta_m \operatorname{sgn} \omega} \right]. \quad (\text{C.77})$$

From this, we can compute the retarded and advanced self-energies by analytically continuing just above or below the real axis:

$$\begin{aligned} \Sigma(\omega \pm i0) = & -\frac{1}{\pi} \sum_m \Delta_m^0 \left[\frac{1}{2} \log \frac{(\omega - E_m)^2 + \Delta_m^2}{D^2} \right. \\ & \left. \pm i \left(\arctan \frac{\omega - E_m}{\Delta_m} + \arctan \frac{E_m}{\Delta_m} \right) \right], \quad (\text{C.78}) \end{aligned}$$

The physical quantity of interest is the d Green's function. Fluctuations about the bosonic mean-field give a correction in the form of a b - f bubble, given by

$$G_m^{d(2)}(i\omega) = \frac{1}{\beta} \sum_{i\Omega} \frac{1}{i\Omega - E_m + i\Delta_m \text{sgn } \Omega} \cdot \frac{1}{i\Omega - i\omega - \lambda - \Sigma(i\Omega - i\omega)} \quad (\text{C.79})$$

$$= - \int \frac{dz}{2\pi i} \frac{1}{z - E_m + i\Delta_m \text{sgn } \text{Im } z} \cdot \frac{f(z)}{z - i\omega - \lambda - \Sigma(z - i\omega)}. \quad (\text{C.80})$$

The object whose analytic structure we must analyze carefully is the self-energy,

$$\Sigma(z) = -\frac{1}{\pi} \sum_m \Delta_m^0 \left[\frac{1}{2} \log \frac{E_m^2 + \Delta_m^2}{D^2} + \log \frac{z - E_m + i\Delta_m \text{sgn } \text{Im } z}{-E_m + i\Delta_m \text{sgn } \text{Im } z} \right].$$

There is a branch cut along the real axis due to the $\text{sgn } \text{Im } z$, but are there any other non-analyticities? First consider the logarithm. The branch points are located when the argument vanishes, meaning $z + i\Delta_m \text{sgn } \text{Im } z = E_m$ must be satisfied. This has no solutions for $\text{Im } z \neq 0$ so the logarithm contributes no new branch cuts. We conclude the self-energy only has a single cut along the real axis, which is shifted to $\text{Im } z = \omega$ when the self-energy is evaluated at $\Sigma(z - i\omega)$.

From the above analysis, we find our contour integral has two cuts: one is along the real axis from the fermion propagator, and the second is at $\text{Im } z = \omega$ due to the shifted self-energy. The contribution from the real axis cut is

$$\begin{aligned} \int dx \frac{1}{\pi} \frac{1}{(x - E_m)^2 + \Delta_m^2} \cdot \frac{f(x)}{x - i\omega - \lambda - \Sigma(x - i\omega)} \\ \approx \theta(-E_m) \frac{1}{E_m - i\omega - \lambda - \Sigma(E_m - i\omega)}. \quad (\text{C.81}) \end{aligned}$$

Using $f(x + i\omega) = -n_B(x)$, the contours along $\text{Im } z = \omega$ give

$$\mathcal{P} \int \frac{dx}{2\pi i} \frac{n_B(x)}{x - E_m + i\Delta_m \text{sgn } w} \cdot \frac{2i\Sigma_2(x + i0)}{(x - \lambda - \Sigma_1(x))^2 + \Sigma_2(x + i0)^2} \quad (\text{C.82})$$

The contribution from the pole in the bose function vanished because $\Sigma_2(0) = 0$. This entire expression is essentially $\sim \alpha \text{sgn } \omega + \beta$ which is an uninteresting constant when $i\omega$ is analytically continued.

Taking just the real axis contribution, and considering the Kondo regime when $E_m < 0$, we get

$$G_m^{d(2)}(\omega) \simeq -\frac{1}{\omega - E_m + \lambda + \Sigma(E_m - \omega)} \quad (\text{C.83})$$

with the self-energy

$$\begin{aligned} \Sigma(E_m - \omega) = & -\sum_n \frac{\Delta_n^0}{2\pi} \log \frac{(\omega + E_n - E_m)^2 + \Delta_n^2}{D^2} \\ & + \frac{i}{\pi} \left(\arctan \frac{\omega + E_n - E_m}{\Delta_n} + \arctan \frac{E_n}{\Delta_n} \right) \end{aligned} \quad (\text{C.84})$$

We can eliminate the bandwidth by noting the following:

$$1 = e^{\pi\epsilon_0/\Delta_0^0} \prod_m \left(\frac{D}{|Z_m|} \right)^{\Delta_m^0/\Delta_0^0}. \quad (\text{C.85})$$

Inverting and taking the logarithm, we get

$$0 = -\epsilon_0 - \sum_m \frac{\Delta_m^0}{\pi} \log \left(\frac{D}{|Z_m|} \right) = -\epsilon_0 - \sum_m \frac{\Delta_m^0}{2\pi} \log \frac{D^2}{E_m^2 + \Delta_m^2}, \quad (\text{C.86})$$

which can be inserted into the above expression for the Green's function to eliminate the bandwidth D :

$$G_m^{d(2)}(\omega) \simeq -\frac{1}{\omega - \epsilon_m - \epsilon_0 + \Sigma(E_m - \omega)} \quad (\text{C.87})$$

with

$$\begin{aligned} \Sigma(E_m - \omega) = & -\sum_n \frac{\Delta_n^0}{2\pi} \log \frac{(\omega + E_n - E_m)^2 + \Delta_n^2}{E_n^2 + \Delta_n^2} \\ & + \frac{i}{\pi} \left(\arctan \frac{\omega + E_n - E_m}{\Delta_n} + \arctan \frac{E_n}{\Delta_n} \right). \end{aligned} \quad (\text{C.88})$$

Appendix D

Downfolding and Cluster-DMFT Implementation Notes

D.1 Table of Parameters

We summarize in Table D.1 the parameters extracted via downfolding for the three-band model and discuss the details of the downfolding procedure.

The charge-transfer energy $\epsilon_d - \epsilon_p$ is a localized, atomic-like quantity. Inherent in the downfolding procedure is a tradeoff between atomic character versus faithful representation low-energy bands. In order to preserve as much as possible the atomic character, we implemented the first step of the downfolding procedure described in Ref. [115]. We chose as initial orbitals $g_n(\mathbf{r})$ the LDA+DMFT basis constructed in the manner described in Ref. [31]. The downfolding procedure is robust: we cross-checked our results by using Wien2Wannier [138] and Wannier90 [139] to perform the same downfolding procedure. Our code differs slightly in the choice of radial dependence of the trial orbitals $g_n(\mathbf{r})$. Again, in order to preserve the atomic character, we disabled the minimization of both spread functionals and did not use an inner window to constrain the Fermi surface. We find the extracted parameters differ by less than 5%.

In order to connect with prior work [103], we compute the range parameter $r \sim t'/t$ using Löwdin downfolding. Beginning with the three-band model,

$$H = \begin{pmatrix} \epsilon_d & 2t_{pd} \sin \frac{k_x}{2} & -2t_{pd} \sin \frac{k_y}{2} \\ 2t_{pd} \sin \frac{k_x}{2} & \epsilon_p + 2t_{pp'} \cos k_x & -4t_{pp'} \sin \frac{k_x}{2} \sin \frac{k_y}{2} \\ -2t_{pd} \sin \frac{k_y}{2} & -4t_{pp'} \sin \frac{k_x}{2} \sin \frac{k_y}{2} & \epsilon_p + 2t_{pp'} \cos k_y \end{pmatrix},$$

	Compound	$\epsilon_d - \epsilon_p$ (eV)	t_{pd} (eV)	t_{pp} (eV)	$t_{pp'}$ (eV)	t'/t	layers	$d_{\text{Cu-O}}^{\text{apical}}$ (Ang.)	T_c (K)
(1)	La_2CuO_4	2.61	1.39	0.640	0.103	0.070	1	2.3932	38
(2)	$\text{Pb}_2\text{Sr}_2\text{YCu}_3\text{O}_8$	2.32	1.30	0.673	0.160	0.108	2	2.3104	70
(3)	$\text{Ca}_2\text{CuO}_2\text{Cl}_2$	2.21	1.27	0.623	0.132	0.085	1	2.7539	26
(4)	$\text{La}_2\text{CaCu}_2\text{O}_6$	2.20	1.31	0.644	0.152	0.120	2	2.2402	45
(5)	$\text{Sr}_2\text{Nd}_2\text{NbCu}_2\text{O}_{10}$	2.10	1.25	0.612	0.144	0.110	2	2.0450	28
(6)	$\text{Bi}_2\text{Sr}_2\text{CuO}_6$	2.06	1.36	0.677	0.153	0.105	1	2.5885	24
(7)	$\text{YBa}_2\text{Cu}_3\text{O}_7$	2.05	1.28	0.673	0.150	0.110	2	2.0936	93
(8)	$\text{HgBa}_2\text{CaCu}_2\text{O}_6$	1.93	1.28	0.663	0.187	0.133	2	2.8053	127
(9)	$\text{HgBa}_2\text{CuO}_4$	1.93	1.25	0.649	0.161	0.122	1	2.7891	90
(10)	$\text{Sr}_2\text{CuO}_2\text{Cl}_2$	1.87	1.15	0.590	0.140	0.108	1	2.8585	30
(11a)	$\text{HgBa}_2\text{Ca}_2\text{Cu}_3\text{O}_8$ (outer)	1.87	1.29	0.674	0.184	0.141	3	2.7477	135
(11b)	$\text{HgBa}_2\text{Ca}_2\text{Cu}_3\text{O}_8$ (inner)	1.94	1.29	0.656	0.167	0.124	3	2.7477	135
(12)	$\text{Tl}_2\text{Ba}_2\text{CuO}_6$	1.79	1.27	0.630	0.150	0.121	1	2.7143	90
(13)	$\text{LaBa}_2\text{Cu}_3\text{O}_7$	1.77	1.13	0.620	0.188	0.144	2	2.2278	79
(14)	$\text{Bi}_2\text{Sr}_2\text{CaCu}_2\text{O}_8$	1.64	1.34	0.647	0.133	0.106	2	2.0033	95
(15)	$\text{Tl}_2\text{Ba}_2\text{CaCu}_2\text{O}_8$	1.27	1.29	0.638	0.140	0.131	2	2.0601	110
(16a)	$\text{Bi}_2\text{Sr}_2\text{Ca}_2\text{Cu}_3\text{O}_{10}$ (outer)	1.24	1.32	0.617	0.159	0.138	3	1.7721	108
(16a)	$\text{Bi}_2\text{Sr}_2\text{Ca}_2\text{Cu}_3\text{O}_{10}$ (inner)	2.24	1.32	0.678	0.198	0.121	3	1.7721	108

Table D.1: Tight-binding parameters of the three-band p - d model, containing the in-plane $d_{x^2-y^2}$ and $p_{(x,y)}$ orbitals, for the hole-doped cuprates. The table is sorted by decreasing charge-transfer energies $\epsilon_d - \epsilon_p$. We have included the two nearest-neighbor (intra-cell) hoppings t_{pd} and t_{pp} as well as the inter-cell oxygen-oxygen hopping $t_{pp'}$. Using the Löwdin procedure, we have integrated out the oxygen bands to arrive at a one-band model, from which we have extracted the ratio t'/t corresponding to the range parameter. We also include the distance between the in-plane copper and the apical atom $d_{\text{Cu-O}}^{\text{apical}}$. For the bilayer and trilayer compounds, we display the distance to the apical oxygens from the Cu atoms in the outer planes. The last column displays the maximum transition temperature $T_{c,\text{max}}$ for the corresponding optimally-doped compound. See Ref. [103] and citations therein for references to experimental work on structural determination and transition temperatures of the various cuprate families.

we integrate out the oxygen bands to arrive at the effective one-band hamiltonian,

$$H_{\text{eff}}(\omega) = \epsilon_d + t_{pd} \cdot \frac{\sum_{i=0}^2 A_i(\omega) a_i(\mathbf{k})}{\sum_{i=0}^2 B_i(\omega) a_i(\mathbf{k})},$$

where we have defined the Fourier harmonics as

$$a_0(\mathbf{k}) = 1$$

$$a_1(\mathbf{k}) = -2(\cos k_x + \cos k_y)$$

$$a_2(\mathbf{k}) = 4 \cos k_x \cos k_y$$

and the coefficients are

$$\begin{aligned} A_0 &= 4t_{pd}(\omega - \epsilon_p + 2t_{pp}) & B_0 &= (\omega - \epsilon_p)^2 - t_{pp}^2 \\ A_1 &= t_{pd}(\omega - \epsilon_p + 2t_{pp'} + 4t_{pp}) & B_1 &= t_{pp'}(\omega - \epsilon_p) - 2t_{pp}^2 \\ A_2 &= 2t_{pd}(t_{pp} + t_{pp'}) & B_2 &= t_{pp'}^2 - t_{pp}^2. \end{aligned}$$

Taking advantage of the fact that B_1/B_0 and B_2/B_0 are small, we expand out the denominator and collect coefficients of the Fourier harmonics to arrive at the range parameter

$$r \sim \frac{t'}{t} = \left. \frac{B_0 A_2 - A_0 B_2}{B_0 A_1 - A_0 B_1} \right|_{\omega=\epsilon_F} \quad (\text{D.1})$$

This procedure preserves the Fermi surface and faithfully represents the low-energy band-structure. Since we prioritized the faithful representation of the atomic quantities over the non-local hopping parameters, our values of $r \sim t'/t$ are smaller than those found in Ref. [103]. However, the trends remain unchanged.

D.2 Numerical Method

We solve the three-band hamiltonian (Eq. 8.3) using c-DMFT. We use in this work the realistic set of parameters shown in Table (D.1). We choose a 2×2 cluster in the cellular form [140]. Cluster DMFT improves on the single site DMFT by adding a non-local self-energy. In Fig. D.1.a we show the 2×2 copper plaquette used as a unit cell through

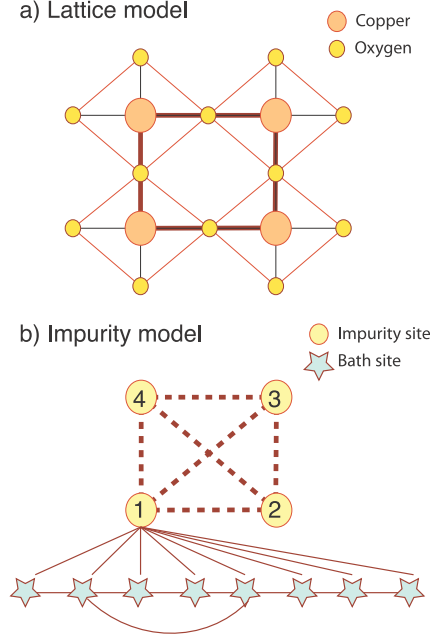


Figure D.1: (a) The d-p theoretical lattice model contains the $p_{(x,y)}$ orbitals of the in-plane oxygen atoms (small circles) and the $d_{x^2-y^2}$ orbital of the copper atoms (large circles). The figure shows the four copper plaquette unit-cell used in the cellular DMFT calculations. (b) The associated Anderson impurity model (AIM) contains four impurities (circles), each of them is independently connected to a bath discretized in eight sites (stars). There is not direct hybridization between the impurities, but the latter are connected by second order process through the bath (dashed lines). The sites of the bath are connected by direct and long-range hoppings.

the calculations. The lattice Green's function of the four Copper site plaquette is given by:

$$\mathbf{G}_{\mathbf{k}}(i\omega_n) = (i\omega_n + \mu - \mathbf{H}_{\mathbf{k}} - \mathbf{\Sigma}(i\omega_n))^{-1}, \quad (\text{D.2})$$

where $\mathbf{H}_{\mathbf{k}}$ is the Fourier transform of the uncorrelated part of the Hamiltonian defined in Eq. (8.3). $\mathbf{\Sigma}$ is the cluster self-energy matrix being nonzero only for the matrix elements connecting the $d_{x^2-y^2}$ orbitals.

The self energy matrix in Eq. (D.2) is obtained by solving an 2×2 impurity Anderson model (shown in Fig. D.1.b) subject to the DMFT self-consistency condition:

$$(i\omega - E_{imp} - \mathbf{\Sigma}(i\omega) - \mathbf{\Delta}(i\omega)) = \hat{P} \left(\frac{1}{N_k} \sum_{\mathbf{k} \in \text{BZ}} G_{\mathbf{k}}(i\omega) \right)^{-1}, \quad (\text{D.3})$$

where the sum runs over the reduced Brillouin Zone (BZ), and \hat{P} is projecting the averaged green function onto the impurity cluster subspace.

In this work we use the exact diagonalization impurity solver algorithm [117]. To solve the cluster impurity problem, we express it in the form of a Hamiltonian H_{imp} with a discrete number of bath orbitals coupled to the cluster and use the Lanczos algorithm to converge the ground state of the Hamiltonian and the lower states of the spectrum. The ED method in conjunction with c-DMFT has been widely used for the one-band model [118, 113, 141].

The Anderson Impurity Model (AIM) is defined by :

$$H_{imp} = \sum_{mn\sigma} \epsilon_{mn\sigma}^n (a_{m\sigma}^\dagger a_{n\sigma} + h.c.) + \sum_{mn\sigma} \epsilon_{mn\sigma}^a (a_{m\sigma}^\dagger a_{n-\sigma}^\dagger + h.c.) + \sum_{mi\sigma} V_{mi\sigma} (a_{m\sigma}^\dagger c_{i\sigma} + h.c.) + \mu \sum_{m\sigma} c_{m\sigma}^\dagger c_{m\sigma} + \sum_{i\sigma} U \hat{n}_{i\uparrow} \hat{n}_{i\downarrow}. \quad (D.4)$$

The fermionic operators a_{mn}^\dagger (a_{mn}) creates (destroys) a particle in the bath, and the fermionic operators c_{mn}^\dagger (c_{mn}) creates (destroys) a particle in the cluster of impurities. The indices m, n are running over the bath sites, and the index i is running over the impurity sites, the sites of the bath are connected by long-range hopping matrix elements through the particle-hole (particle-particle) channel ϵ^n (ϵ^a), the non-correlated sites of the bath are also connected to the correlated impurities by the matrix elements V_{mi} , the onsite repulsion at the impurity sites is U (equal to the Coulomb repulsion of the Copper site U_d), and μ is the chemical potential. We define ϵ as the extended matrix which contains the normal ϵ^n and anomalous ϵ^a blocks in the Nambu basis:

$$\epsilon = \begin{pmatrix} \epsilon^n & \epsilon^a \\ (\epsilon^a)^T & -(\epsilon^n)^T \end{pmatrix} \quad (D.5)$$

The Weiss field $\mathcal{G}(i\omega_n) = i\omega_n - \Delta(i\omega_n) - E_{imp}$ is constructed from the parameters of the AIM:

$$\Delta(i\omega_n) = \mathbf{V}^\dagger (i\omega_n - \epsilon)^{-1} \mathbf{V} \quad (D.6)$$

The parameters of (D.4) are determined by imposing the self-consistency condition in Eq. (D.3) using a conjugate gradient minimization algorithm:

$$d = \sum_{\omega < \omega_0, \alpha\beta} |\Delta_{\alpha\beta}^{ED}(i\omega_n) - \Delta_{\alpha\beta}(i\omega_n)|^2 \quad (D.7)$$

Where $\alpha\beta$ are running over the matrix elements, $\omega_0 = 20$ is a hard cutoff on the summation and Δ^{ED} is the function (D.6) of the Hamiltonian parameters. The fitting procedure is not exact due to the discretization of the bath and is an additional approximation to the c-DMFT scheme. In this work we considered a bath discretised with 8 energy levels. Finally, once the Hamiltonian parameters are obtained by the fitting procedure, we obtain the low energy spectrum by the Lanczos procedure. We impose an energy cutoff E_{max} such that the Boltzman weight $e^{-\beta(E_{max}-E_0)} < 0.001$, where E_0 is the ground state energy. We discard all the eigenstates which have an energy larger than the cutoff $E_i - E_0 > E_{max}$. Once the eigenstates are obtained we compute the Boltzman weighted average to get the dynamical and static observables.

In this work we consider two different instabilities: i) the superconducting phase, and ii) the long-range magnetic ordered phase. The former is computed in the Nambu basis, and the Hilbert space is block diagonalized by the spin S^z quantum numbers, and the latter is obtained in the tensor product of the up and down spins. Since the number of particles is not a good quantum number in the superconducting phase, we work at fixed chemical potential. For the magnetic phase we found a better convergence when working at fixed density, with a free chemical potential.

For the determination of the phase diagram we used physical observables readily available from the 2×2 cluster of impurities, such as the staggered magnetization $S^z = \frac{1}{2}(n_\uparrow - n_\downarrow)$, the superconducting order parameter $\Delta = \langle\langle c_1 c_2 \rangle\rangle_{(\tau=0)}$ (where 1 and 2 are nearest neighbor links of the impurity plaquette) and the anomalous self-energy at zero frequency $\Sigma^{an} \equiv \Sigma_{12}^{an}(\omega = 0)$. We emphasize that the computed order parameters do not rely on any additional procedure, such as the Σ -periodization [140], which interpolates and extrapolates the discrete cluster quantities to the continuum in k-space.

Finally, we discuss the computation of the double-counting correction E_{dc} . Since the Wannier functions of the three-band p - d model is not atomic-like, we cannot use the atomic double-counting proposed in Ref. [39]. Rather, we first perform the *ab initio*

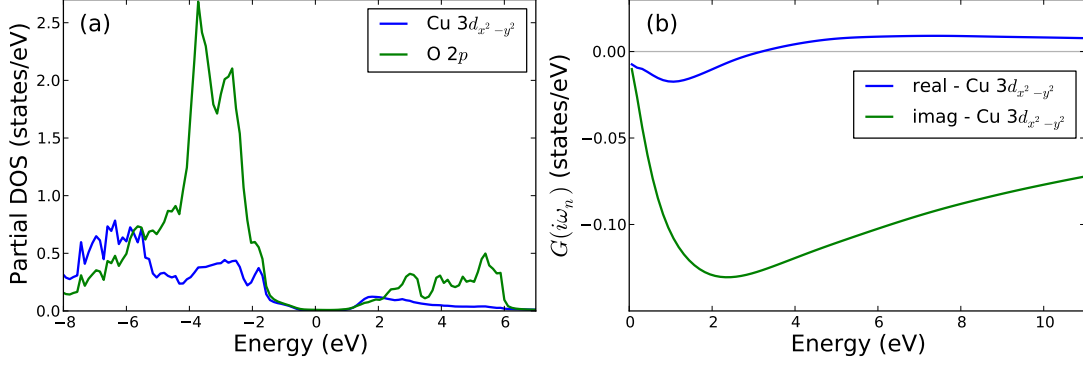


Figure D.2: (a) Density of states of LSCO from the all-electron DFT+DMFT calculation. (b) All-electron Matsubara Green's function for the Cu $3d_{x^2-y^2}$ orbital used as reference to fix double-counting in three-band p - d model. The temperature is $\beta = 50 \text{ eV}^{-1}$.

all-electron calculation using the atomic double-counting,

$$E_{\text{dc}} = U \left(n_{d0} - \frac{1}{2} \right) - J \left(\frac{n_{d0}}{2} - \frac{1}{2} \right), \quad (\text{D.8})$$

with $n_{d0} = 9$, the natural value derived from chemical valence counting. We use $U = 10 \text{ eV}$ and $J = 0.7 \text{ eV}$. The atomic form of the double-counting is appropriate here because treating the full energy window causes the orbitals to be very atomic-like. In Fig. D.2a, we plot the density of states from the all-electron calculation, which exhibits the charge-transfer gap of the correct magnitude (slightly less than 2 eV). Then, we select the double-counting in the p - d model so the Matsubara Green's function matches the corresponding quantity in the all-electron calculation (Fig. D.2b). We find that $E_{\text{dc}} = 3.12 \text{ eV}$ gives a good match, and use this value for all subsequent model calculations. Finally, we use a reduced onsite-repulsion $U_{3\text{-band}} \approx U - 2J$ for our 3-band calculations to capture the effect of the Hund's coupling present in the all-electron calculation.

Appendix E

Iterated Perturbation Theory

Why does iterated perturbation theory (IPT) capture the Mott transition of the half-filled Hubbard model? IPT is DMFT with the impurity self-energy computed via a diagrammatic expansion in U to second order. It is surprising that a truncated perturbative calculation in the interaction strength, captures the nonperturbative physics of the Mott transition.

The reason for its success is the simplicity of the strong-coupling limit [142]. We know the exact answer for the atomic Green's function ($\Delta/U \rightarrow 0$) at the particle-hole symmetric point,

$$G(i\omega_n) = \frac{1}{2} \left(\frac{1}{i\omega_n + U/2} + \frac{1}{i\omega_n - U/2} \right) = \frac{1}{i\omega_n - \Sigma(i\omega_n)}, \quad (\text{E.1})$$

from which we can extract the atomic self-energy:

$$\Sigma(i\omega_n) = \frac{1}{i\omega_n} \frac{U^2}{4}. \quad (\text{E.2})$$

The self-energy is proportional to U^2 only, without any higher powers.

The diagrammatics of IPT gives the same answer. In the extreme atomic limit, $\mathcal{G}_0^{-1} = i\omega_n$, and the polarization bubble in the self-energy is

$$P(i\nu_n) = -\frac{1}{\beta} \sum_{i\omega_n} \frac{1}{i\omega_n} \frac{1}{i\nu_n + i\omega_n} = \oint \frac{dz}{2\pi i} \frac{1}{z} \frac{f(z)}{i\nu_n + z} = \begin{cases} 0 & i\nu_n \neq 0 \\ -f'(0) & i\nu_n = 0 \end{cases} \quad (\text{E.3})$$

Then the self-energy is

$$\Sigma(i\omega_n) = \frac{(-U)^2}{\beta} \sum_{i\nu_n} \frac{1}{i\omega_n - i\nu_n} \left(\frac{\beta}{4} \delta_{i\nu_n, 0} \right) = \frac{1}{i\omega_n} \frac{U^2}{4}, \quad (\text{E.4})$$

which is the atomic expression. IPT can be extended away from half-filling [143].

Appendix F

Entropy via Integration

The conventional technique for computing the entropy in numerical simulations is through a temperature integration of the total energy [144]. This requires a sequence of simulations for a sequence of temperatures extending upwards from the desired temperature to ostensibly infinite temperature, and knowledge of the infinite-temperature limit of the entropy S_∞ .

The derivation begins with formula for the entropy in terms of the specific heat,

$$S = \int_0^T dT \frac{C_V}{T} = S_\infty - \int_T^\infty \frac{dT}{T} \frac{\partial E}{\partial T}. \quad (\text{F.1})$$

We change variables to reciprocal temperature $\beta = 1/T$ and use integration by parts to remove the temperature derivative on E to obtain

$$S(\beta) = S_\infty + \beta E(\beta) - \int_0^\beta d\beta E(\beta). \quad (\text{F.2})$$

In the case of the one-orbital Anderson impurity model, $S_\infty = \log 4$.